DEVELOPMENT OF FIBER LASERS AND DEVICES FOR COHERENT RAMAN SCATTERING MICROSCOPY

A Dissertation
Presented to the Faculty of the Graduate School
of Cornell University
in Partial Fulfillment of the Requirements for the Degree of
Doctor of Philosophy

by
Erin Stranford Lamb
August 2015

© 2015 Erin Stranford Lamb

ALL RIGHTS RESERVED

DEVELOPMENT OF FIBER LASERS AND DEVICES FOR COHERENT RAMAN SCATTERING MICROSCOPY

Erin Stranford Lamb, Ph.D.

Cornell University 2015

As ultrafast laser technology has found expanding application in machining, spectroscopy, microscopy, surgery, and numerous other areas, the desire for inexpensive and robust laser sources has grown. Until recently, nonlinear effects in fiber systems due to the tight confinement of the light in the core have limited their performance. However, with advances in managing nonlinearity through pulse propagation physics and the use of large core fibers, the performance of fiber lasers can compete with that of their solid-state counterparts. As specific applications, such as coherent Raman scattering microscopy, emerge that stand to benefit from fiber technology, new performance challenges in areas such as laser noise are anticipated.

This thesis studies nonlinear pulse propagation in fiber lasers and fiber parametric devices. Applications of dissipative solitons and self-similar pulse propagation to low-repetition rate oscillators that have the potential to simplify short-pulse amplification schemes will be examined. The rest of this thesis focuses on topics relevant to fiber laser development for coherent Raman scattering microscopy sources. Coherent pulse division and recombination inside the laser cavity will be introduced as an energy-scaling mechanism and demonstrated for a fiber soliton laser. The relative intensity noise properties of mode-locked fiber lasers, with a particular emphasis on normal dispersion lasers, will be explored in simulation and experiment. A fiber optical parametric oscillator will be studied in detail for low noise frequency conversion of picosecond pulses, and its utility for coherent Raman imaging will be demonstrated. Spectral compression of femtosecond pulses is used to generate picosecond pulses to pump this device, and this technique provides a route to future noise reduction in the system. Furthermore, this device forms a multimodal source capable of providing the picosecond pulses for coherent Raman scattering microscopy and the high energy femtosecond pulses for other multiphoton imaging techniques. Finally, ideas for future extensions of this work will be discussed.

BIOGRAPHICAL SKETCH

Erin Christine Stranford was born in Palatine, Illinois in 1988. After living there for three years and in Plymouth, Minnesota for seven, she moved to Albuquerque, New Mexico where she lived until graduating from La Cueva High School. Having always loved mathematics, she decided to enroll in the applied mathematics program at the University of Tulsa in Tulsa, Oklahoma. Since she enjoyed conducting small research projects for New Mexico's reginal and state science fairs throughout high school, Erin decided to try majoring in physics as well. Thanks to the enthusiasm and skilled instruction of the physics faculty at the University of Tulsa, Erin remained in physics and graduated with dual bachelor's degrees in 2010.

Erin enjoyed her introduction to optics through research projects with Professor Scott Holmstrom at the University of Tulsa and Professor Thomas Schibli through a summer REU at the University of Colorado at Boulder, so she decided to pursue Ph.D. studies in optics. Attracted to the applied physics program at Cornell University due to its strong optics research, she enrolled in the fall of 2010 and joined Professor Frank Wise's group. Erin has greatly enjoyed the time she has spent here researching fiber lasers and fiber parametric devices.

After completing her Ph.D., Erin will be a postdoctoral researcher with the time and frequency division of the National Institute of Standards and Technologies in Boulder, Colorado. There, she intends to study microresonator frequency combs and cavity soliton generation with Dr. Scott Diddams and Dr. Scott Papp.

To my family: Alan, Dad, Mom, Laura, and Devin.

ACKNOWLEDGEMENTS

First, I would like to give my sincere thanks to Frank Wise for all of the help, support, and guidance given during my time at Cornell. I truly appreciate the opportunity of learning from someone as knowledgable and kind as Frank, and it has been an honor to be a member of his group.

I also thank Will Renninger and Simon Lefrancois for their patience and generosity in teaching me when I first joined the group; I owe both a large debt of gratitude. I also appreciate the help and camaraderie of the other members of the Wise group, including: Andy Chong, Hui Liu, Luming Zhao, Heng Li, Adam Bartnik, Peng Li, Yuxing Tang, Zhanwei Liu, Logan Wright, Zimu Zhu, and Walter Fu. I additionally thank Walter for useful comments on a draft of this thesis.

I have also enjoyed the chance to work with some excellent collaborators. In particular, I thank Sunney Xie, Minbiao Ji, Dan Fu, and Wenlong Yang from Harvard University and Adrea Johnson and Yoshi Okawachi from Cornell University for working with me and giving me the chance to learn about applications of fiber lasers and devices. I also thank William Wadsworth from the University of Bath for providing photonic crystal fiber for my experiments and Toptica Photonics for the loan of equipment that was of invaluable help.

I give special thanks to my husband Alan Lamb for all of his help, encouragement, support, and enthusiasm for my work, and to my parents Jerry and Marty Stranford and my sisters Laura and Devin Stranford for always being there and for making it to Ithaca to visit.

Finally, I thank Alex Gaeta and Steve Strogatz for serving on my committee and the National Science Foundation, the National Institutes of Health, and the National Science Foundation Graduate Research Fellowship Program for providing financial support for the work presented in this thesis.

TABLE OF CONTENTS

LIST OF TABLES

LIST OF FIGURES

BIBLIOGRAPHY

[1] S. Lefrançois, Ph.D. thesis, Cornell University, 2012.

[2] S. Lefrancois, D. Fu, G. R. Holtom, L. Kong, W. J. Wadsworth, P. Schneider, R. Herda, A. Zach, X. S. Xie, and F. W. Wise, Opt. Lett. **37**, 1652 (2012).

CHAPTER 1

INTRODUCTION

The discovery of Kerr-lens mode-locking of the titanium sapphire laser led to rapid progress in the field of ultrafast science. The demand for stable sources of ultrafast pulses continues to grow in fields as diverse as telecommunications, materials processing, biological imaging and surgery, metrology, and basic science. Despite the impressive success of the titanium sapphire laser as a source of femtosecond pulses, solid-state lasers are limited in real-world applications due to their cost, size, cooling requirements, and need for precise alignment of bulk optical components [1].

Fiber lasers have emerged in the last decade as an alternate route to high energy ultrashort pulses. As a laser medium, doped optical fiber has many advantages over its solid-state counterparts. For one, the waveguide nature of optical fiber enables perfect overlap of the pump and signal in the gain medium, and, in some cases, the construction of completely alignment free lasers with no free space components. For another, the large ratio of the surface area to the volume of the fiber eliminates the need for water cooling of the gain medium. Finally, the single mode properties of optical fiber ensure excellent beam quality [2]. Practically, fiber lasers tend to be less expensive than solid-state lasers, enabling laser technology to be more widely adopted, especially outside of specialized laboratories.

Despite the numerous advantages of optical fiber, the performance of ultrafast fiber lasers has lagged behind that of solid-state lasers due the tight confinement of intense pulses in the core of the fiber. This can lead to large enhancements of nonlinear effects that can pose severe limitations to laser performance. Fortunately, the development of robust large-mode fibers and a detailed understanding of pulse propagation in fiber lasers has led to orders of magnitude increases in ultrafast fiber laser performance in the last ten years. In particular, taking advantage of pulse propagation in normal dispersion fiber has enabled the shortest pulses and highest energies from fiber lasers to date [3].

1.1 Organization of thesis

This thesis studies pulse propagation in fiber lasers and fiber parametric devices as a route to high-performance fiber-based devices. After introducing basic concepts in this chapter, low-repetition rate fiber oscillators will be discussed with the goal of developing lasers well-suited to simplifying short-pulse amplification. The rest of the work presented in this thesis is focused on various topics in fiber laser development for coherent Raman scattering microscopy. Coherent pulse division and recombination inside of a laser cavity will be introduced and demonstrated as a technique to increase the output pulse energy directly from a laser cavity. Simulation and measurement of relative intensity noise in mode-locked fiber lasers will also be presented, with an emphasis on the noise properties of normal dispersion fiber lasers. A two-color source for coherent Raman scattering microscopy based on frequency conversion in an optical parametric oscillator will be presented along with a discussion of extensions and possible routes to noise reduction by utilizing normal dispersion fiber lasers. In particular, the use of spectral compression of a dissipative soliton laser will be demonstrated as a route to a multimodal imaging source capable of meeting the pulse parameters for Raman and multiphoton imaging techniques. Finally, future directions of this work will be discussed.

1.2 Pulse propagation in fiber

The equations modeling pulse propagation in fiber are described below. In addition, the quantum noise terms that will be simulated are introduced, and the simulation model is discussed.

1.2.1 Generalized nonlinear Schrodinger equation

Fundamentally, pulse propagation in optical fiber is governed by Maxwell's equations. Under a series of standard approximations, Maxwell's equations reduce to the generalized nonlinear Schrodinger equation. This derivation is presented in numerous textbooks, such as references [4, 5, 6], and summarized below.

We begin with the wave equation:

$$\nabla^2 \mathbf{E} - \frac{1}{c^2}\frac{\partial^2 \mathbf{E}}{\partial t^2} = \mu_0 \frac{\partial^2 \mathbf{P}_L}{\partial t^2} + \mu_0 \frac{\partial^2 \mathbf{P}_{NL}}{\partial t^2}, \tag{1.1}$$

where $\mathbf{E}$ is the electric field, c is the speed of light in vacuum, μ_0 is the magnetic permeability of free space (later, ϵ_0 is the electric susceptibility), and $\mathbf{P}_L$ and $\mathbf{P}_{NL}$ are the linear and nonlinear portions of the polarizability, respectively. A few standard assumptions are then made. Namely, we assume that $\mathbf{P}_{NL}$ is a perturbation of $\mathbf{P}_L$, that the polarization of the electric field is maintained during propagation through the fiber, and that the envelope of the pulse changes on a time scale much slower than the carrier frequency, which is expressed as:

$$\frac{\Delta\omega}{\omega_0} \ll 1 \tag{1.2}$$

and known as the slowly varying envelope approximation (SVEA).

Under the SVEA, we can separate the slowly varying portion of the electric field, $\mathbf{A}(\mathbf{r},t)$, to write:

$$\mathbf{E}(\mathbf{r},t) = \frac{1}{2}\hat{x}(F(x,y)A(z,t)\exp\left[i(\beta_0 z - \omega_0 t)\right] + c.c.), \tag{1.3}$$

where *F(x,y)* represents the rapidly varying portion of the field and *c.c.* stands for complex conjugate. $\mathbf{P}_L$ and $\mathbf{P}_{NL}$ and can be written in a similar form.

For $\mathbf{P}_{NL}$, we assume that the third order nonlinearity is the dominant term (which is generally true for silica fiber) and that the third order susceptibility can be expressed as

$$\chi^{(3)}(t-t_1, t-t_2, t-t_3) = \chi^{(3)}R(t-t_1)\delta(t_1-t_2)\delta(t_2-t_3), \tag{1.4}$$

where *R(t)* is the normalized nonlinear response function. This expression encompasses the intensity dependent nonlinear effects, including self-phase modulation (SPM), stimulated Raman scattering (SRS), self-steepening, and shock formation. This yields the final expression for the nonlinear polarization:

$$P_{NL} = \frac{3\epsilon_0}{4}\chi^{(3)}E(\mathbf{r},t)\int_{-\infty}^{t} R(t-t_1)E^*(\mathbf{r},t_1)E(\mathbf{r},t_1)dt_1. \tag{1.5}$$

As detailed in references [4, 5, 6], the wave equation can now be transformed to the frequency domain to be solved using separation of variables and then transformed back to the time domain. This yields the final form for the generalized nonlinear Schrodinger equation (GNLSE):

$$
\begin{aligned}
&\frac{\partial A}{\partial z} + \frac{\alpha}{2}A - \sum_{n=2}^{\infty} i^{n+1}\frac{\beta_n}{n!}\frac{\partial^n A}{\partial t^n} = \\
&\quad i\gamma\left(1 + \frac{i}{\omega_0}\frac{\partial}{\partial t}\right)\left(A(z,t)\int_{-\infty}^{t} R(t-t')|A(z,t')|^2 dt'\right). \qquad (1.6)
\end{aligned}
$$

In this equation, α represents linear gain or loss, the β_n terms are the coefficients of the Taylor expansion of the fiber's dispersion profile, and $\gamma = \frac{n_2(\omega_0)\omega_0}{cA_{eff}}$ is the nonlinear coefficient representing SPM. The nonlinear response function can take the form

$$
R(t) = (1 - f_R)\delta(t - t_e) + f_R h_R(t), \qquad (1.7)
$$

where $h_R(t)$ is the Raman response, determined by the material, f_R defines the contribution of the delayed Raman response to the nonlinear polarization, and t_e represents the nearly instantaneous electronic response time [5].

Under the assumptions of negligible loss and a long enough pulse that higher-order dispersion, self-steepening, and the Raman response are small, the GNLSE reduces to the nonlinear Schrodinger equation (NLSE):

$$
\frac{\partial A}{\partial z} = -\frac{i\beta_2}{2}\frac{\partial^2 A}{\partial t^2} + i\gamma|A|^2 A, \qquad (1.8)
$$

where β_2 is the second order dispersion, also known as the group velocity dispersion (GVD). This equation is of particular importance to pulse propagation in the anomalous dispersion regime.

1.2.2 Intensity noise in pulse propagation

The GNLSE is a deterministic equation. This thesis will also consider the intensity noise in fiber systems, which will require the introduction of shot noise into the pulse propagation model. Shot noise represents the fundamental limitation to intensity noise arising from quantum mechanics and can be thought of as an uncertainty of one photon of random phase per frequency component. The shot noise field itself can be represented in the time domain as a random amplitude fluctuation $\delta A(t)$ with an autocorrelation defined as

$$G_{\delta A}(\tau) \equiv \langle \delta A^*(t)\delta A(t+\tau)\rangle = \frac{h\nu}{2}\delta(\tau), \tag{1.9}$$

where h is Planck's constant and ν is the carrier frequency. This is related to the two sided power density

$$S_{\delta A}(f) = \int_{-\infty}^{+\infty} G_{\delta A}(t)e^{i2\pi ft}dt = \frac{h\nu}{2}. \tag{1.10}$$

Equivalent representations can be written in the frequency domain [7].

During pulse propagation, quantum noise is added to the complex amplitudes to account for spontaneous emission from gain and loss. This is implemented by adding variations that correspond to the shot noise variances multiplied by the amount of gain or loss [7].

1.2.3 Simulating the generalized nonlinear Schrodinger equation

The laser cavities in this thesis are modeled using the split-step Fourier method, as described in reference [5]. This method is based on separating the action of nonlinearity and dispersion by approximating the spatial derivative of the amplitude as

$$\frac{\partial A}{\partial z} = (\hat{D} + \hat{N})A, \tag{1.11}$$

where $\hat{D}$ is an operator encompassing dispersion and other linear effects and $\hat{N}$ is the operator describing nonlinear effects. For the lasers and parametric devices studied in this thesis,

$$\hat{D} = \sum_{n=2}^{\infty} i^{n+1} \frac{\beta_n}{n!} \frac{\partial^n}{\partial T^n} - \frac{\alpha}{2} \tag{1.12}$$

and

$$\hat{N} = i\gamma\left(|A|^2 + \frac{i}{\omega_0} \frac{1}{A} \frac{\partial}{\partial T}(|A|^2 A) - T_R \frac{\partial |A|^2}{\partial T} \right), \tag{1.13}$$

where

$$T_R = \int_0^{\infty} tR(t)dt. \tag{1.14}$$

In the split-step Fourier method, the two operators are assumed to act independently over a small longitudinal step h along the fiber. In its simplest form, propagation is accomplished by evaluating the expression

$$A(z+h,T) \approx \exp(h\hat{D}) \exp(h\hat{N}) A(z,T). \tag{1.15}$$

By employing the Baker-Hausdorff equation [8] for two non-commuting operators, we observe that the split-step method is accurate to the order of

$$\frac{1}{2}[h\hat{D}, h\hat{N}] = \frac{1}{2}h^2[\hat{D}, \hat{N}] = O(h^2). \tag{1.16}$$

The accuracy of the split-step Fourier method can be increased by adopting the symmetrized split-step method, where half of the dispersion operator is applied before the nonlinear operator and half after. This is represented by replacing equation 1.15 with

$$A(z+h,T) \approx \exp\left(\frac{h}{2}\hat{D}\right) \exp\left(\int_a^{z+h} N\hat{(z')} dz'\right) \exp\left(\frac{h}{2}\hat{D}\right) A(z,T). \tag{1.17}$$

Then, the double commutator term from the Baker-Hausdorff formula determines the accuracy, which is now on the order of h^3. The linear operator $\hat{D}$ is evaluated in the Fourier domain, and the nonlinear operator $\hat{N}$ is evaluated using a fourth-order Runge-Kutta method.

The symmetric split-step Fourier method is used for simulating the lasers presented in this thesis, using an adapted version of the code presented in reference [9]. For most of these cavities, the effects of SRS and self-steepening are negligible and thus not simulated. For simulations of four-wave mixing (FWM) in optical parametric amplifiers and oscillators, SRS and self-steepening become more significant and higher accuracy may be desired due to large simulated bandwidths. Thus, FWM is simulated using a Runge-Kutta integrator that incorporates both the linear operator $\hat{D}$ and the nonlinear operator $\hat{N}$, which allows for the cancellation of higher-order error terms and therefore improved accuracy. This method is known as the Runge Kutta in the Interaction Picture method, or RK4IP, and is described in reference [10]. The RK4IP code used for simulations in this thesis is an adapted version of the code described in reference [11].

1.3 Mode-locking in fiber lasers

Mode-locking is the process by which a laser produces pulses of radiation as opposed to emitting continuous-wave (CW) radiation. It occurs when the longitudinal modes of the resonator cavity become mutually coherent, causing periodic constructive interference of the modes. This produces pulses of light separated by the round-trip time of the cavity [12].

Mode-locking can be achieved using either active or passive methods. In active mode-locking, an element such as an acousto-optic modulator is introduced into the laser cavity to induce amplitude modulations. When the frequency of the modulation matches the mode spacing in the cavity, the modes will be driven in phase and achieve coherence. The pulse durations from actively mode-locked lasers are limited to picoseconds at best due to realistically achievable modulation frequencies [12]. In contrast, passive mode-locking allows the generation of orders of magnitude shorter pulses by replacing the active modulator by a saturable absorber (SA), which is a passive element that introduces intensity-dependent loss into the cavity. In this case, the loss through the SA is modulated by the pulse itself, removing the response time of electronics as a limitation to the pulse duration. Specific implementations of SAs will be discussed later in this chapter.

Numerous methods exist for creating pulses in laser cavities, and the underlying physics of how the pulses form and are stabilized can be quite different. The remainder of this section will discuss the pulse propagation and characteristic features of the main known classes of mode-locked fiber lasers.

1.3.1 Soliton mode-locking

Solitons are well-known static solutions to the NLSE:

$$\frac{\partial A}{\partial z} = -\frac{i\beta_2}{2}\frac{\partial^2 A}{\partial t^2} + i\gamma|A|^2 A, \tag{1.18}$$

and are formed through the balance of anomalous GVD and the self-focusing nonlinearity. They take the form

$$A(t,z) = \sqrt{A}\,\mathrm{sech}\left(\frac{t}{\tau}\right)\exp\left(\frac{i\beta_2}{2\tau^2}z\right), \tag{1.19}$$

where $\tau = 0.567\tau_{FWHM}$ is the normalized pulse width. Following from this equation, solitons are governed by an area theorem of the form

$$E\tau = \frac{2|\beta_2|}{\gamma}. \tag{1.20}$$

Here, E is the pulse energy found by integrating the intensity profile over all time [13, 14].

Although solitons are solutions of the NLSE in passive fiber, they also exist in laser cavities, with the gain, saturable absorption, and other cavity elements acting as perturbations on the soliton. The perturbations do, however, cause the soliton to shed dispersive radiation as it reshapes itself into a soliton. The radiated energy can interfere constructively to form the characteristic Kelly sidebands on the soliton spectrum. The condition for phase matching of the dispersive radiation is

$$\Delta\omega = \pm\frac{t}{\tau}\sqrt{m\frac{8z_0}{z_p} - 1}, \tag{1.21}$$

where m is the integer sideband order, $z_0 = \frac{\pi\tau^2}{2|\beta_2|}$ is the soliton period, and z_p is the perturbation length, or in the case of a laser, the cavity length [13, 15]. An example spectrum from a mode-locked Yb-doped fiber soliton laser is shown in Fig. 1.1. Visible first and second order Kelly sidebands can be seen.

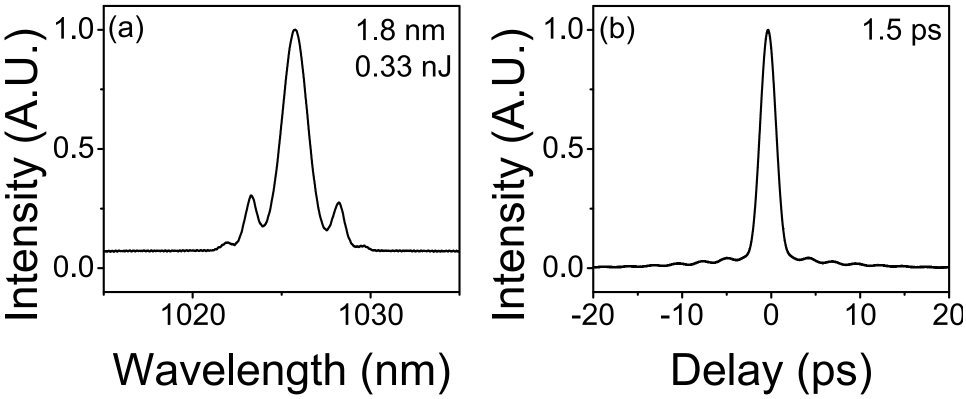

Figure 1.1: Output (a) spectrum and (b) autocorrelation from an Yb-doped fiber soliton laser.

Despite the ubiquitousness of solitons, the soliton area theorem and the presence of Kelly sidebands pose a severe limitation on the pulse energy from fiber soliton lasers. Experimentally, pulse energies of tens of picojoules are typical for sub-100 femtosecond pulses [16]. With pulse durations approaching the picosecond range, the energy limit increases to a few hundred picojoules at most.

1.3.2 Dispersion-managed soliton mode-locking

As shown by the soliton area theorem (equation 1.20), nonlinearity poses a significant limitation on the pulse energy from soliton lasers. However, the influence of nonlinearity can be negated to an extent by using alternating sections of normal and anomalous dispersion within the laser cavity, which is referred to as a dispersion map. The anomalous dispersion segments support the soliton solution, and the normal dispersion segments stretch the pulse in time, reducing its peak power and thus reducing the nonlinear phase accumulation in the cavity [16, 17].

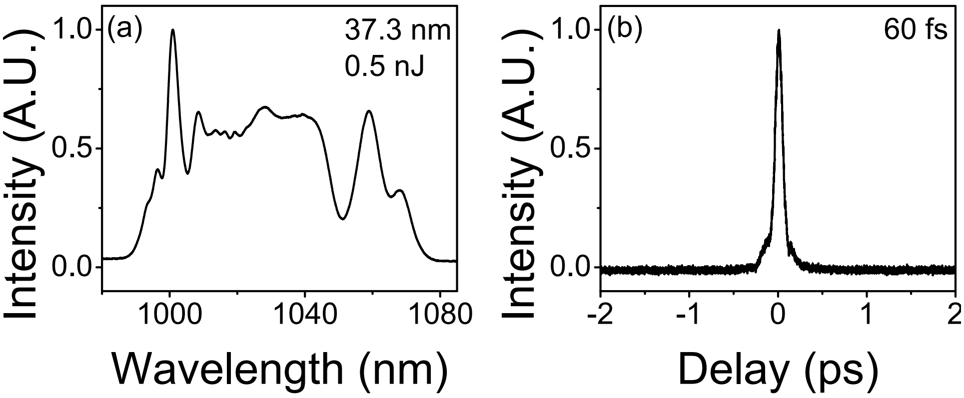

Figure 1.2: Output (a) spectrum and (b) autocorrelation from a dispersion-managed Yb-doped fiber soliton laser.

This process, called dispersion management, can be used to achieve an order of magnitude increase in the pulse energy. The pulse can be stable at both net anomalous and net normal dispersion (though not at exactly zero dispersion). The shortest pulses tend to exist near zero dispersion, and the highest energy pulses (up to around 2 nJ) exist in the net-normal dispersion regime [18]. An example mode-locked spectrum and autocorrelation for a dispersion-managed soliton with a net normal dispersion of approximately 2000 fs^2 are shown in Fig. 1.2.

1.3.3 Dissipative soliton mode-locking

Dissipative solitons exist in the normal dispersion regime and thus cannot be explained by the soliton solutions of the NLSE, which rely on the balance of anomalous dispersion and SPM. Instead, dissipative solitons balance normal dispersion, nonlinear phase accumulation, saturable absorption, and spectral filtering [3] and are modeled by a cubic-quintic Ginzburg-Landau equation of the form

$$\frac{\partial A}{\partial z} = gA + \left(\frac{1}{\Omega} - i\frac{D}{2}\right)\frac{\partial^2 A}{\partial t^2} + (\alpha + i\gamma)|A|^2|A| + \delta|A|^4 A, \tag{1.22}$$

where A is the field amplitude, g is the gain and loss per unit length, Ω is related to the spectral filter bandwidth, D represents the dispersion, γ is the nonlinear coefficient, and α and γ are the cubic and quintic terms representing the SA [19]. A particular solution to this equation exists and qualitatively reproduces the behavior of dissipative soliton lasers as described in reference [19].

The spectral filter is a key element in ensuring the self-consistency of the dissipative soliton in the laser cavity. Although filtering of a transform-limited pulse increases the pulse duration, filtering a chirped pulse decreases the pulse duration by removing spectral components on the leading and/or trailing edges of the pulse. Thus, self-consistency is maintained as the pulse acquires chirp and is lengthened in the fiber segments of the cavity and is then returned to its initial condition by the action of the spectral filter before the next round-trip [20]. As a result of this process, the dissipative soliton experiences spectral and temporal breathing within the cavity, and the output pulse is highly chirped. The output pulse energy and duration can be tuned by changing parameters such as the net cavity dispersion, the spectral filter bandwidth, and the amount of nonlinear phase accumulation within the cavity [21].

A common output spectrum and de-chirped pulse are shown in Fig. 1.3. The steep sides of the spectra are one of the most distinctive features of dissipative solitons. At repetition rates above 10 MHz, the output pulses can by de-chirped to close to the transform limit. At even lower repetition rates, longer chirped pulses are achieved and the de-chirped pulses tend to acquire a larger deviation from the transform limit [22].

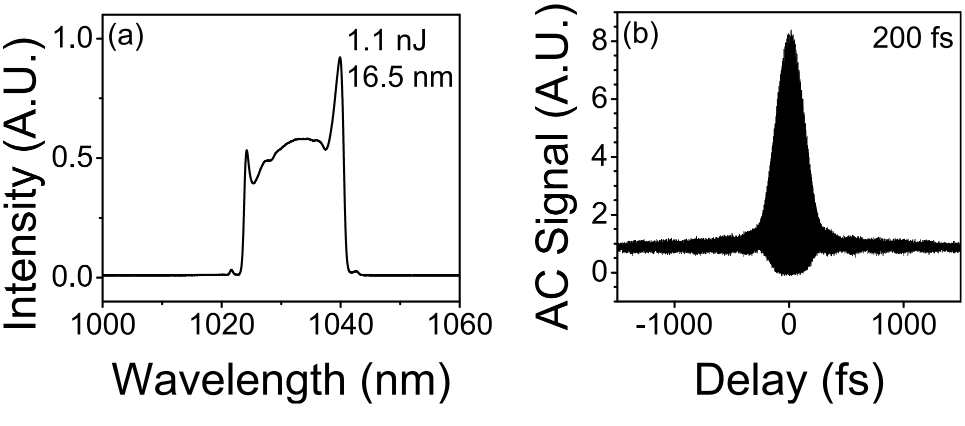

Figure 1.3: Output (a) spectrum and (b) autocorrelation from an Yb-doped fiber dissipative soliton laser.

Importantly, dissipative solitons are not subject to the area theorem of the NLSE and can achieve orders of magnitude higher energy than solitons in oscillators with single mode fiber. Experimentally, pulse energies on the order of 20 nJ with sub-200 fs pulse durations can be achieved from a variety of laser cavities [23, 24].

Optimizing dissipative solitons for short pulse duration produces pulses around 70 fs with up to 2 nJ of pulse energy [25], with the limit on pulse duration being set by the amount of dispersion (fiber) needed to construct a physically realizable cavity.

1.3.4 Passive self-similar mode-locking

Parabolic pulses are known self-similar solutions to the NLSE with normal dispersion. Thus, a pulse with a parabolic profile, which has the form

$$A^2(0,t) = A_0^2\left(1 - \left(\frac{t}{\tau}\right)^2\right), \tag{1.23}$$

with $t < \tau$, will maintain its parabolic shape during propagation [26]. Since the Fourier transform of a parabola is a parabola, the pulse is in fact parabolic in both the time and frequency domains. Both normal GVD and SPM act to add a parabolic phase in their respective domains, so the pulse profile remains unchanged during propagation. These pulses are termed similaritons in analogy with solitons. Furthermore, the quadratic temporal phase caused by SPM results in a linear frequency sweep, so the chirp of self-similarly propagating parabolas tends to remain linear [27].

Ilday *et al.* [27] demonstrate self-similar propagation in a fiber laser by using intra-cavity dispersion compensation to maintain self-consistency. The pulse stretches in time as it propagates through the fiber and is then re-set to its original duration through a dispersive delay line (DDL) before beginning the next round trip. The output pulse is taken before the DDL and is thus highly chirped. Due to the mostly linear chirp of the similaritons, they can be de-chirped to their transform limit using a grating pair external to the cavity. Pulse energies up to around 10 nJ and pulse durations down to around 100 fs can be achieved using this pulse shaping technique.

1.3.5 Amplifier similariton mode-locking

The NLSE with normal dispersion and gain,

$$\frac{\partial A}{\partial z} = -\frac{i\beta_2}{2}\frac{\partial^2 A}{\partial t^2} + i\gamma|A|^2 A + \frac{g}{2}A, \tag{1.24}$$

exhibits an asymptotic self-similar solution in the limit that $z \to \infty$ [28]. As opposed to the passive similaritons described above, these amplifier similaritons are actually nonlinear attractors of the NLSE with gain. Thus, any pulse launched into normal dispersion gain fiber will tend towards a parabolic pulse of the form

$$A(z,t) = A_0(z)\sqrt{\left(1 - \left(\frac{t}{\tau(z)}\right)^2\right)}e^{i\phi(z,t)}, \tag{1.25}$$

where $t \leq \tau$. The pulse phase ϕ, chirp $\delta\omega$, amplitude $A_0(z)$, and duration $\tau(z)$ evolve according the following relations:

$$\phi(z,t) = \phi_0 + 3\gamma\left(\frac{1}{2g}\right)A_0^2(z) - g\left(\frac{1}{6\beta_2}\right)t^2, \tag{1.26}$$

$$\delta\omega(t) = \frac{-\partial\phi(z,t)}{\partial t} = g\left(\frac{1}{3\beta_2}\right)t, \tag{1.27}$$

$$A_0(z) = 0.5(gE)^{1/3}(\gamma\beta_2/2)^{-1/6}\exp\left(\frac{gz}{3}\right), \tag{1.28}$$

and

$$\tau(z) = 3g^{-2/3}\left(\frac{\gamma\beta_2}{2}\right)^{1/3}E^{1/3}\exp\left(\frac{gz}{3}\right). \tag{1.29}$$

In the above relationships, E is the input pulse energy. These equations highlight that as the pulse propagates through the gain medium, it acquires linear chirp and the energy and pulse width grow exponentially [28]. The ultimate limitation to the pulse evolution is typically the gain bandwidth inhibiting further spectral growth.

The nonlinear attraction to a parabola has been utilized in self-similar amplification to generate pulses as short as 50 fs [29]. This pulse shaping mechanism can also be used in laser systems, although some technique must be employed to maintain self-consistency in the oscillator cavity due to the large spectral growth the pulse experiences in the gain medium. Oktem *et al.* report a soliton-similariton Er-doped fiber laser that uses soliton attraction in anomalous dispersion fiber to re-set the pulse each round trip [30]. Simultaneously, Renninger and coworkers report using a narrow-band spectral filter before the gain fiber to ensure consistent seeding of the gain fiber [31]. In a further demonstration of the robustness of this technique, a Raman amplifier similariton laser that utilizes Raman gain has also been demonstrated [32]. It also takes advantage of a narrow bandpass filter to ensure consistency.

Generally, the spectra from mode-locked amplifier similariton lasers expand to fill the gain bandwidth, enabling some of the shortest pulses from fiber lasers.

The pulses from these lasers typically de-chirp to the transform limit, enabling durations as short as 40 fs from Yb-doped fiber lasers [31]. Pulse energies of up to 4 nJ are typical from lasers based on single mode fiber. Example spectra from an Yb-doped amplifier similariton fiber laser are shown in Fig. 1.4.

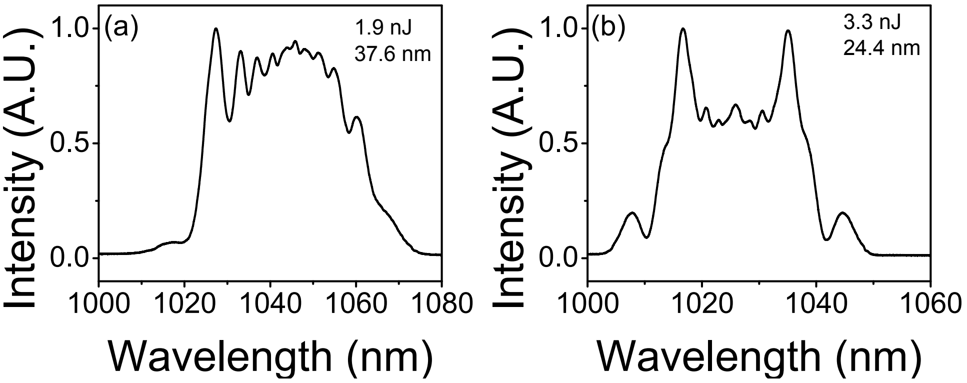

Figure 1.4: Example spectra from an Yb-doped fiber amplifier similariton laser.

Unlike the other pulse evolutions discussed in this section, the amplifier similariton is based on local attraction in one segment of the cavity (the gain) rather than existing as an average cavity solution. This opens up the possibility of manipulating the pulse in other sections of the cavity while maintaining mode-locking, as long as the pulse is returned to the proper seed condition before the gain fiber. Examples of this include a demonstration that similar performance can be achieved from an amplifier similariton laser with varying net dispersion, including at net anomalous dispersion [33], and extending the bandwidth of the spectrum beyond the gain bandwidth limit in fiber after the gain [34].

1.4 Fiber laser components

Most of the fiber lasers described in the above section rely on saturable absorbers (SAs) and spectral filters to achieve stable operation. This section discusses the common implementations of SAs and spectral filters used in the devices described in this thesis.

1.4.1 Spectral filters

The bandwidth of the gain medium imposes the upper limit on the spectral filter bandwidth in the laser cavity, but it is often useful to have a narrower filter in the cavity. Specifically, spectral filtering is critically important for mode-locking dissipative solitons [20] and amplifier similaritons [31]. Additionally, spectral filters will also play a role in the optical parametric oscillator discussed in Chapter 5 of this thesis [35].

Birefringent filters

Birefringent filters are described in detail in reference [36]. Sinusoidal filters are formed by sending linearly polarized light through a birefringent material with the polarization of the light misaligned to the polarization axis of the material. This will induce a wavelength-dependent phase delay between the ordinary and extraordinary waves, so placing a second polarizer after the birefringent element will effectively block some of the wavelengths, forming a filter.

Assuming a 45° angle of incidence, the transmission of the filter can be described as

$$T = \cos^2\left(\frac{\pi(n_e - n_o)d}{\lambda}\right), \tag{1.30}$$

where d is the thickness of the material and n_e and n_o are the extraordinary and ordinary indices of refraction, respectively. In the work presented in this thesis, quartz is used as the birefringent material, and quartz-based filters can create bandwidths in the few nanometer to tens of nanometers range in the near infrared. The modulation depth of the filter can be near 100%, and the central wavelength can be tuned by rotating the quartz plate. Fig. 1.5 shows the filter profile and the filter bandwidth as a function of plate thickness at 1030 nm.

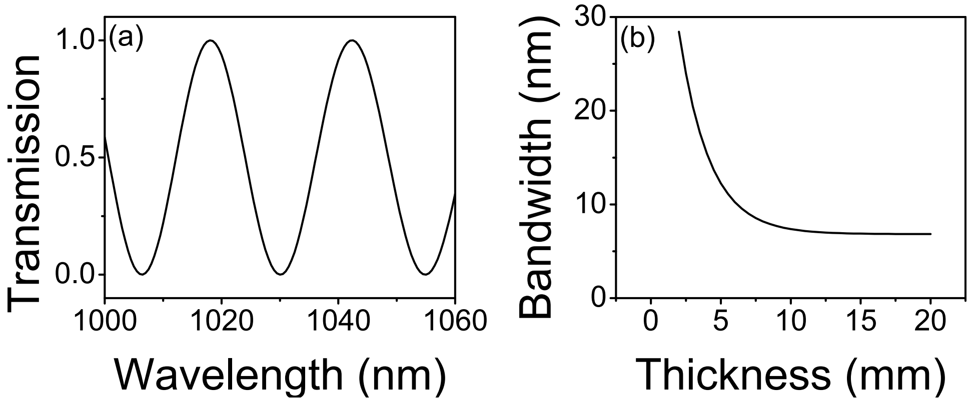

Figure 1.5: Birefringent quartz plate filters at 1030 nm. (a) Filter profile for a 5 mm thick plate. (b) Filter bandwidth as a function of thickness.

Grating filters

Due to the multiple pass-bands of the birefringent filter (see Fig. 1.5), they do not make suitable single-peaked filters with few-nanometer bandwidths since multiple pass bands may fall within the spectrum that is being filtered. To achieve a single-peaked filter with a bandwidth of a few nanometers, a grating filter can be used. The grating spatially disperses the colors in the spectrum as shown in Fig. 1.6, and a spectral filter can be formed by placing an aperture, such as a lens and fiber tip (collimator), in the dispersed beam. The fiber only picks up a portion of the dispersed spectrum due to the finite acceptance angle of the fiber. In the case of standard single-mode fibers at 1030 nm, bandwidths around 2 nm can be achieved using gratings with a line density of 600 per millimeter, and bandwidths around 4 nm are achieved using a grating with 300 lines per millimeter. The profile shape is Gaussian due to the Gaussian mode of the fiber. The filter bandwidths can be rigorously derived using the ABCDEF matrix formalism [37].

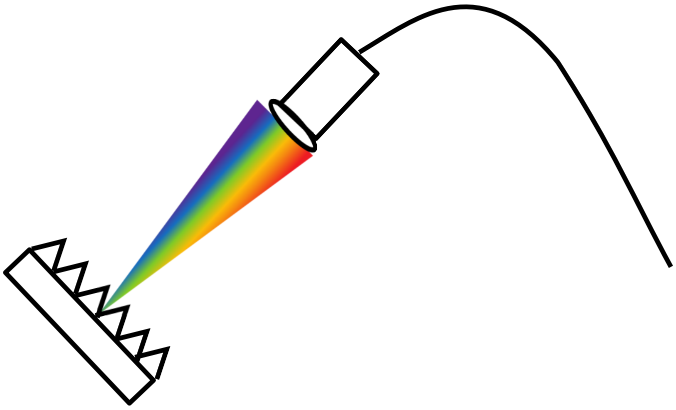

Figure 1.6: Schematic of grating-based filter.

Fabry-Perot filters

A Fabry-Perot cavity is formed by two partially reflective surfaces spaced apart by some distance. The incoming beam will reflect back and forth between the two surfaces, and interfere constructively and destructively due to the phase changes the beam undergoes upon reflection. As described in reference [38], the end result is periodic transmission from the cavity, with the transmission peaks separated by the free spectral range. The shape of the transmission is described by an Airy function of the form

$$T = \frac{1}{1 + \frac{4R}{(1-R)^2} \sin^2\left(\frac{\Phi}{2}\right)}, \tag{1.31}$$

where R is the reflectivity of the mirrors and Φ is related to the phase change the field experiences upon one reflection. The filter profile is shown in Fig. 1.7. This technique can be used to produce few-nanometer pass-bands separated by large enough frequencies to be effectively single-peaked.

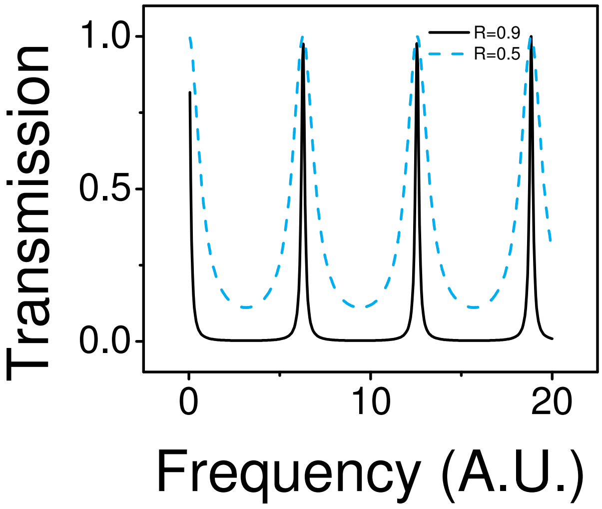

Figure 1.7: Transmission function of a Fabry-Perot filter.

1.4.2 Saturable absorbers

Saturable absorbers are critically important in aiding pulse formation in a passively mode-locked cavity. They promote pulse formation by preferentially transmitting higher intensity light, enabling high intensity fluctuations to be promoted above the background noise level. An ideal saturable absorber, which is used in the simulations presented in this thesis, has a transmission curve of the form

$$T(t) = 1 - \frac{M}{1 + P(t)/P_{sat}}, \tag{1.32}$$

where M is the modulation depth, $P(t)$ is the peak power, and P_{sat} is the saturation power. The transmission curve for an ideal SA is plotted in Fig. 1.8.

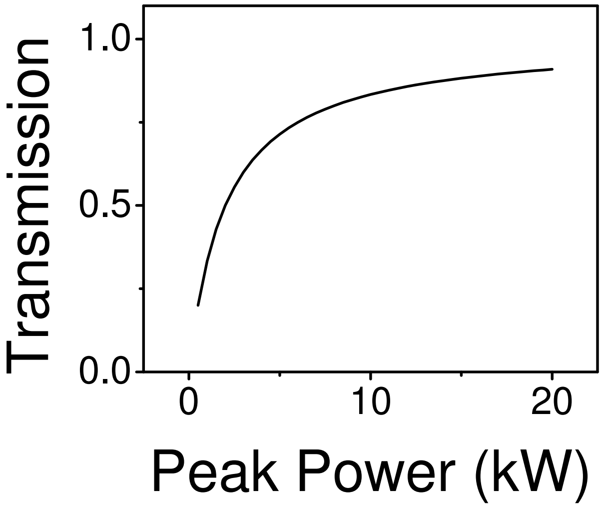

Figure 1.8: Transmission function of an ideal saturable absorber with a saturation power of 2 kW and a 100% modulation depth.

Numerous implementations of SAs have been used in laser systems, including materials with real saturable absorption, such as dyes, semiconductors, carbon nanotubes, and graphene, and artificial saturable absorbers such as nonlinear polarization evolution (NPE) and nonlinear optical loop mirrors (NOLMs). The SAs used in this thesis are discussed below.

Semiconductor saturable absorber mirrors

Semiconductor saturable absorber mirrors (SESAMs or SAMs) consist of a semiconducting material, such as Gallium Arsenide, and a reflecting surface. The light incident on the semiconducting material promotes some electrons from the valence band to the conduction band. At low incident energies, most of the incoming light is absorbed, but as the intensity increases, most of the valence electrons have already been promoted, allowing the more intense light to be transmitted and creating saturable absorption [39].

SESAMS have the advantage of being environmentally stable and promoting self-starting behavior of mode-locked states, but they tend to be limited to low modulation depths. This is in part because higher nonlinear absorption is associated with higher linear absorption, which serves to make SESAMS prone to damage at high powers. This restriction can be especially severe in high-energy fiber lasers that require higher modulation depth SAs than soliton-based solid-state lasers [40].

Nonlinear optical loop mirrors

Nonlinear optical loop mirrors (NOLMs) [41] and nonlinear amplifying loop mirrors (NALMs) [42] are based on the nonlinear interference of two counter-propagating waves. In the NOLM, the electric field is split into two unequal parts that counter-propagate through the same nonlinear material. They acquire different nonlinear phases due to their different intensities, so, when recombined, the two waves interfere and exhibit saturable absorption according to the transmission equation

$$T = 1 - 2\alpha(1-\alpha)\left[1 + \cos\left([1-2\alpha]|E_{in}|^2 \frac{2\pi n_2 L}{\lambda}\right)\right], \tag{1.33}$$

where α is the splitting ratio and L is the length of the loop. NOLMs can be conveniently implemented in fiber by splicing two ends of a fiber splitter together to form the loop. As described in equation 1.33, the shape of the transmission curve can be tuned by changing the splitting ratio and the length of fiber in the loop. Two example transmission curves are shown in Fig. 1.9.

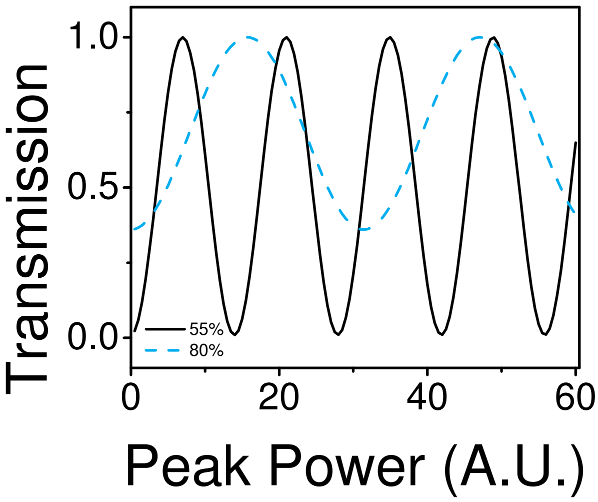

Figure 1.9: Transmission function of a nonlinear optical loop mirror (NOLM) for 55% and 80% splitting ratios.

NALMs are based on a similar concept, though instead of a passive nonlinear medium, an active gain medium is used in the loop. The presence of the gain gives an extra degree of freedom at the cost of additional complexity. Both NOLMs and NALMs can be environmentally stable through the use of polarization-maintaining fiber.

Nonlinear polarization evolution

Nonlinear polarization evolution (NPE) is the SA used most often in the lasers presented in this thesis. It is an artificial SA that converts nonlinear polarization rotation in fiber into amplitude modulation through polarization dependent loss. Due to cross-phase modulation, the polarization of elliptically polarized light will exhibit an intensity-dependent evolution described by the relative rotation angle

$$\Delta\phi_{NL} = \frac{\gamma L}{3}(|E_+|^2 - |E_-|^2), \tag{1.34}$$

where L is the length of the nonlinear medium and E_+ and E_- represent the circular basis [5]. Then, the intensity-dependent polarization change can be converted to an amplitude modulation by introducing a polarization dependent loss. The typical implementation of NPE is shown in Fig. 1.10. A quarter-wave plate is placed after a polarizer and before a fiber to set elliptical polarization in the nonlinear material, and, at the output of the fiber, an half-wave plate and a quarter-wave plate are placed before a polarizer to induce the polarization-dependent loss. In many of the lasers discussed here, the rejection port of the second polarizer is used as the output coupler.

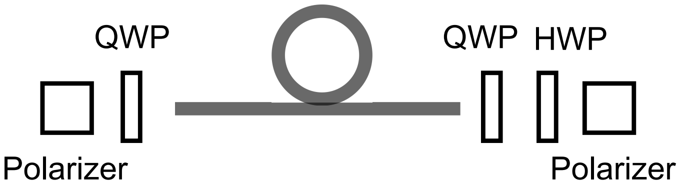

Figure 1.10: Implementation of a nonlinear polarization evolution (NPE)-based saturable absorber. QWP: quarter-wave plate; HWP: half-wave plate.

1.5 Fiber four-wave mixing

Four-wave mixing (FWM) is a parametric process mediated by the third-order nonlinear susceptibility, $\chi^{(3)}$ [5]. In general, two pump photons are annihilated to produce signal and idler photons at higher and lower frequencies, respectively, as long as energy and momentum are conserved in the process. In this thesis, degenerate FWM, where both pump photons are the same frequency, will be considered. In the case of pump degenerate FWM, the conservation laws, also known as the phase-matching conditions, are described by the expressions

$$2\hbar\omega_p = \hbar\omega_s + \hbar\omega_i \tag{1.35}$$

and

$$\Delta\mathbf{k} = 2\mathbf{k}_p - \mathbf{k}_s - \mathbf{k}_i = 0, \tag{1.36}$$

where the $\hbar\omega$ is the photon energy, $\hbar\mathbf{k} = \hbar\frac{2\pi n(\omega)}{\lambda}$ is the photon momentum, and p, s, and i refer to the pump, signal, and idler. This process is depicted in 1.11.

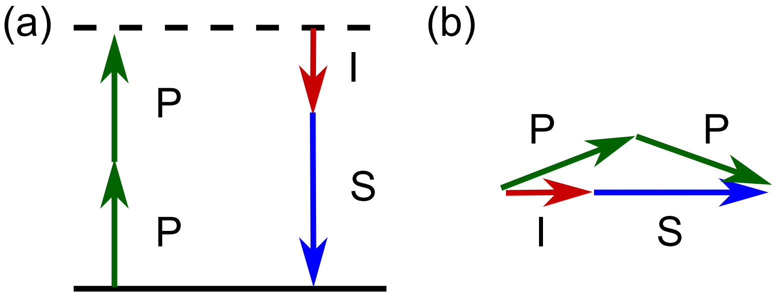

Figure 1.11: (a) Energy conservation in degenerate FWM. (b) Momentum conservation in degenerate FWM. P: pump; S: signal; I: idler.

The parametric gain for the FWM process can be calculated in the small signal approximation by considering the GNLSE with higher-order dispersion and self-phase modulation [5]:

$$\frac{\partial A}{\partial z} = \sum_{n=2}^{\infty} i^{n+1}\frac{\beta_n}{n!}\frac{\partial^n A}{\partial t^n} + i\gamma P_0|A|^2 A. \tag{1.37}$$

A solution of the form

$$A(z,t) = A_0(z) + A_1(z)e^{i(\omega_0-\omega)t} + A_2(z)e^{i(\omega_0+\omega)t}, \tag{1.38}$$

where $A_1(z) = e^{gz}$, can be substituted into equation 1.37. $A_0(z)$ is the strong pump field at frequency ω_0 and $A_1(z)$ and $A_2(z)$ are the weak signal and idler fields shifted by frequency ω from the pump. The expression for the parametric gain g is found by solving for the amplitudes using perturbation analysis and is

$$g = \sqrt{(\gamma P_0)^2 - \left(\frac{\kappa}{2}\right)^2}, \tag{1.39}$$

where

$$\kappa = 2\gamma P_0 + 2\sum_{n=1}^{\infty} \frac{\beta_{2n}}{2n!}(\omega - \omega_0)^{2n}. \tag{1.40}$$

Note that in order to satisfy the expressions for both A_1 and A_2, only even orders of dispersion will contribute to the phase matching.

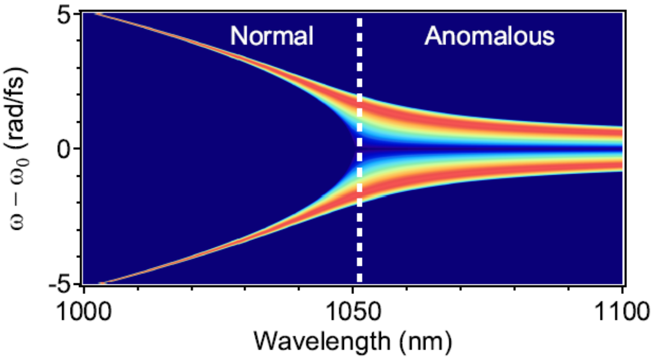

Figure 1.12: Plot of the small-signal parametric gain for four-wave mixing. Figure taken from reference [11] with permission.

The typical shape for the parametric gain spectrum is shown in Fig. 1.12. From this plot, it can be seen that the phase matching behavior is characteristically different when pumping in the anomalous or the normal dispersion region of the fiber. On the anomalous dispersion side of the zero dispersion wavelength, the signal and idler wavelengths are close to that of the pump and the gain bandwidth is relatively broad. Here, the phase matching is primarily determined through a balance of the nonlinear term and anomalous GVD. On the normal dispersion side, the GVD term is positive and cannot balance the nonlinear contribution, so the phase matching is accomplished by the higher-order dispersion terms. Since the higher order dispersion coefficients are smaller in magnitude, the frequency difference $\omega - \omega_0$ must be correspondingly larger in order for these terms to provide a sufficient contribution. This leads to wider spacing between the signal and idler wavelengths and the pump wavelength and to a narrower gain bandwidth.

1.6 Coherent Raman scattering microscopy

As described by the spontaneous Raman effect, photons scattered by a material experience a change in wavelength due to their interactions with the vibrational structure of the molecules. Although this process is extremely useful in spectroscopy due to the uniqueness of Raman spectra, the process is notoriously weak [43]. This fact has limited the use of the Raman effect for microscopy due to the long acquisition times needed to generate an image. However, by coherently driving the Raman scattering process, the signal can be greatly enhanced. Thus, coherent Raman scattering (CRS) microscopy enables video rate imaging of tissue with the three-dimensional sectioning capabilities inherent in any nonlinear imaging technique [44]. This thesis will explore development of fiber-based lasers and parametric devices to serve as a source for this class of imaging techniques. Fiber technology offers a route to creating a simple and robust source that could extend the use of CRS microcopies outside of specialized laboratories.

CRS is a FWM process. Signals for CRS processes are derived in detail in reference [45] and are summarized here. As a starting point, we derive a general expression for determining the signal from CRS, and specific cases will be considered in the following sections.

We begin with the wave equation (eq. 1.1), reprinted for convenience:

$$\nabla^2\mathbf{E} - \frac{1}{c^2}\frac{\partial^2\mathbf{E}}{\partial t^2} = \mu_0\frac{\partial^2\mathbf{P}_L}{\partial t^2} + \mu_0\frac{\partial^2\mathbf{P}_{NL}}{\partial t^2}. \tag{1.41}$$

To solve for the signal field, which we label E_4, we use a plane-wave approximation of the form:

$$\mathbf{E}(\omega_4, z, t) = \frac{1}{2}[\mathbf{E}(\omega_4, z)\exp{[i(k_4 z - \omega_4 t)]} + c.c.], \tag{1.42}$$

where k_i is the wave number. Substituting this into the wave equation and using the small-signal approximation (the pump beam remains constant during propagation) and the SVEA:

$$|k_4\frac{\partial}{\partial z}\mathbf{E}(\omega_4, z)| >> |\frac{\partial^2}{\partial z^2}\mathbf{E}(\omega_4, z)|, \tag{1.43}$$

we arrive at the following equation for the signal field:

$$\begin{aligned} ik_4\frac{\partial}{\partial z}\mathbf{E}(\omega_4, z) - \frac{k_4^2}{2}\mathbf{E}(\omega_4, z) + \frac{\omega_4^2}{2c^2}\mathbf{E}(\omega_4, z) = \\ \mu_0[\frac{\partial}{\partial t^2}(\mathbf{P}_L + \mathbf{P}_{NL})]\exp{(-i(k_4 z - \omega_4 t))}. \end{aligned} \tag{1.44}$$

Next, assume the following forms for $\mathbf{P}_L$ and $\mathbf{P}_{NL}$:

$$\mathbf{P}_L = \mathbf{P}^{(1)}(\omega_4, z, t) = \chi^{(1)}\mathbf{E}(\omega_4, z, t), \tag{1.45}$$

where

$$1 + \frac{\chi^{(1)}(\omega_4)}{\epsilon_0} = \epsilon_4 \tag{1.46}$$

and

$$\begin{aligned} \mathbf{P}_{NL} = \mathbf{P}_i^{(3)}(\omega_4, z, t) = \frac{6}{8}\chi_{ijkl}^{(3)}(-\omega_4, \omega_1, -\omega_2, \omega_3) \\ \cdot E_j(\omega_1, z)E_k^*(\omega_2, z)E_l(\omega_3, z)\exp\left(-i[\omega_4 t - (k_1 - k_2 + k_3)z]\right) + c.c. \end{aligned} \tag{1.47}$$

Substituting these expressions into equation 1.44 and neglecting the z-dependence of the field amplitudes, we arrive at

$$\begin{aligned} ik_4\frac{\partial}{\partial z}E_i(\omega_4) = -\frac{3}{4}\mu_0\omega_4^2\chi_{ijkl}^{(3)}(-\omega_4, \omega_1, -\omega_2, \omega_3) \\ \cdot E_j(\omega_1)E_k^*(\omega_2)E_l(\omega_3)\exp\left(i[(k_1 - k_2 + k_3 - k_4)z\right). \end{aligned} \tag{1.48}$$

Rearranging,

$$\frac{\partial}{\partial z}E_i(\omega_4) = \frac{3}{4}i\omega_4\sqrt{\frac{\mu_0}{\epsilon_0\epsilon_4}}\chi_{ijkl}^{(3)}(-\omega_4, \omega_1, -\omega_2, \omega_3)E_j(\omega_1)E_k^*(\omega_2)E_l(\omega_3)\exp\left(i\Delta kz\right). \tag{1.49}$$

Assuming negligible pump depletion and that $\chi^{(3)}$ is not dependent on z, equation 1.49 can be integrated over the interaction length L to yield

$$E_i(\omega_4) = \frac{3}{4} i\omega_4 \sqrt{\frac{\mu_0}{\epsilon_0 \epsilon_4}} \chi^{(3)}_{ijkl}(-\omega_4, \omega_1, -\omega_2, \omega_3) E_j(\omega_1) E^*_k(\omega_2) E_1(\omega_3) L \,\mathrm{sinc}\left(\frac{\Delta k L}{2}\right). \tag{1.50}$$

This expression will be the starting point for the analysis of two specific cases in the following sections.

1.6.1 Coherent anti-Stokes Raman scattering microscopy

Coherent anti-Stokes Raman scattering microscopy (CARS) was the first CRS technique used for microscopy and is still widely used today. CARS is a FWM process by which two colors of light are used to generate a third, termed the anti-Stokes frequency, by interacting with the Raman resonance in the material. The frequencies are related via the relation $\omega_3 = 2\omega_1 - \omega_2$, and the process is depicted in the energy level diagram shown in Fig. 1.13 [45]. To perform this technique, a pump beam with frequency ω_1 and a Stokes beam with frequency ω_2 are incident on the sample, with the frequency difference between the two colors corresponding to the Raman vibrational frequency ω_R. As the beams travel through the sample, light at the anti-Stokes frequency ω_3 is generated and collected.

The CARS process is mediated by the nonlinear polarization of the material according to:

$$P_x(\omega_3) = \frac{3}{8} \chi_{1111}(-\omega_3, \omega_1, -\omega_2, \omega_1) E_x(\omega_1) E^*_x(\omega_2) E_x(\omega_1), \tag{1.51}$$

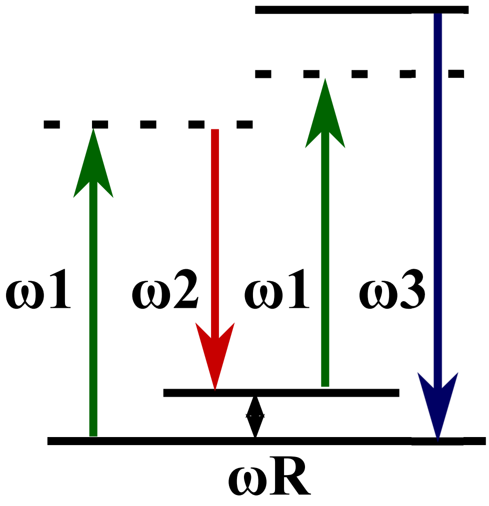

Figure 1.13: Energy diagram for CARS. ω_1 is the pump frequency, ω_2 is the Stokes frequency, ω_3 is the anti-Stokes frequency, and ω_R is the Raman vibrational frequency.

where $\omega_1 > \omega_2$ and x denotes the signal frequency.

Substituting into equation 1.50 for the signal field yields

$$E_x(\omega_3) = \frac{3}{8} i\omega_3 \sqrt{\frac{\mu_0}{\epsilon_0 \epsilon_3}} \chi_{1111}(-\omega_3, \omega_1, -\omega_2, \omega_1) E_x^2(\omega_1) E_x^*(\omega_2) L \,\mathrm{sinc}\left(\frac{\Delta k L}{2}\right), \quad (1.52)$$

where $\Delta k = |(2\mathbf{k}_1 - \mathbf{k}_2 - \mathbf{k}_3) \cdot \bar{z}|$. The nonlinear susceptibility can be expressed as

$$\chi_{1111} = \chi_{1111}^{NR} + \chi'_{1111} + i\chi''_{1111}, \quad (1.53)$$

where χ'_{1111} is the real component, χ''_{1111} is the imaginary component, and χ_{1111}^{NR} represents the non-resonant contribution. Using the above expression for the nonlinear susceptibility and noting that the intensity of the electric field in the MKS system of units can be calculated according to

$$I(\omega_3) = \frac{c}{2} n_3 \epsilon_0 |E_x(\omega_3)|^2, \tag{1.54}$$

the detected CARS intensity becomes

$$I(\omega_3) = \frac{9}{16} \frac{\omega_3^2}{n_1^2 n_2 n_3} \left(\frac{\mu_0}{\epsilon_0} \right)^2 I^2(\omega_1) I(\omega_2) L^2 \operatorname{sinc}^2 \left(\frac{\Delta k L}{2} \right)$$
$$\cdot [|\chi_{1111}^{NR}|^2 + |\chi'_{1111}|^2 + |\chi''_{1111}|^2 + 2\chi^{NR}(\chi'_{1111})^*]. \tag{1.55}$$

This expression indicates one of the main disadvantages of CARS microscopy: namely, the signal dependence on the electronic non-resonant contribution to the nonlinear susceptibility. This limits the signal-to-noise ratio and sensitivity of CARS, and makes the determination of chemical concentration from the signal more complicated.

1.6.2 Stimulated Raman scattering microscopy

Stimulated Raman scattering (SRS) microscopy is an alternate CRS technique to CARS that is gaining popularity due to its avoidance of the non-resonant background and the ease of extracting chemical concentration from the detected signal [46]. Fig. 1.14 depicts the SRS process. Here, pump light at frequency ω_1 and Stokes light at ω_2 are incident on the sample, and either the gain at ω_2 or the loss at ω_1 can be detected. These processes are termed stimulated Raman gain (SRG) and stimulated Raman loss (SRL), respectively.

Following the derivation for the SRS signal presented in reference [45], we begin with the nonlinear polarization for the Stokes beam at frequency ω_2:

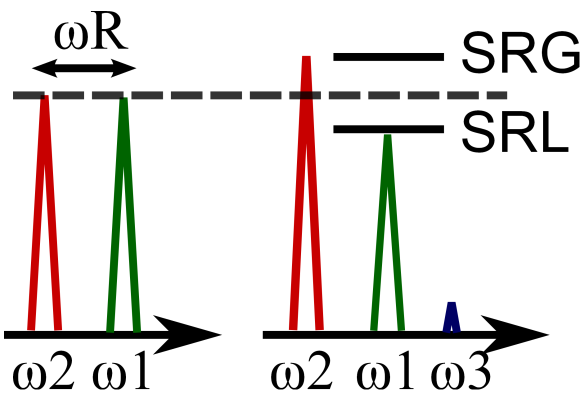

Figure 1.14: Depiction of SRS. ω_1 is the pump frequency, ω_2 is the Stokes frequency, ω_3 is the anti-Stokes frequency, and ω_R is the Raman vibrational frequency. SRG is the stimulated Raman gain and SRL is the stimulated Raman loss.

$$P_x(\omega_2) = \frac{6}{8}\chi_{11ii}(-\omega_2, \omega_2, -\omega_1, \omega_1)E_x(\omega_2)|E_i(\omega_2)|^2, \tag{1.56}$$

where i can refer to either polarization. Then, the signal field is calculated by integrating equation 1.48 without making the undepleted pump approximation to yield

$$E_x(\omega_2, L) = \exp\left(\frac{3L\omega_2}{4n_2}\sqrt{\frac{\mu_0}{\epsilon_0}}i\chi_{11ii}(-\omega_2, \omega_2, -\omega_1, \omega_1)|E_i(\omega_1)|^2\right)E_x(\omega_2, 0). \tag{1.57}$$

The intensity of the signal follows directly from this:

$$I(\omega_2, L) = I(\omega_2, 0)\exp\left(-\left(\frac{3\omega_2 L}{n_1 n_2}\left(\frac{\mu_0}{\epsilon_0}\right)\mathrm{Im}\,(\chi_{11ii})I(\omega_1)\right)\right). \tag{1.58}$$

From this expression, it can be seen that only the imaginary part of the nonlinear susceptibility contributes to the signal, which eliminates the non-resonant background observed in CARS. However, this comes at the cost of requiring a source with intensity noise levels near the fundamental shot noise limit to avoid laser fluctuations masking the SRG or SRL, which are approximately at the level of a part in 10^6 [46].

BIBLIOGRAPHY

[1] U. Keller, Applied Physics B **100**, 15 (2010).

[2] F. W. Wise, A. Chong, and W. H. Renninger, Laser & Photonics Reviews **2**, 58 (2008).

[3] W. H. Renninger, A. Chong, and F. W. Wise, Selected Topics in Quantum Electronics, IEEE Journal of **18**, 389 (2012).

[4] R. W. Boyd, *Nonlinear Optics* (Academic press, Burlington, MA, 2003).

[5] G. P. Agrawal, *Nonlinear Fiber Optics* (Academic press, Burlington, MA, 2007).

[6] P. V. Mamyshev and S. V. Chernikov, Opt. Lett. **15**, 1076 (1990).

[7] R. Paschotta, Applied Physics B **79**, 153 (2004).

[8] G. H. Weiss and A. A. Maradudin, Journal of Mathematical Physics **3**, (1962).

[9] F. O. Ilday, Ph.D. thesis, Cornell University, 2004.

[10] J. Hult, J. Lightwave Technol. **25**, 3770 (2007).

[11] S. Lefrançois, Ph.D. thesis, Cornell University, 2012.

[12] H. A. Haus, Selected Topics in Quantum Electronics, IEEE Journal of **6**, 1173 (2000).

[13] L. E. Nelson, D. J. Jones, K. Tamura, H. A. Haus, and E. P. Ippen, Applied Physics B: Lasers and Optics **65**, 277 (1997).

[14] J. Kutz, SIAM Review **48**, 629 (2006).

[15] S. M. J. Kelly, K. Smith, K. J. Blow, and N. J. Doran, Opt. Lett. **16**, 1337 (1991).

[16] K. Tamura, E. P. Ippen, H. A. Haus, and L. E. Nelson, Opt. Lett. **18**, 1080 (1993).

[17] H. A. Haus, K. Tamura, L. E. Nelson, and E. P. Ippen, Quantum Electronics, IEEE Journal of **31**, 591 (1995).

[18] H. Lim, F. O. Ilday, and F. W. Wise, Opt. Lett. **28**, 660 (2003).

[19] W. H. Renninger, A. Chong, and F. W. Wise, Phys. Rev. A **77**, 23814 (2008).

[20] A. Chong, J. Buckley, W. Renninger, and F. Wise, Opt. Express **14**, 10095 (2006).

[21] A. Chong, W. H. Renninger, and F. W. Wise, J. Opt. Soc. Am. B **25**, 140 (2008).

[22] W. H. Renninger, A. Chong, and F. W. Wise, Opt. Lett. **33**, 3025 (2008).

[23] A. Chong, W. H. Renninger, and F. W. Wise, Opt. Lett. **32**, 2408 (2007).

[24] D. S. Kharenko, E. V. Podivilov, A. A. Apolonski, and S. A. Babin, Opt. Lett. **37**, 4104 (2012).

[25] A. Chong, W. H. Renninger, and F. W. Wise, Opt. Lett. **33**, 2638 (2008).

[26] D. Anderson, M. Desaix, M. Karlsson, M. Lisak, and M. L. Quiroga-Teixeiro, J. Opt. Soc. Am. B **10**, 1185 (1993).

[27] F. O. Ilday, J. R. Buckley, W. G. Clark, and F. W. Wise, Phys. Rev. Lett. **92**, 213902 (2004).

[28] M. E. Fermann, V. I. Kruglov, B. C. Thomsen, J. M. Dudley, and J. D. Harvey, Phys. Rev. Lett. **84**, 6010 (2000).

[29] Y. Deng, C.-Y. Chien, B. G. Fidric, and J. D. Kafka, Opt. Lett. **34**, 3469 (2009).

[30] B. Oktem, C. Ulgudur, and F. O. Ilday, Nat Photon **4**, 307 (2010).

[31] W. H. Renninger, A. Chong, and F. W. Wise, Phys. Rev. A **82**, 021805 (2010).

[32] C. Aguergaray, D. Méchin, V. Kruglov, and J. D. Harvey, Opt. Express **18**, 8680 (2010).

[33] W. H. Renninger, A. Chong, and F. W. Wise, Opt. Express **19**, 22496 (2011).

[34] A. Chong, H. Liu, B. Nie, B. G. Bale, S. Wabnitz, W. H. Renninger, M. Dantus, and F. W. Wise, Opt. Express **20**, 14213 (2012).

[35] E. S. Lamb, S. Lefrancois, M. Ji, W. J. Wadsworth, X. S. Xie, and F. W. Wise, Opt. Lett. **38**, 4154 (2013).

[36] J. W. Evans, J. Opt. Soc. Am. **39**, 229 (1949).

[37] A. A. Tovar and L. W. Casperson, J. Opt. Soc. Am. A **14**, 882 (1997).

[38] W. T. Silfvast, *Laser Fundamentals* (Cambridge University Press, Cambridge, NY, 1996).

[39] U. Keller, K. J. Weingarten, F. X. Kartner, D. Kopf, B. Braun, I. D. Jung, R. Fluck, C. Honninger, N. Matuschek, and J. Aus der Au, Selected Topics in Quantum Electronics, IEEE Journal of **2**, 435 (1996).

[40] W. H. Renninger and F. W. Wise, Selected Topics in Quantum Electronics, IEEE Journal of **21**, 1 (2015).

[41] N. J. Doran and D. Wood, Opt. Lett. **13**, 56 (1988).

[42] M. E. Fermann, F. Haberl, M. Hofer, and H. Hochreiter, Opt. Lett. **15**, 752 (1990).

[43] C. V. Raman and K. S. Krishnan, Nature **121**, 501 (1928).

[44] A. Alfonso-García, R. Mittal, E. S. Lee, and E. O. Potma, Journal of biomedical optics **19**, 71407 (2014).

[45] G. L. Eesley, *Coherent Raman Spectroscopy* (Pergamon Press Inc, Elmsford, NY, 1981).

[46] C. W. Freudiger, W. Min, B. G. Saar, S. Lu, G. R. Holtom, C. He, J. C. Tsai, J. X. Kang, and X. S. Xie, Science **322**, 1857 (2008).

CHAPTER 2

LOW REPETITION RATE OSCILLATORS

2.1 Introduction

Careful management of nonlinear phase accumulation is an important part of short-pulse amplification. Femtosecond pulses are commonly amplified using a chirped-pulse amplification (CPA) scheme, where the pulses are stretched in time before amplification to reduce the peak power and thus the accumulated nonlinear phase. Additionally, pulse-pickers may be needed to reduce the repetition rate of the laser, and one or more pre-amplifiers are often used before the final stage of amplification [1].

Giant-chirp oscillators (GCOs) are an extension of dissipative soliton lasers to cavities with large dispersion (and thus typically low repetition rate). In this limit, the pulse acquires a “giant-chirp” and is stretched in time to a larger degree than is accounted for by the cavity dispersion. Since these lasers naturally produce high energy pulses with very long durations, they provide a route to simplifying CPA by potentially eliminating the need to have a pulse picker and stretcher. In initial experimental demonstrations, a dissipative soliton GCO was used to generate pulses with up to 20 nJ of pulse energy with chirped durations out to 140 ps. They can be de-chirped to around twice the transform limit, achieving final pulse durations greater than 800 fs [2]. This chapter will discuss extensions of the GCO concept and low repetition rate lasers, focusing on cavities that have the potential to produce shorter final pulse durations.

2.2 All-normal dispersion dissipative soliton giant-chirp oscillators

Although the initial reports of GCOs [2] were encouraging in terms of the ratio of chirped pulse duration to de-chirped pulse duration, the fact that the de-chirped pulse could not reach the transform limit precluded achieving final pulse durations below 500 fs. This section will summarize attempts to optimize these results.

2.2.1 Modeling

Simulations for a dissipative soliton GCO are conducted using the split-step method as described in the Introduction. The gain fiber is fixed at 70 cm and is followed by 50 cm of single mode fiber (SMF). The amount of SMF before the gain fiber is varied. The saturation energy of the gain fiber begins at 3.3 nJ and is increased to change the converged pulse energy from the laser. The saturable absorber is modeled as an ideal curve with a modulation depth of 70%. The laser cavity has 70% output coupling, and an additional 40% linear loss is assumed to account for other experimental losses.

The GCO is simulated with 10 m, 50 m, and 100 m of passive fiber added before the gain fiber, which correspond to repetition rates of 17.9 MHz, 3.9 MHz, and 2.0 MHz, respectively. Both the intra-cavity filter bandwidth and the converged pulse energy are varied in these cavities, and the results are summarized in Fig. 2.1. As the repetition rate of the laser is lowered, the bandwidth of the output spectrum is reduced, meaning that the transform limit of the pulse is increased. The output pulse duration also becomes longer at lower repetition rates.

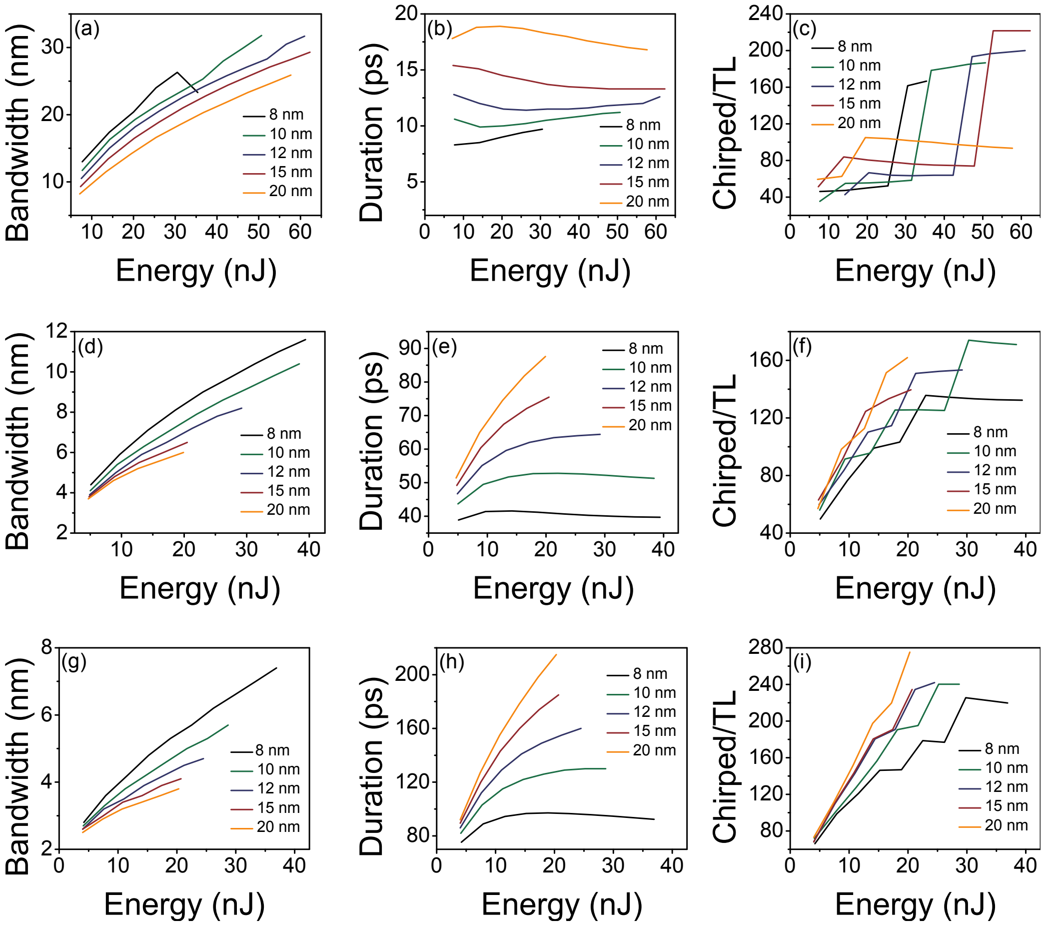

Figure 2.1: GCO simulations for various filter bandwidths. (a)-(c) Output bandwidth, output pulse duration, and ratio of the output chirped pulse duration to the transform limit for the 17.9 MHz cavity. (d)-(f) Output bandwidth, output pulse duration, and ratio of the output chirped pulse duration to the transform limit for the 3.9 MHz cavity. (g)-(i) Output bandwidth, output pulse duration, and ratio of the output chirped pulse duration to the transform limit for the 2.0 MHz cavity.

For the purposes of CPA, a highly chirped output pulse with a short transform limited pulse duration is desirable. For a given converged pulse energy, Fig. 2.1 (c), (f), and (i) show that the lower repetition rate cavity will have the larger ratio of chirped pulse duration to transform limit. However, for the 100 m cavity, the spectral bandwidths are less than 8 nm, so the de-chirped pulse duration will be limited to hundreds of femtoseconds at best. To consider the limitation this imposes on the performance of GCOs, it is instructive to note that for the experimentally realizable pulse energies of up to 25 nJ [2], the ratio of chirped pulse duration to transform limited duration does not exceed around 150 and the de-chirped pulse duration will be close to 1 ps long. This trend imposes the main limitation on dissipative soliton GCOs for applications where femtosecond pulses are desired.

2.2.2 Experiments

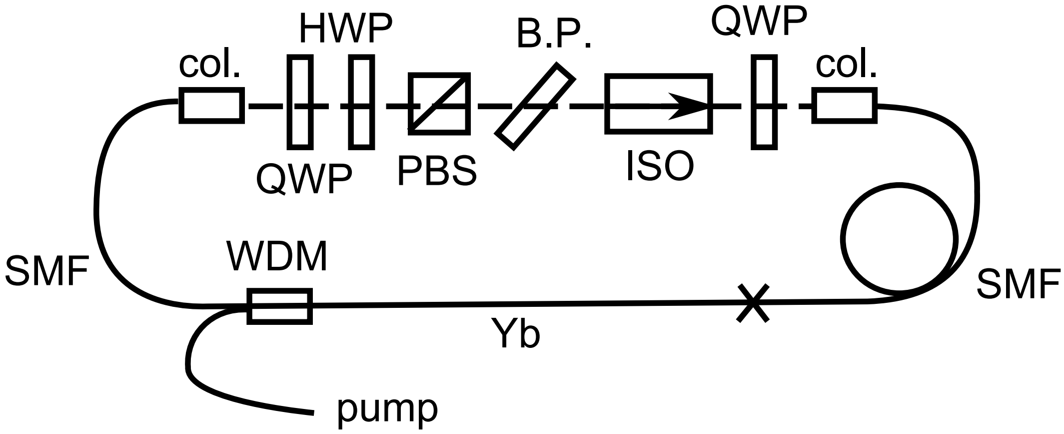

Figure 2.2: GCO cavity design. SMF: single mode fiber; Yb: Ytterbium-doped fiber; WDM: wavelength division multiplexer; col.: collimator, QWP: quarter-wave plate; HWP: half-wave plate; PBS: polarizing beam splitter; ISO: isolator.

The experimental cavity for a GCO mode-locked with nonlinear polarization evolution (NPE) is shown in Fig. 2.2. Around 50 m of SMF is used before the gain fiber to give a repetition rate of 4.2 MHz. This cavity is studied to see if optimization of the de-chirping stage can yield shorter pulse durations than the 880 fs de-chirped duration presented in reference [2]. Two mode-locked results are shown in Fig. 2.3. These results are similar to those achieved previously for this cavity with respect to the fact that the de-chirped duration for both pulses deviates from the transform limit by a factor of two or more. The de-chirping is performed with a pair of reflection gratings with a line density of 1600 lines/mm with a 70° angle of incidence, which is chosen to reduce the ratio of group-velocity dispersion (GVD) to third-order dispersion (TOD). These results indicate that it will be challenging to achieve shorter pulses from this type of laser cavity, due both to the narrow mode-locked spectra and the persistent deviation from the transform limited duration after de-chirping.

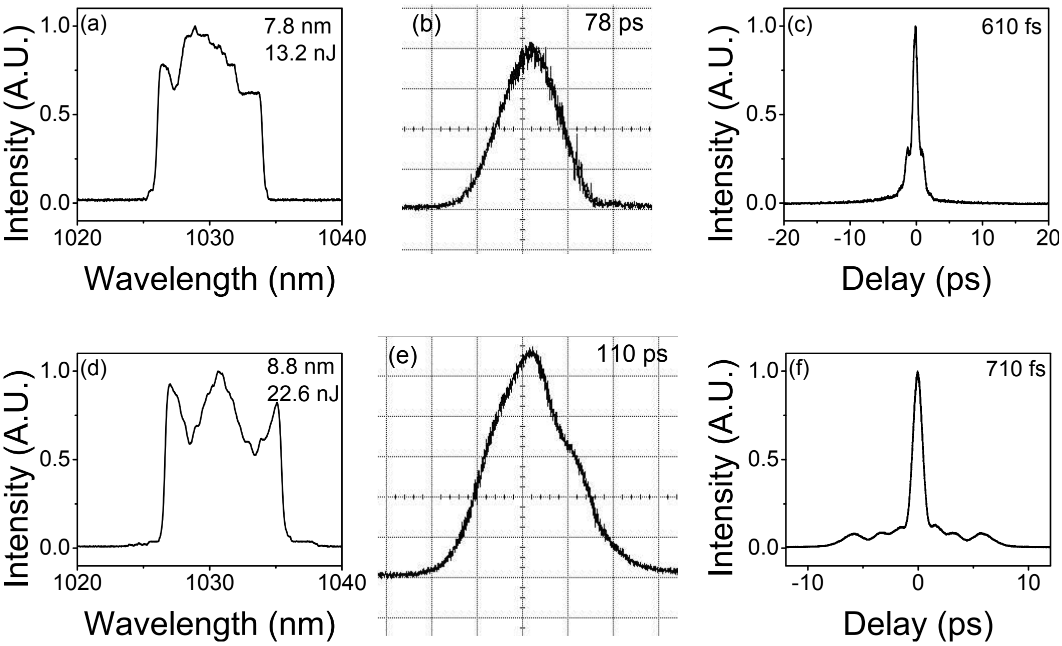

Figure 2.3: Mode-locked results from 4.2 MHz GCO. (a) Spectrum, (b) chirped pulse, and (c) de-chirped pulse from cavity with an 8 nm spectral filter. (d) Spectrum, (e) chirped pulse, and (f) de-chirped pulse from cavity with a 10 nm spectral filter.

2.2.3 Extension to cavities with polarization-maintaining fiber

Among recent reports of dissipative soliton GCOs, the largest ratios of chirped pulse duration to de-chirped pulse duration are from all-fiber cavities primarily composed of polarization-maintaining (PM) fiber. NPE is implemented through non-PM gain fiber and a short segment of SMF after the gain fiber [3, 4]. In the initial report with 30 m of PM fiber before the gain fiber (7 MHz repetition rate), a 20 nJ, 30 ps pulse is de-chirped to 200 fs, which is only 25% longer than the transform limited duration of 160 fs [3]. By increasing the length of PM fiber before the gain to 120 m, up to 25 nJ pulses with 70 ps durations are generated and can be de-chirped down to 300 fs. This represents a record-breaking ratio of chirped to de-chirped pulse duration of over 200 [4]. These cavities have no explicit spectral filter; the filtering comes from the wavelength division multiplexer (WDM) and the interplay between a gain spectrum centered at 1010 nm and stimulated Raman scattering (SRS). Interestingly, both of these lasers exhibit coherent dissipative soliton pulses, even in the presence of noisy Raman pulses generated through SRS. This is in contrast to the work reported in reference [5], which correlates the presence of a Raman pulse with destabilization of the dissipative soliton pulse. Aguergaray *et al.* attribute this difference to the fact that they do have a discrete spectral filter in their cavity, which ensures that the Raman pulse starts from noise each round trip. This is in contrast to the laser cavities in [3, 4], where the authors hypothesize that the absence of a filter may allow feedback of the Raman pulse, enabling it to stabilize over multiple round trips.

We construct the 7.2 MHz all-fiber laser cavity depicted in reference [3] with a few changes to components. Most notably, the core-pumped gain fiber we use (Yb-501 from CorActive) lases closer to 1030 nm, and we use a non-filtering WDM. We are unable to find stable mode-locking with this laser cavity. Since the spectral filtering is the largest difference between the two cavities, we then add a free space-section to the laser cavity as shown in Fig. 2.4 to implement spectral filtering with a birefringent plate. Noise bursts with accompanying Raman pulses are still easy to find in this cavity; an example is shown in Fig. 2.5. Mode-locked states are

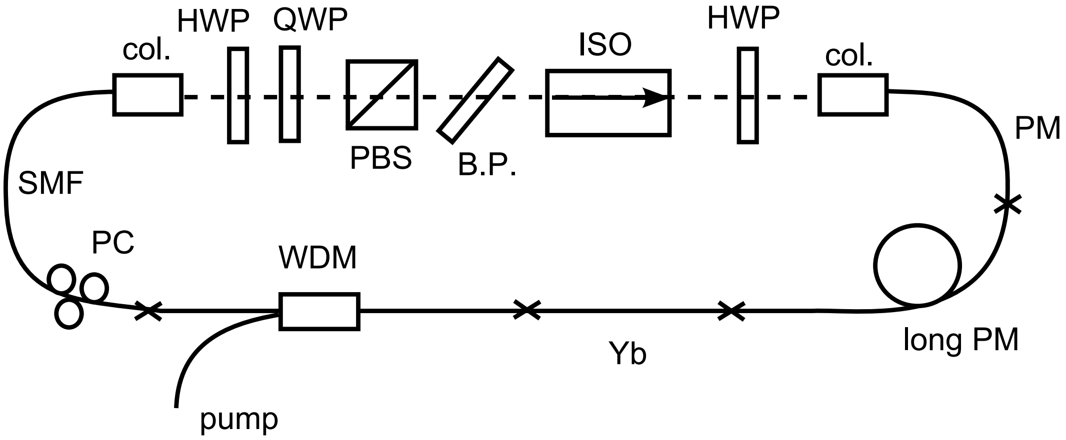

Figure 2.4: PM GCO cavity design. SMF: single mode fiber; PM: polarization maintaining fiber; Yb: Ytterbium-doped fiber; WDM: wavelength division multiplexer; PC: polarization controller; col.: collimator, QWP: quarter-wave plate; HWP: half-wave plate; PBS: polarizing beam splitter; ISO: isolator.

also found in the cavity, both with Raman pulses and without Raman pulses, as shown in Fig. 2.6. However, the de-chirped durations for these pulses also deviate from the transform limit by a noticeable amount, not providing a significant improvement over the results presented in the previous section.

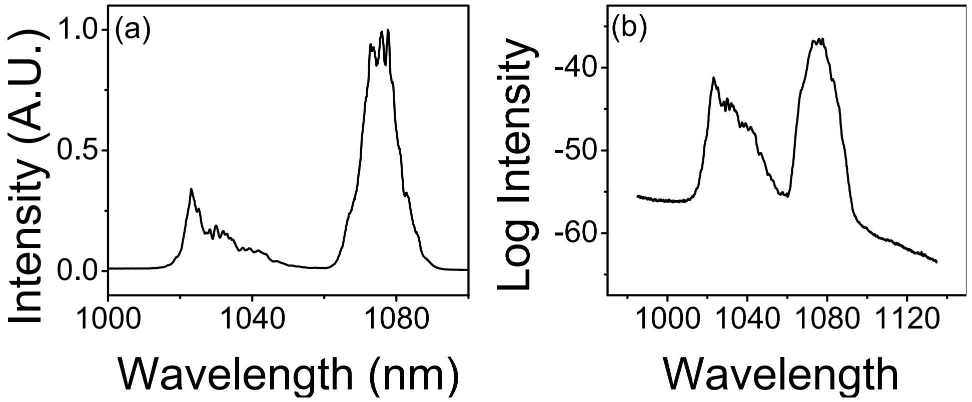

Figure 2.5: Spectra for noise-like pulses from a GCO with 30 m of PM fiber before the gain and an 8 nm spectral filter on (a) linear and (b) log scales.

There are two main differences between the mostly PM cavity and the cavity discussed in the previous section. The first is the restriction of NPE to a 1-2 m segment of the cavity, rather than NPE occurring throughout the whole cavity. The

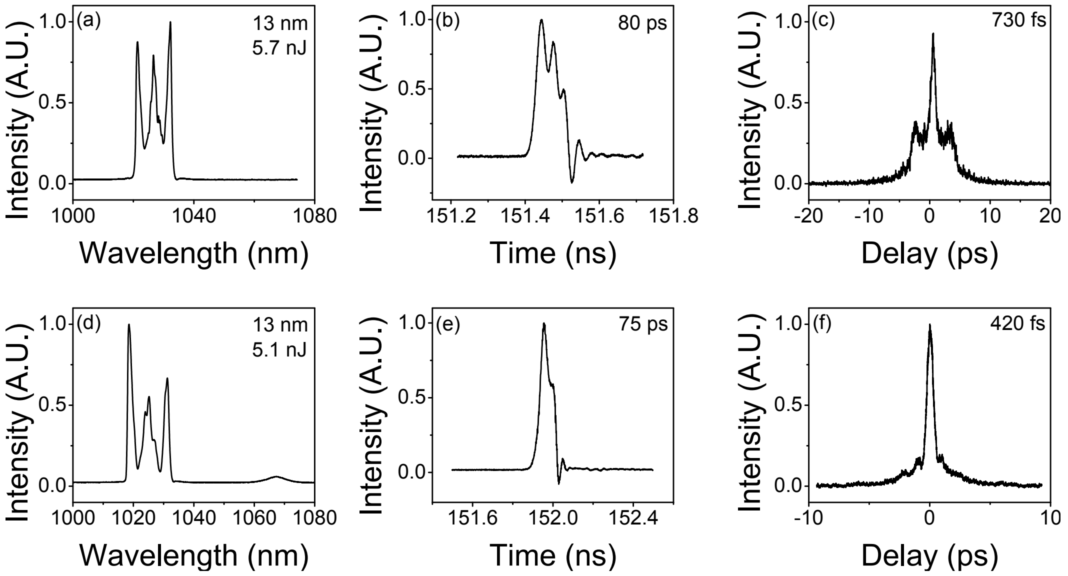

Figure 2.6: Spectra for mode-locked pulses from a GCO with 30 m of PM fiber before the gain: (a) spectrum, (b) chirped pulse, and (c) de-chirped pulse from cavity with a 12 nm spectral filter and (d) spectrum, (e) chirped pulse, and (f) de-chirped pulse from cavity with a 20 nm spectral filter.

second is the difference in filtering mechanism between the results of references [3, 4] and the dissipative soliton lasers that rely on a discrete filter. Since the experiments shown here with the restricted NPE segment and the birefringent filter do not replicate the performance demonstrated in reference [3], we suspect that the filtering mechanism is the important design parameter in achieving pulses that de-chirp closer to the transform limit.

2.3 Amplifier similariton low repetition rate oscillators

Amplifier similariton lasers are typically able to achieve shorter pulses than dissipative soliton lasers [6]. Therefore, at low repetition rates, they may enable an easier route to pulses with a large ratio between the output duration and the transform limited duration. However, in contrast to the dissipative soliton lasers, the pulse properties of the amplifier similariton laser are determined by the parabolic attraction in the gain fiber, so these pulses are less likely to acquire chirp many times greater than the cavity dispersion. Thus, the long output pulse durations are determined more by linear stretching in the long lengths of fiber inside of the low repetition rate cavity.

The performance of low repetition-rate amplifier similariton lasers are assessed in simulation and experiment. Multiple cavity designs are explored experimentally, and the practical limitations of the various implementations are discussed.

2.3.1 Modeling

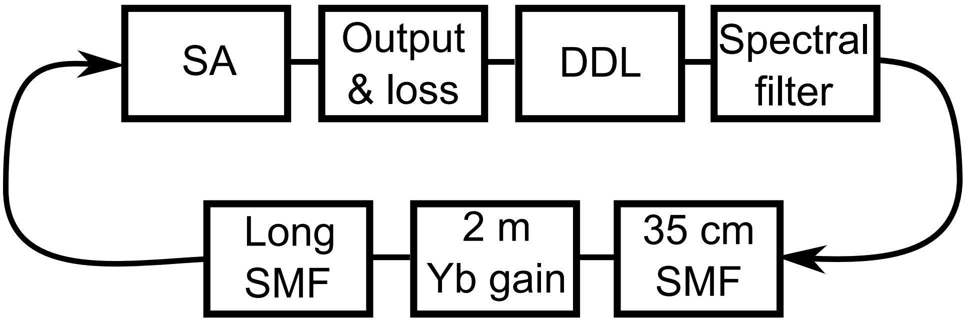

Figure 2.7: Schematic of simulated low repetition rate amplifier similariton cavity. SA: saturable absorber; DDL: dispersive delay line; SMF: single mode fiber.

The simulated cavity is depicted in Fig. 2.7. The narrow-band spectral filter serves the purpose of seeding the gain fiber with a pulse close to the asymptotic solution. In order to avoid perturbing the pulse between the spectral filter and the gain fiber, the additional passive fiber used to lower the repetition rate is added after the gain fiber, unlike in the dissipative soliton GCO. This positioning allows the pulse to be stretched before taking the output. After the output, a grating pair is used to compensate the large normal dispersion experienced by the pulse. Without the dispersion compensation, the pulse entering the gain fiber will have additional chirp and will thus not be as good an approximation to the asymptotic solution, which tends to produce output pulses with less bandwidth and lower energy.

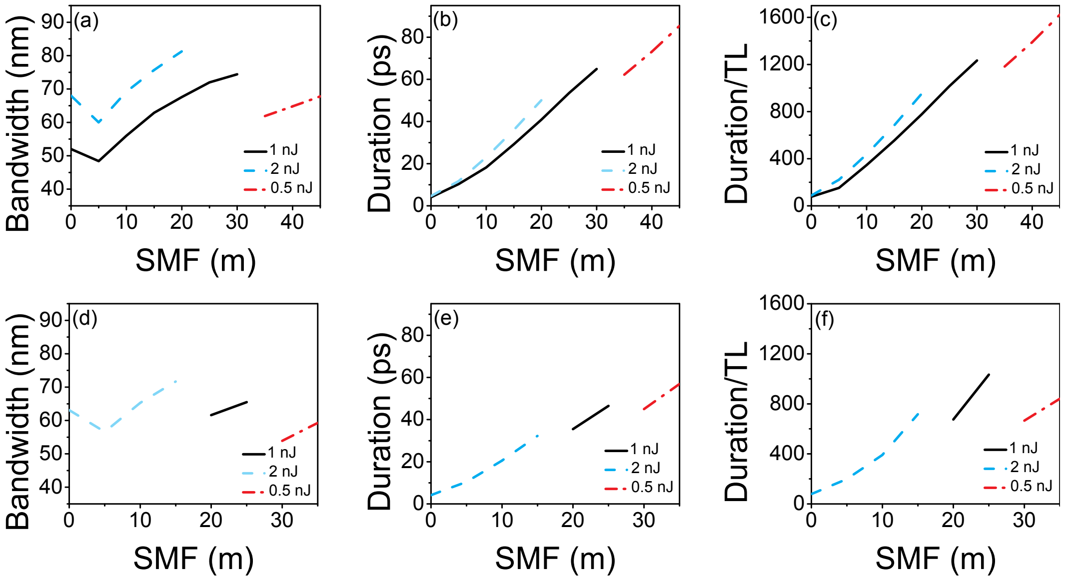

Figure 2.8: Simulation results for low repetition rate amplifier similariton lasers. (a)-(c) Output bandwidth, output pulse duration, and ratio of chirped pulse duration to transform limited duration for laser cavities with a 4 nm spectral filter. (d)-(f) Output bandwidth, output pulse duration, and ratio of chirped pulse duration to transform limited duration for laser cavities with a 2 nm spectral filter.

The simulation results are summarized in Fig. 2.8. The length of passive fiber after the gain is increased, and the saturation energy of the gain fiber is set to yield converged pulse energies of 1 nJ, 2 nJ, or 0.5 nJ. Note that the lower energy pulses converge for lower amounts of fiber as well, but these simulations were neglected in favor of the more desirable higher-energy states. The anomalous dispersion provided by the dispersive delay line is set to maintain a net cavity dispersion around 90,000 fs^2. As the amount of passive fiber after the gain is increased, the spectral bandwidth of the pulse increases under the action of self-phase modulation. The pulse will also acquire additional chirp after the gain, which results in an increasing output pulse duration with added fiber. As can be seen in

Fig. 2.8(c) and Fig. 2.8(f), amplifier similariton pulses can achieve much higher ratios of chirped pulse duration to transform limited duration than dissipative soliton pulses. This highlights an advantage of the amplifier similariton lasers: since the cavity is stabilized by the local attraction in the gain, the stretching of the pulse in other segments of the cavity is largely independent of the laser achieving a self-consistent solution as long as the pulse is re-set to its initial condition before entering the gain fiber. This is in contrast to the dissipative soliton laser, where adding large amounts of passive fiber exerts a strong influence on the average cavity solution.

Fig. 2.8 also shows that larger bandwidths and longer pulses can be achieved when using a 4 nm spectral filter instead of a 2 nm filter. For spectral filter bandwidths beyond 4 nm, the laser will tend towards dissipative soliton mode-locking, and with narrower filters, the output bandwidth will be narrowed further [6].

As indicated in Fig. 2.8, it is harder to achieve higher pulse energies as more passive fiber is added to the cavity. To analyze this observation further, the nonlinear phase accumulation within the cavity is considered and shown in Fig. 2.9. For the three converged pulse energies, the amount of nonlinear phase accumulation seems to be leveling off before 20π. This indicates that total nonlinear phase accumulation may pose a limitation to mode-locking the higher-energy amplifier similariton pulses in longer cavities.

To reduce the nonlinear phase accumulation in the cavity, laser cavities with the long length of passive fiber appearing before the gain are also considered. In order to match the experiments presented in the next section, the DDL is placed before the long length of passive fiber, so the long chirped pulse is measured at

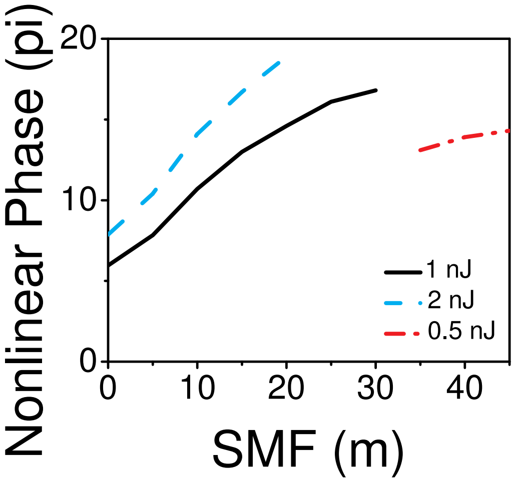

Figure 2.9: Nonlinear phase accumulation in the low repetition rate amplifier similariton laser cavity with a 4 nm spectral filter.

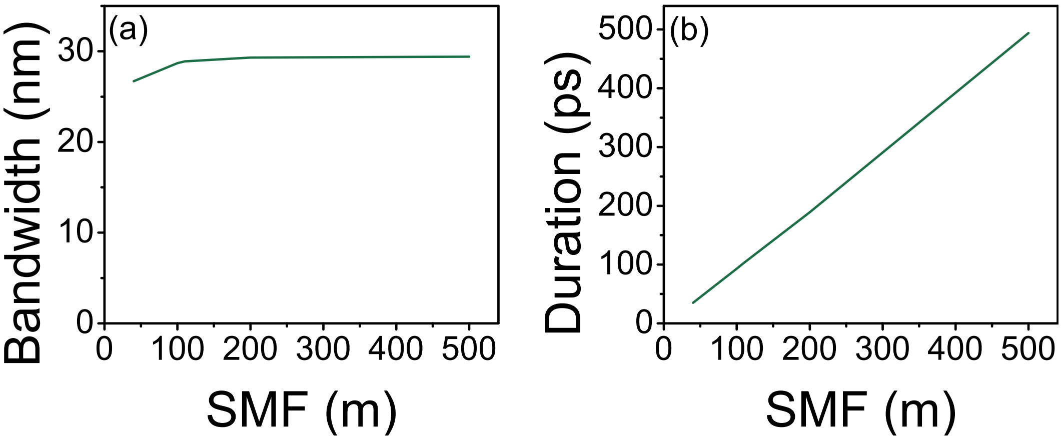

Figure 2.10: Simulated (a) output bandwidth and (b) down-chirped pulse duration for a low repetition rate dispersion managed amplifier similariton laser. The converged pulse energy is 2 nJ

this point in the cavity and is down-chirped rather than up-chirped. The pulse is then de-chirped as it propagates through the long length of passive fiber. The simulations shown in Fig. 2.10 all have converged pulse energies of 2 nJ, indicating that higher pulse energies can be achieved in this configuration. Indeed, passive fiber lengths up to 500 m have been simulated for this cavity. As expected, the stretched pulse duration increases linearly with added dispersion, and the output bandwidth remains nearly constant.

2.3.2 Experiment

Design 1: Passive fiber after the gain

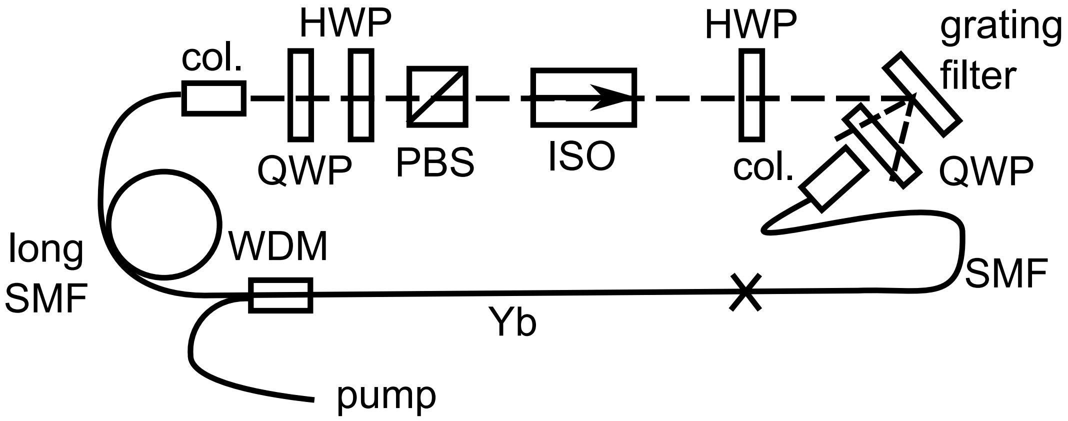

Figure 2.11: Schematic of amplifier similariton cavity with long length of fiber after the gain. HWP: half-wave plate; QWP: quarter-wave plate; PBS: polarizing beam splitter; ISO: isolator; col.: collimator; SMF: single mode fiber.

The laser cavity shown in Fig. 2.11, which does not have a DDL, is considered first. The purpose of these initial experiments is to assess mode-locking as passive fiber is added after the gain without the additional loss that will be introduced with the DDL. Two factors may limit the laser performance with this set-up. The first is the nonlinear phase accumulation in the cavity since the long length of fiber appears where the pulse is its most energetic. The second is the chirp the pulse acquires in the passive fiber. Especially without the DDL, the added chirp will cause the pulse entering the gain fiber to deviate more from the asymptotic solution, which may limit the laser performance.

The gain fiber in these cavities is approximately 3-4 m of Yb-gain fiber (CorActive SCF-YB25-6/125-13), which is counter-pumped by a WDM (Lightel). The gain fiber is preceded by 10 cm of passive fiber, and the amount of passive fiber after the gain is varied. An approximately 4 nm filter can be formed by placing a 300 lines/mm grating around 10 cm from a 1 mm aspheric lens collimator; 2 nm bandwidths are achieved by using a 600 lines/mm grating the same distance from the collimator. The additional half-wave plate before the grating filter serves to maximize the diffraction efficiency of the grating.

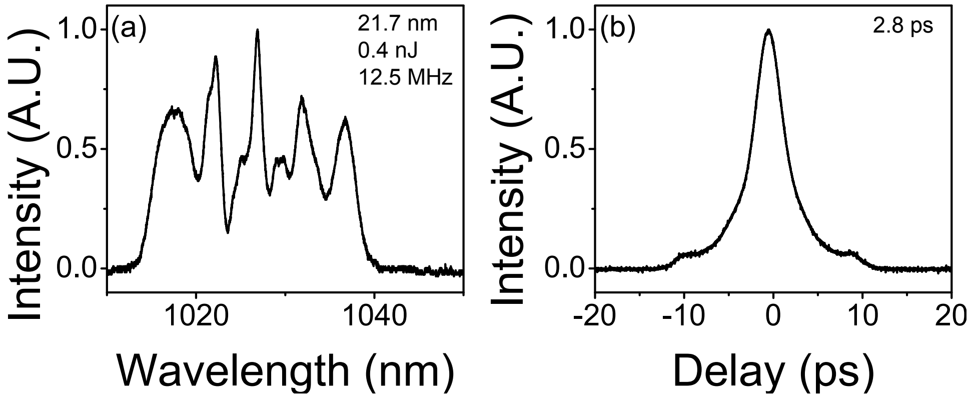

Figure 2.12: Mode-locked result from a 12.5 MHz Yb-doped amplifier similariton laser: (a) spectrum and (b) autocorrelation of chirped pulse.

Fig. 2.12 shows a typical spectrum and autocorrelation of the chirped output pulse for a cavity with 10 m of passive fiber after the gain fiber. The 2 nm intra-cavity spectral filter is used to avoid mode-locking dissipative soliton-like spectra. The output spectrum is over 20 nm at the base, which is less than the over 40 nm achieved with higher repetition-rate amplifier similariton lasers [6], and the pulse energy is quite limited at 0.4 nJ. It is difficult to mode-lock this cavity with energies above 0.5 nJ. The chirped pulse duration, 2.8 ps, is much less than predicted by the simulations shown in Fig. 2.8(e). This is likely symptomatic of the difficulty of mode-locking high energy, broad bandwidth spectra in this cavity and indicates that hundreds of meters of passive fiber may be needed to achieve stretched pulse durations greater than 100 ps. As is often (but not always; see amplifier similariton spectra in Chapter 4) the case, continuous-wave breakthrough can also be observed on the mode-locked spectrum.

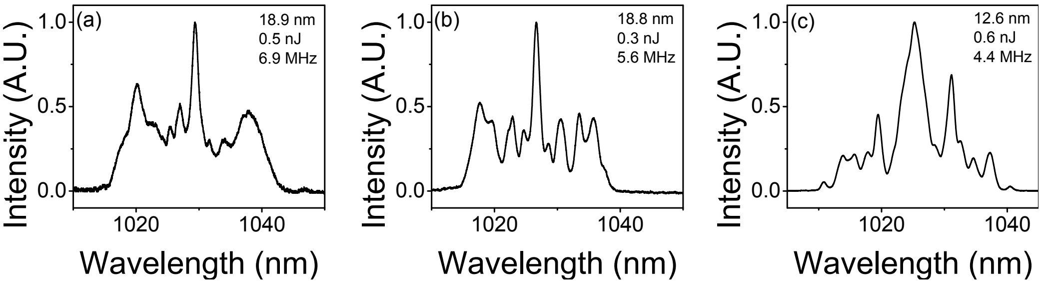

Figure 2.13: Mode-locked spectra from low repetition rate Yb-doped amplifier similariton lasers: (a) 6.9 MHz. (b) 5.6 MHz. (c) 4.4 MHz.

Fig. 2.13 shows example output spectra from this laser as the repetition rate is lowered further by adding passive fiber in approximately 10 m increments. The pulse energy stays in the 0.5 nJ range and the spectral bandwidths have a tendency to decrease, which could be symptomatic of the extra chirp and nonlinear phase causing the pulse seeding the gain fiber to be further from the asymptotic solution. It is also very challenging to achieve single-pulsing operation with this laser since the 0.5 nJ pulse energy only corresponds to a few milliwatts of average power.

To test the influence of the extra chirp the pulse acquires in the passive fiber, a grating pair is inserted between the isolator and the grating filter in the 40 m cavity depicted in Fig. 2.11. Low-loss transmission gratings (LightSmyth Technologies, 1000 lines/mm) are used. An example mode-locked spectrum is shown in Fig. 2.14. The spectral bandwidth from this laser has increased, confirming that the uncompensated chirp limits the laser performance to some extent. However, finding single-pulsing states in this cavity remains extremely difficult.

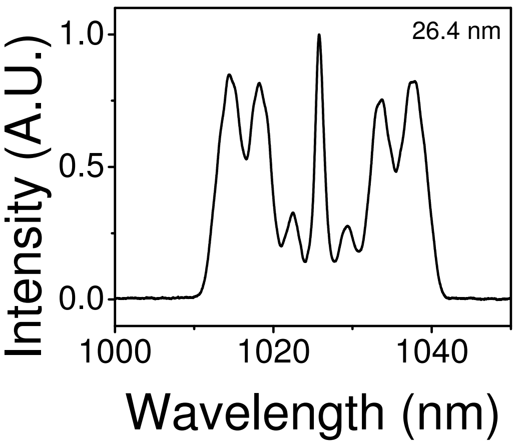

Figure 2.14: Mode-locked spectrum from a multi-pulsing state of an Yb-doped dispersion managed amplifier similariton laser.

Design 2: Passive fiber before the gain with dispersion management

The results shown in the previous section indicate that increasing amounts of nonlinear phase accumulation and uncompensated normal dispersion limit the laser performance. To reduce the nonlinear phase accumulation in the cavity, the long length of SMF is moved from after the gain fiber to before the gain fiber as shown in Fig. 2.15. In this cavity, the temporal stretching is almost entirely linear since the long segment of passive fiber appears where the pulse energy is at its lowest. It should also be noted that the pulse in this cavity is never up-chirped to a long duration; instead, the pulse is down-chirped to its longest duration after the grating pair and is then de-chirped in the passive fiber before the gain. To achieve an up-chirped pulse, the ordering of the fiber and the DDL would need to be switched. However, placing the fiber first would necessitate the use of another collimator pair to use the grating pair as the DDL, which would significantly increase the loss in the cavity. Thus, the grating pair is placed first to assess the concept.

To minimize loss in the cavity, a pair of plastic 1750 lines/mm transmission

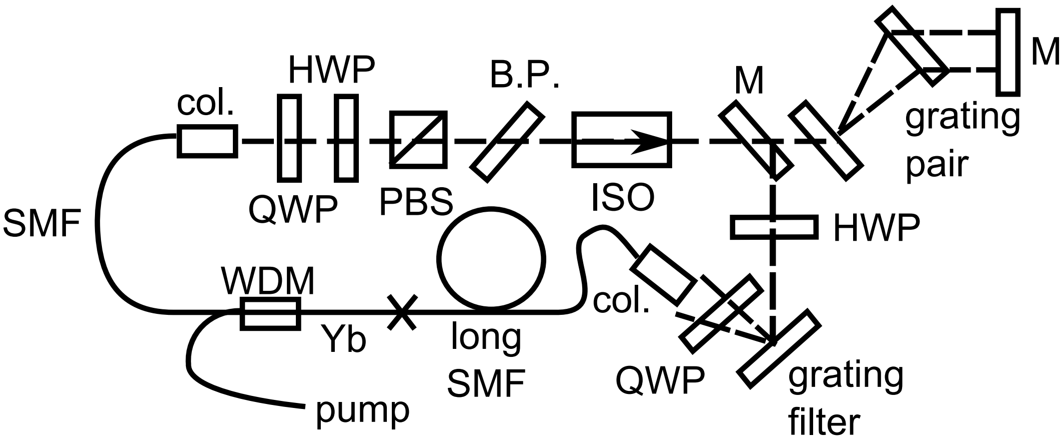

Figure 2.15: Cavity schematic of dispersion managed amplifier similariton laser with the long length of passive fiber before the gain. HWP: half-wave plate; QWP: quarter-wave plate; PBS: polarizing beam splitter; ISO: isolator; M: mirror; col.: collimator; SMF: single mode fiber.

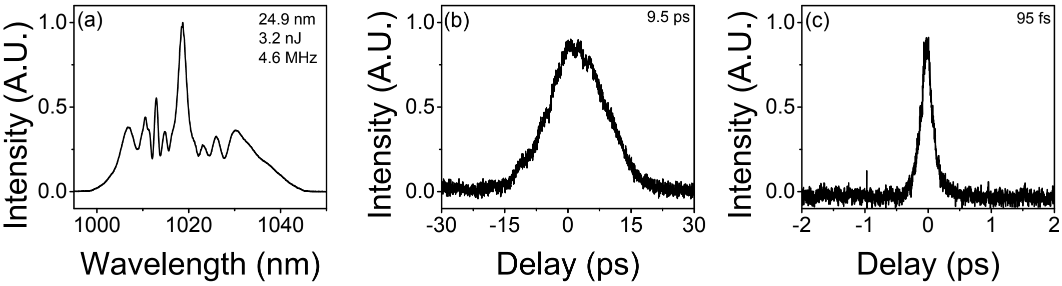

Figure 2.16: Mode-locked result for a dispersion managed amplifier similariton laser at 4.6 MHz: (a) spectrum; (b) down-chirped pulse duration (taken from grating filter reflection); and (c) de-chirped output pulse.

gratings are used for the DDL. A mode-locked pulse is shown in Fig. 2.16 for a 40 m cavity (4.6 MHz). The achievable single-pulse energy of 3 nJ is higher for this laser cavity than the cavity described in the previous section, indicating that reducing the nonlinear phase accumulation in the cavity may be beneficial. CW-breakthrough is still visible on the spectrum, and it is still non-trivial to find single-pulsing states. The duration of the down-chirped pulse is measured by taking an intensity autocorrelation of the portion of the pulse reflected from the grating filter. The output pulse from the polarizing beam splitter (PBS) is de-chirped to show coherence.

Since nonlinear phase accumulation is less of a limitation in this cavity, much longer lengths of fiber can be tolerated. Around 200 m of passive fiber is added before the gain fiber, and the grating spacing is adjusted to maintain a comparable net dispersion. Interestingly, the cavity does not mode-lock using the same plastic transmission gratings, but does when they are replaced with 1400 lines/mm reflection gratings that introduce an order of magnitude less third-order dispersion (TOD). Since the reflection gratings introduce more loss into the cavity, this indicates that excessive TOD may impact amplifier similariton mode-locking. Simulations of TOD in amplifier similariton lasers shows that TOD on the order of 10^7 fs^3 starts to result in pulse distortions that preclude stable mode-locking.

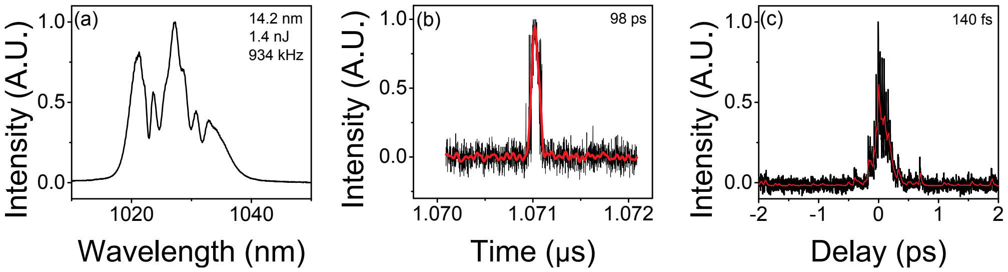

Figure 2.17: Mode-locked result for a dispersion managed amplifier similariton laser at 934 kHz: (a) spectrum; (b) down-chirped pulse duration (taken from grating filter reflection); and (c) de-chirped output pulse. The dips observed in the intensity autocorrelation in (c) result from using the Femtochrome autocorrelator at low repetition rate.

The mode-locked results for the 934 kHz cavity are shown in Fig. 2.17. The down-chirped pulse from the grating filter reflection has been stretched to around 98 ps, and the output pulse from the PBS is de-chirped to under 150 fs. Single-pulsing is very difficult to find in the cavity, in part due to the large loss coming from the reflection gratings.

Design 3: Passive fiber before the gain with chirped fiber Bragg grating

In order to achieve an up-chirped pulse using a cavity design similar to the one presented in the previous section, the order of the DDL and the passive fiber needs to be reversed. If a grating pair is used to provide the anomalous dispersion, this would necessitate using another collimator pair to place the gratings between the long passive fiber and the gain fiber, which would introduce significantly more loss. Instead, a chirped fiber Bragg grating (CFBG) is used to provide the anomalous dispersion in a fiber format. The ideal cavity layout is shown in Fig. 2.18.

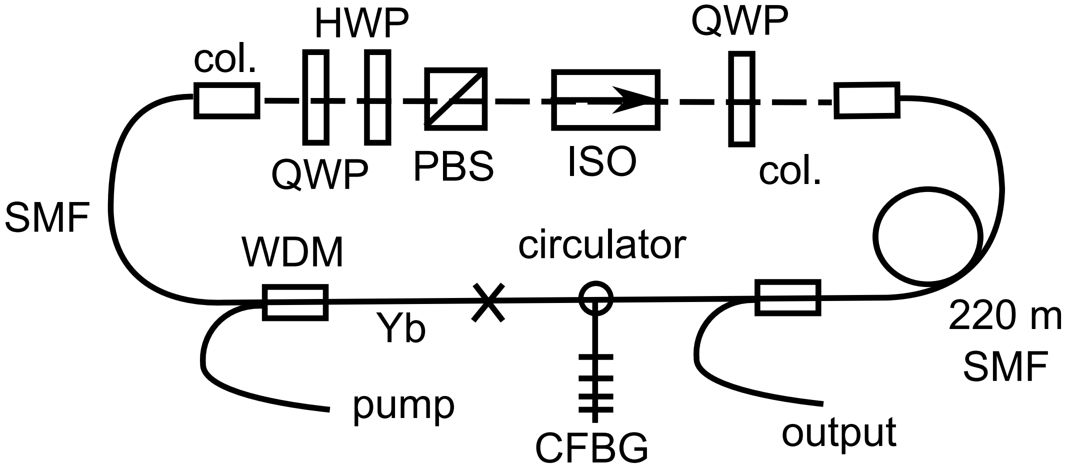

Figure 2.18: Schematic of amplifier similariton cavity with chirped fiber Bragg grating. HWP: half-wave plate; QWP: quarter-wave plate; PBS: polarizing beam splitter; ISO: isolator; col.: collimator; SMF: single mode fiber; CFBG: chirped fiber Bragg grating.

The CFBG (TeraXion) provides a 3.2 nm Gaussian filter at 1030 nm and imparts -5 ps^2 of anomalous dispersion. This balances the normal dispersion from the 220 m of HI1060 (Corning) single mode fiber that precedes it in the cavity. The grating filter is removed since the CFBG provides the narrow bandwidth spectral filter. As an additional advantage over the grating pair, the CFBG does not introduce any TOD.

Experimentally, the CFBG is implemented in the cavity using a polarization insensitive circulator (Haphit). Mode-locking was not found using the configuration shown in Fig. 2.18. The cavity mode-locks with extreme difficulty when the circulator and CFBG are placed before the 220 m length of fiber. One possibility for this difficulty is the specifications of the circulator; it has an insertion loss of around 4 dB and a return loss of around 55 dB, which could cause back reflections that inhibit mode-locking.

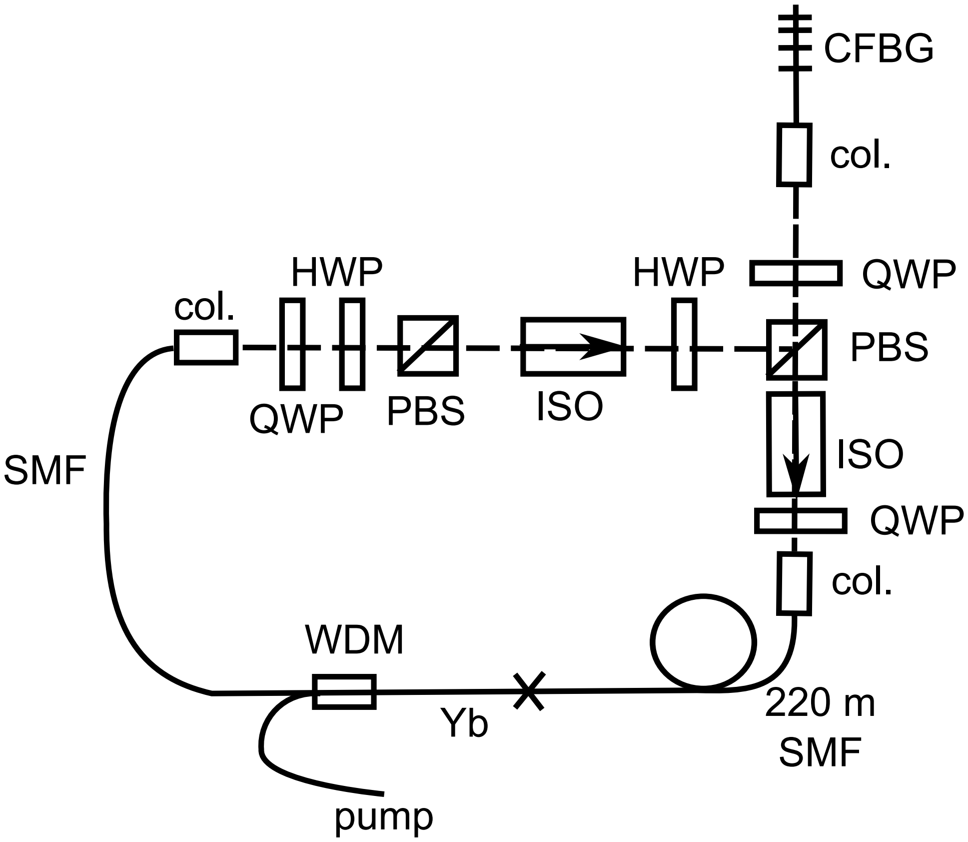

Figure 2.19: Schematic of amplifier similariton sigma cavity with chirped fiber Bragg grating. HWP: half-wave plate; QWP: quarter-wave plate; PBS: polarizing beam splitter; ISO: isolator; col.: collimator; SMF: single mode fiber; CFBG: chirped fiber Bragg grating.

To eliminate the circulator as a source of uncertainty in the cavity and test the performance of the CFBG by itself, the sigma cavity shown in Fig. 2.19 is constructed. This laser mode-locks more easily than with the circulator, indicating that the implementation of this laser design may need to wait on a 1030 nm circulator with better return loss specifications. Single-pulsing states remain challenging to find. Example mode-locked spectra are shown in Fig. 2.20.

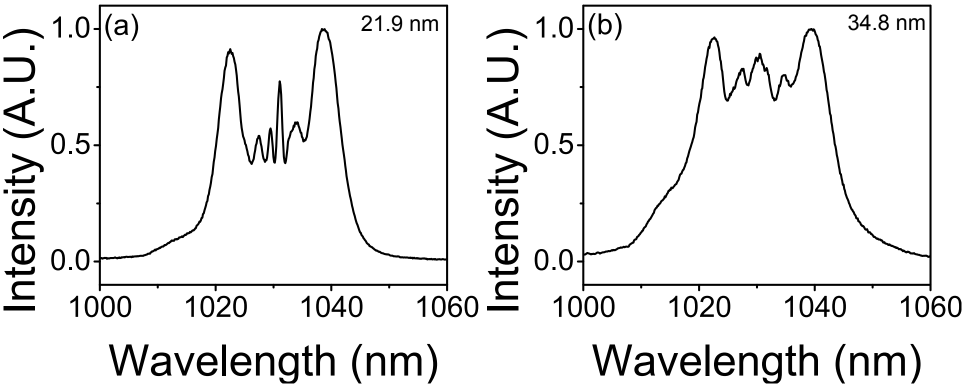

Figure 2.20: Mode-locked spectra from laser cavity shown in Fig. 2.19.

2.4 Erbium-doped amplifier similariton lasers at low repletion-rate

At repetition rates of tens of megahertz, the Er-doped amplifier similariton laser can provide sub-100 fs pulses with over 3 nJ of pulse energy [7]. Both normal and anomalous dispersion passive fibers exist at the 1550 nm lasing wavelength of erbium-doped fiber, so the Er-doped amplifier similariton fiber laser can circumvent the extra loss that must be introduced to the 1030 nm fiber lasers when adding dispersion management. This section describes preliminary experiments on low repetition rate Er-doped amplifier similariton lasers.

The cavity schematic is shown in Fig. 2.21. Here, a 600 lines/mm grating and a 0.5 mm graded-index collimator form a 4 nm spectral filter. SMF-28e+ (Corning) and MetroCor (Corning) are used for the anomalous and normal dispersion fibers,

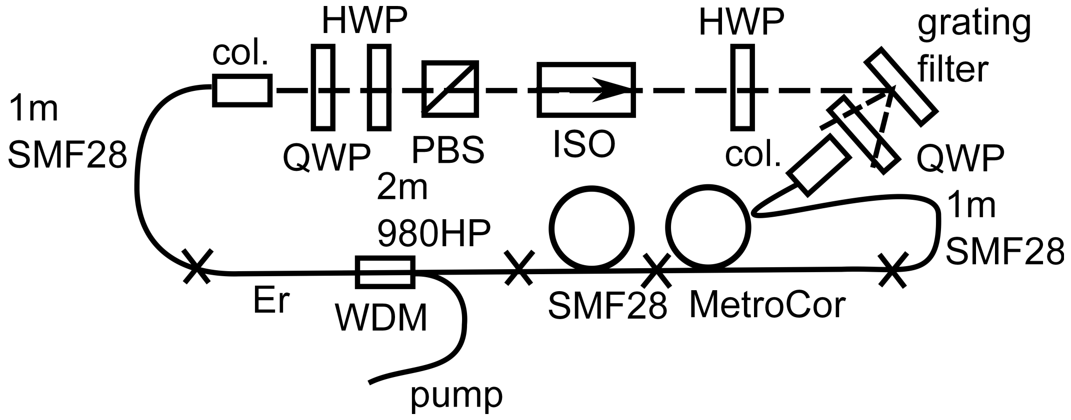

Figure 2.21: Schematic of erbium-doped amplifier similariton cavity. HWP: half-wave plate; QWP: quarter-wave plate; PBS: polarizing beam splitter; ISO: isolator; col.: collimator; SMF: single mode fiber.

respectively. The gain segment is 3 m of RedFern erbium-doped gain fiber, which is a normal dispersion fiber with an approximately 3 μm core size. The laser is co-pumped using a WDM (Lightel) with 980HP fiber, and around 1 m of SMF28e+ follows the gain.

The laser is first mode-locked at a repetition rate of 21 MHz (no additional MetroCor or SMF28e+ preceding the gain). Example mode-locked spectra from the PBS output are shown in Figs. 2.22(a) and 2.22(b). Then, MetroCor and SMF28e+ are added in a ratio of about 3.2 to 1 to maintain the same net dispersion. Lasers with repetition rates of 8.7 MHz (Figs. 2.22(c) and (d)) and 2.7 MHz (Figs. 2.22(e) and (f)) are built. Comparable spectral bandwidths are found as the repetition rate is reduced.

The laser is much easier to mode-lock when the cavity is aligned to lase at 1530 nm (rather than 1550 nm). Single pulsing states are still challenging to find, though possibly easier than in the Yb-doped laser. Certainly, the implementation of the dispersion map is simpler in this cavity, so the Er-doped laser may be the better system to assess the low repetition rate amplifier similariton designs.

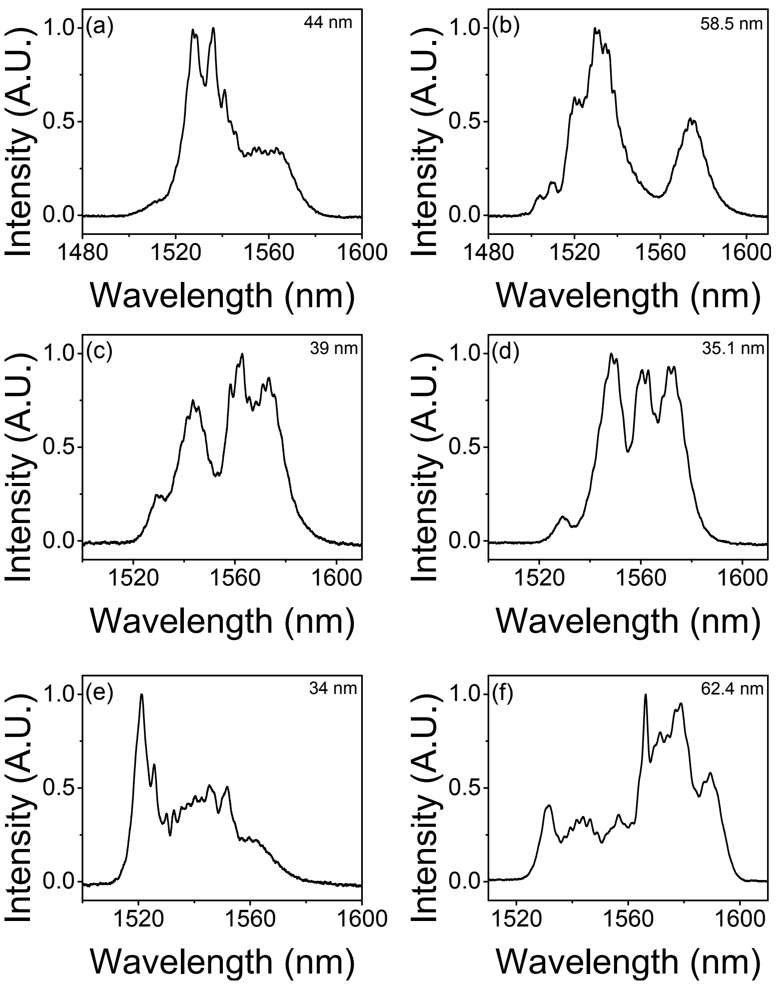

Figure 2.22: Mode-locked spectra from Er-doped dispersion managed amplifier similariton laser at: (a) and (b) 21 MHz; (c) and (d) 8.7 MHz; (e) and (f) 2.7 MHz.

2.5 Conclusion

A few implementations of low repetition rate Yb-doped amplifier similariton lasers have been assessed and show promise for creating long pulses that can be de-chirped to shorter durations than their dissipative soliton counterparts. We find that adding large amounts of fiber to the cavity without dispersion compensation has a tendency to limit the mode-locked bandwidth, so shorter pulses can be achieved by implementing dispersion management. Also, nonlinear phase accumulation is seen to limit the pulse energy; higher energy pulses are achieved when the laser is designed to minimize nonlinear phase accumulation.

In the Yb-doped fiber lasers, implementing the dispersion map is simpler if the long length of SMF can be placed after the gain fiber so that the highly up-chirped output can be taken directly from the NPE rejection port. However, simulations indicate that the amplifier similariton lasers can only tolerate nonlinear phase accumulations on the order of 20π, placing a stricter limit on the amount of SMF that can be used (and thus the chirped pulse duration that can be achieved) after the gain when the pulse energy is at its highest. Nonlinear phase accumulation will also limit the pulse energy from these lasers, and, experimentally, we find pulse energies over 1 nJ are difficult to find even with modest fiber lengths of a few tens of meters.

The nonlinear phase accumulation can be reduced by moving the long length of SMF to before the gain fiber. Pulse energies of up to 3 nJ can be achieved in this configuration, which provides further indication that nonlinear phase accumulation limits the pulse energy in the previously described cavity. When leaving the DDL in the free space section before the long length of SMF, down-chirped pulse durations of around 100 ps can be achieved in a cavity with a 934 kHz repetition rate (approximately 220 m of SMF before the gain). The output pulse from the PBS has the bandwidth to support de-chirped pulse durations below 150 fs. Since the stretching is nearly linear with this design, similar performance should be achievable for an up-chirped pulse by switching the ordering of the DDL and the SMF. However, this cannot be achieved in the Yb-doped fiber laser without introducing significant loss by adding either a second free space section for the DDL or by using a lossy circulator to implement the DDL through a CFBG. Since this cavity design is highly promising otherwise, future work should focus on implementing a low-loss DDL. Assuming a filter with 100% transmission in the pass-band, simulations indicate that additional loss above 80-90% degrades the performance of the laser and cannot be compensated by increasing the pump. The cavity losses should be kept below this to achieve optimal performance.

The dispersion managed amplifier similariton laser is more naturally implemented in an Er-doped fiber laser, where both normal and anomalous dispersion can be provided by standard fibers. Thus, the erbium laser may provide a more natural setting to assess these types of lasers.

BIBLIOGRAPHY

[1] D. Strickland and G. Mourou, Optics Communications **55**, 447 (1985).

[2] W. H. Renninger, A. Chong, and F. W. Wise, Opt. Lett. **33**, 3025 (2008).

[3] D. S. Kharenko, E. V. Podivilov, A. A. Apolonski, and S. A. Babin, Opt. Lett. **37**, 4104 (2012).

[4] A. E. Bednyakova, S. A. Babin, D. S. Kharenko, E. V. Podivilov, M. P. Fedoruk, V. L. Kalashnikov, and A. Apolonski, Opt. Express **21**, 20556 (2013).

[5] C. Aguergaray, A. Runge, M. Erkintalo, and N. G. R. Broderick, Opt. Lett. **38**, 2644 (2013).

[6] W. H. Renninger, A. Chong, and F. W. Wise, Phys. Rev. A **82**, 021805 (2010).

[7] H. Liu, Z. Liu, E. S. Lamb, and F. Wise, Opt. Lett. **39**, 1019 (2014).

CHAPTER 3

DIVIDED-PULSE LASERS[1]

3.1 Introduction

Nonlinear phase accumulation limits the pulse energy from many ultrafast lasers. In particular, this limitation can be severe in fiber lasers. Numerous approaches have been taken to address this issue, including lowering peak power through dispersion management [2], utilizing the linearization of nonlinear phase in self-similar pulse evolutions [3, 4, 5], and mode-locking dissipative solitons in the all-normal dispersion regime, which can tolerate larger nonlinear phase accumulation [6]. The above approaches can be combined with scaling of the core size of the fiber to reduce nonlinear effects [7].

In amplifiers, divided-pulse amplification (DPA) has been demonstrated to reduce peak power and scale pulses to higher energy by temporally dividing the pulse before amplification [8]. For picosecond fiber amplifiers, pulse division has enabled the scaling of peak powers into the megawatt regime [9]. In conjunction with chirped-pulse amplification (CPA), DPA has been used to achieve gigawatt peak powers with 300 fs pulses [10] from a fiber source. In an extension of the DPA technique, pulse division has been used before a nonlinear compression stage to achieve recombined compressed pulses at higher energies than are possible without pulse division [11]. Other recent work has addressed limitations to passive DPA systems, including gain saturation and imperfect division and recombination [12].

Here we propose and demonstrate a divided-pulse laser (DPL), which imple-

---

[1] Much of the work presented in this chapter was published in Optics Letters [1].

ments coherent pulse division and recombination within the laser cavity. In analogy to the temporal pulse division in DPA, the pulse is divided before the gain medium, where most of the nonlinear phase is accumulated, and then recombined before the output to scale the pulse energy. The concept is illustrated schematically in Figure 3.1 using two dividing elements (which yield 4 divided pulses). The technique is demonstrated experimentally in an ytterbium-doped fiber soliton laser, where we achieve 16-times energy scaling utilizing this approach. Initial experimental results for divided-pulse dispersion managed solitons and dissipative solitons will also be presented, along with a discussion of further extensions of the divided-pulse technique. Compared to the combination of a low-energy oscillator and an amplifier designed to reach the same pulse energy, we expect that DPLs may offer higher pulse quality, lower noise, and will require fewer pump lasers.

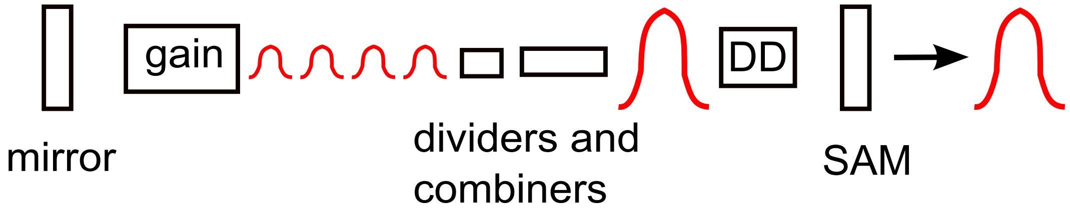

Figure 3.1: Schematic representation of DPL illustrated using two dividing elements. SAM: saturable absorber mirror; DD: dispersive delay, which may or may not be included.

3.2 Divided-pulse soliton laser

As a specific embodiment of the DPL, we construct the fiber soliton laser shown in Fig. 3.2. The birefringence of yttrium orthovanadate crystals is utilized for the pulse division and recombination, as in [8, 9]. The pulse enters the first dividing crystal from a polarizing beam splitter (PBS I) horizontally polarized. The optical axis of the crystal is oriented 45 degrees to the polarization of the incoming pulse,

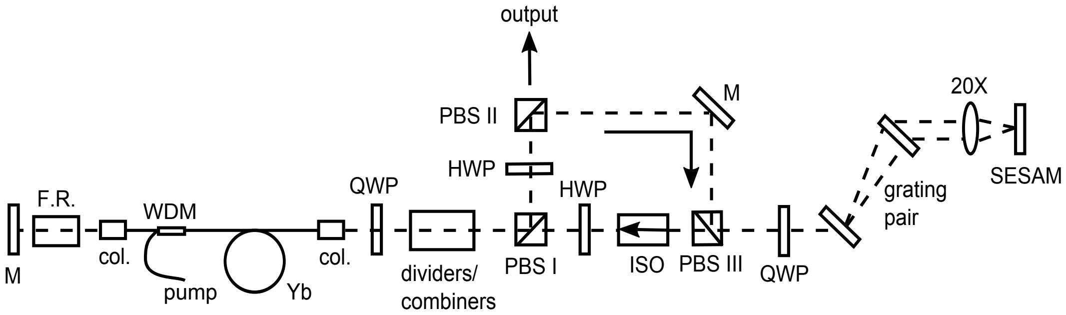

Figure 3.2: Divided-pulse soliton fiber laser. M: mirror; F.R.: Faraday rotator; col.: collimator; WDM: wavelength division multiplexer; QWP: quarter-wave plate; HWP: half-wave plate; PBS: polarizaing beam splitter; ISO: isolator; SESAM: semiconductor saturable absorber mirror.

causing the pulse to split into two copies, one along each axis of the crystal. The two pulses exit the crystal with a time delay induced by the birefringence. Additional dividing crystals are oriented 45 degrees from the preceding crystal so that the splitting process repeats. At the end of N crystals, there will be 2^N copies of the initial pulse. The shortest crystal is selected so that its time delay is greater than the pulse duration. In this experiment, the crystals were arranged from longest to shortest, so neighboring pulse copies have alternating horizontal and vertical polarization at the end of the crystal stack.

The quarter-wave plate (QWP) before the gain fiber converts the polarization of each pulse to circular, which effectively reduces the nonlinear coefficient of the single-mode fiber (SMF) [13], independent of the pulse division. The divided pulses are then amplified in a double-pass through 70 cm of single mode Yb gain fiber (CorActive Yb501), with a Faraday rotator and mirror serving as the retroreflector. The Faraday rotator acts to flip the polarization state of the divided pulses, which is necessary for them to recombine through the same crystal stack. This causes the recombined pulse to become vertically polarized, so it is now reflected by PBS I. The half-wave plate (HWP) and PBS II serve as a variable output coupler. The pulse reflected by PBS II is reflected from a mirror and PBS III to pass through a QWP, a polarization-insensitive grating pair (LightSmyth Technologies LSFSG-1000-3212-HP) to provide the anomalous dispersion necessary for soliton formation, and a semiconductor saturable absorber mirror (SESAM; BATOP opto-electronics SAM 332-IVb.18). After the second pass through the grating pair, the QWP converts the polarization to horizontal, so the pulse passes through PBS III and the isolator to begin the next round trip. The net dispersion is approximately -0.5 ps^2. The repetition rate of the cavity is 34 MHz. The fiber section of the cavity is around 2.2 m (single-pass), and the rest of the cavity is comprised of free space components.

Without any pulse division (but with circularly polarized pulses in the fiber), the cavity produces soliton pulses with 0.35 nJ of energy and 1.4 ps duration, as shown in Figure 3.3(a) and (b). Efforts to increase the pulse energy further result in multiple-pulsing.

To demonstrate the DPL concept, the longest dividing crystal of length 57.6 mm is added to the cavity. The results are summarized in Fig. 3.3(c-e). By increasing the pump power, the single pulse energy of the output pulse can reach 0.7 nJ with the same 1.4 ps duration, which corresponds to each divided pulse having the same 0.35 nJ pulse energy in fiber. Fig. 3.3(d) shows the intensity autocorrelation of the recombined output pulse, and Fig. 3.3(e) shows the intensity autocorrelation of the divided pulses, obtained from leakage from a cavity mirror. The autocorrelation of the divided pulse clearly corresponds to that of two pulses of equal intensity, and the 50 ps spacing corresponds to the delay induced by the birefringent crystal. Along with the autocorrelation showing the recombined pulse at the output, this confirms that the pulse division is operating as expected. The autocorrelation of the recombined pulse shows that any residual energy in the divided-pulse has been

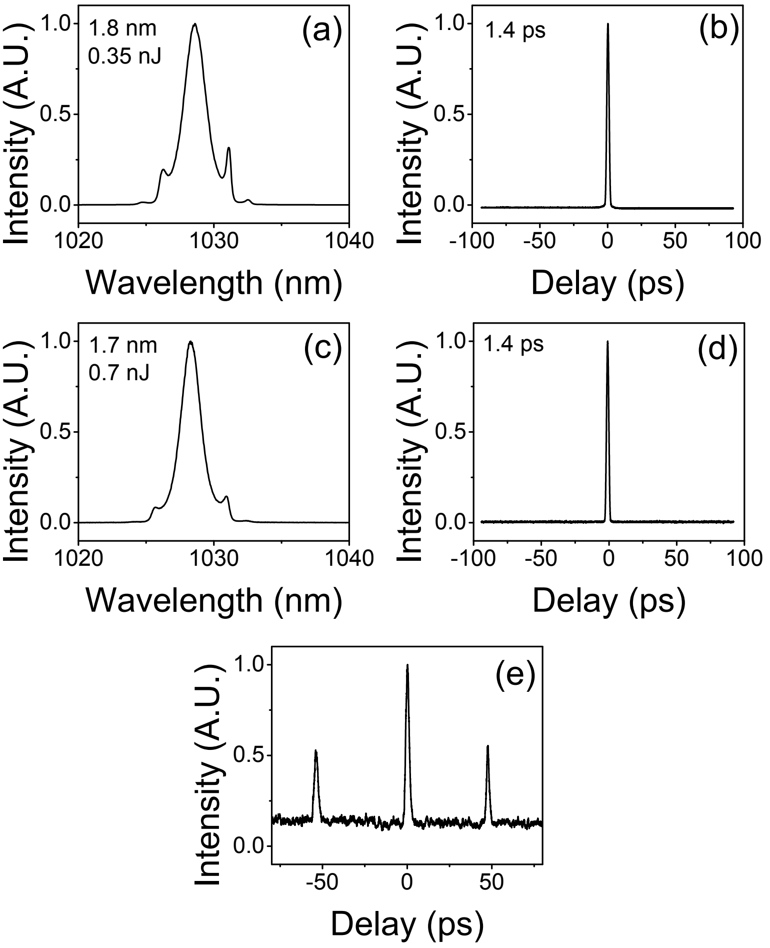

Figure 3.3: Experimental results with no pulse division: (a) spectrum; (b) autocorrelation of output pulse; and experimental results with 1 dividing element in the laser cavity: (c) spectrum; (d) autocorrelation of recombined output pulse; and (e) autocorrelation of divided pulse.

suppressed to below the dynamic range of the autocorrelator, which is around 25 dB.

The achievable single-pulse energy of the recombined pulse doubles with each additional crystal. The data for 2, 3, and 4 dividing crystals are presented in Fig. 3.4. With 4 dividing crystals in the cavity, we have achieved around 16 times scaling of the pulse energy, reaching over 6 nJ of pulse energy (over 200 mW of average power) from the soliton laser, as shown in Fig. 3.4(e). The spectrum in Fig.

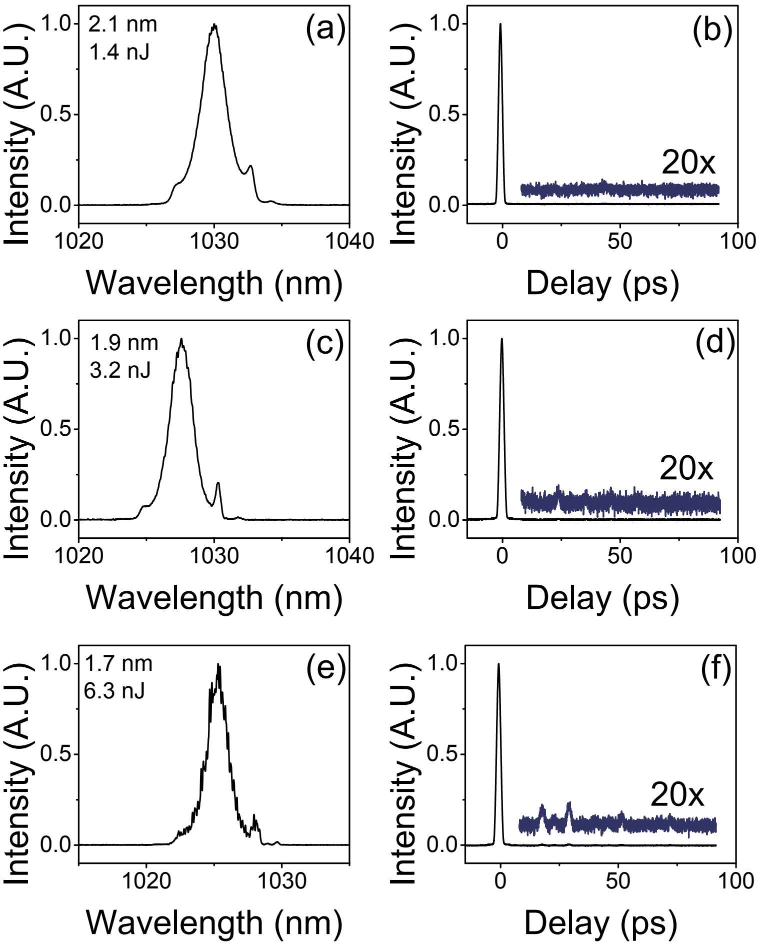

Figure 3.4: Experimental results: with 2 dividing crystals (a) spectrum; (b) autocorrelation of recombined pulse; with 3 dividing crystals (c) spectrum; (d) autocorrelation of recombined pulse; with 4 dividing crystals (e) spectrum; (f) autocorrelation of recombined pulse. The autocorrelation is multiplied by a factor of 20 and displaced vertically (blue traces) to highlight the slight imperfections in the recombination. The change in center wavelength is caused by variation in the cavity alignment.

3.4(e) starts to exhibit fringes from imperfect recombination of the divided pulses, but the autocorrelation in Fig. 3.4(f) shows that the corresponding secondary pulses have less than 1% of the energy of the main pulse. As shown in Fig. 3.5(a) and (b), the output pulses are chirped to about twice the transform limit, and can be dechirped to the transform limit. The radio-frequency spectrum near the fundamental repetition rate exhibits an instrument-limited contrast of over 70 dB, as shown in Fig. 3.5(c). Additionally, the mode is self-starting and stable over the course of a day, which is the longest time period tested. Although it is not the main point of this work, an attractive feature of this implementation is that operation is impervious to thermal and mechanical perturbations of the fiber owing to the Faraday rotator.

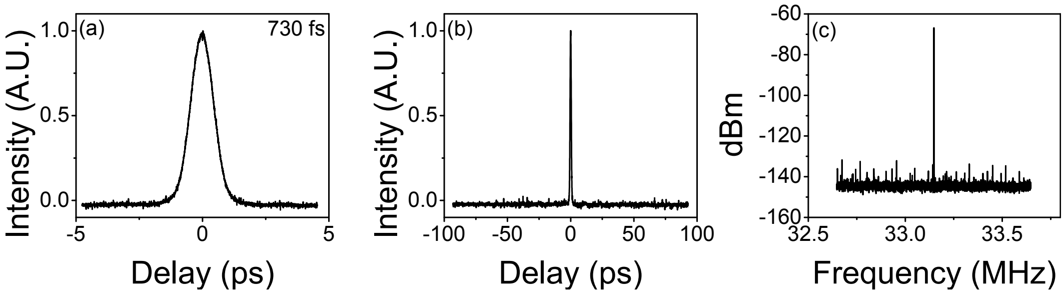

Figure 3.5: (a) Short-range and (b) long-range autocorrelations of the de-chirped pulses with 4 dividing crystals in the cavity. (c) RF spectrum of the fundamental repetition rate with 4 dividing crystals in the cavity. The RF spectrum is recorded with a Signal Hound Analyzer with a 200 Hz resolution bandwidth.

Two tests are performed to verify the peak power of the output pulse from this laser. First, 1.8 nJ of pulse energy from the 4-crystal cavity is launched into 2 m of single mode fiber to broaden under the influence of self-phase modulation, and the output spectrum is measured. In Fig. 3.6(a), the measured bandwidth is compared to a simulation of a hyperbolic secant with the expected peak power in the same length of fiber, showing that the spectral broadening is in reasonable agreement. In Fig. 3.6(b), the autocorrelation is measured using a second harmonic generation based autocorrelator (Femtochrome Research, Inc.) while crystals are removed from the cavity (and the pump power is correspondingly reduced). The signal is reduced by a factor of 4.18 as each crystal is removed, which is in good agreement with the expected reduction of 4 if the pulse energy is being reduced by a factor of 2. Both of these measurements indicate that the DPL is producing pulses with the expected peak power.

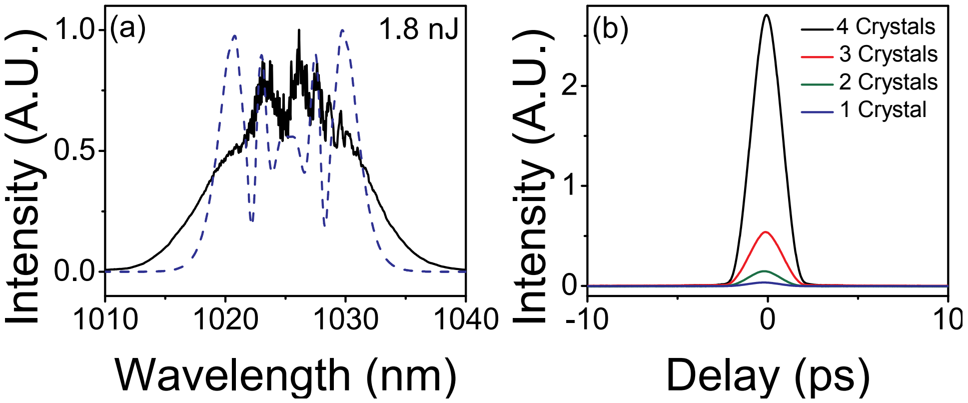

Figure 3.6: (a) Comparison of simulation (dotted line) and experiment (solid line) of a portion of the output pulse broadening in 2 m of single mode fiber. (b) Autocorrelation signal as a function of crystals in the cavity.

The results above demonstrate that coherent pulse division and recombination within the laser cavity can be used to avoid excessive nonlinearity and thereby scale the output energy from an ultrafast laser. This demonstration shows the utility of a DPL for scaling the energy of picosecond pulses from fiber lasers, which have typically been limited to sub-nanojoule energies. Thus, this technique may be advantageous for applications, such as coherent Raman imaging, that may require higher energy picosecond pulses. The DPL can also be used to create controllable pulse bursts, which are called for in some applications. The number of pulses is determined by the number of dividing elements, and a burst of equal amplitude pulses can be obtained by taking the output before recombination. More generally, the pulse burst can be tailored by tuning the dividing elements. An example of this with 2 dividing crystals (4 pulses) is shown in Figure 3.7.

Of course, the use of bulk crystals for pulse division and recombination does sacrifice some of the benefits of fiber construction. Thus, the DPL approach might be most-attractive in fiber-based lasers that already contain bulk components. However, in the current set-up, the free-space alignment could be reduced to a point-to-point alignment through the crystal stack by replacing the other bulk

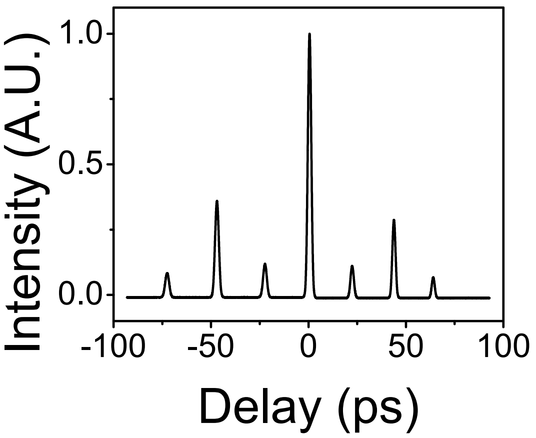

Figure 3.7: Autocorrelation of a pulse burst with two dividing crystals in the cavity. The crystals have been misaligned to yield pulses with unequal amplitudes.

components with their fiber-format equivalents, such as fiber Bragg gratings for the anomalous dispersion, fiber-coupled SESAMs and Faraday rotators, and fiber polarization controllers. As mentioned above, the implementation shown here is naturally compatible with environmental stability of the fiber segment in the laser.

3.3 Divided-pulse dispersion managed soliton laser

DPLs may offer advantages for other lasers and pulse evolutions, such as in dispersion managed soliton, dissipative soliton, and self-similar lasers, although the presence of spectral breathing in these other pulse evolutions may influence the pulse division and recombination. Experimental results on divided-pulse nonlinear compression [11] indicate that the pulse division and recombination works in the presence of spectral breathing, with fringes visible on the edges of the spectrum around 10 dB below the peak. These result from imperfect recombination of the pulse arising from the wavelength-dependent index of refraction of the dividing crystals inducing a different phase on the spectral components generated between division and recombination. Reference [11] also shows that this effect can be reduced by using beam splitters for the pulse division, although this comes at the cost of a less compact division and recombination stage.

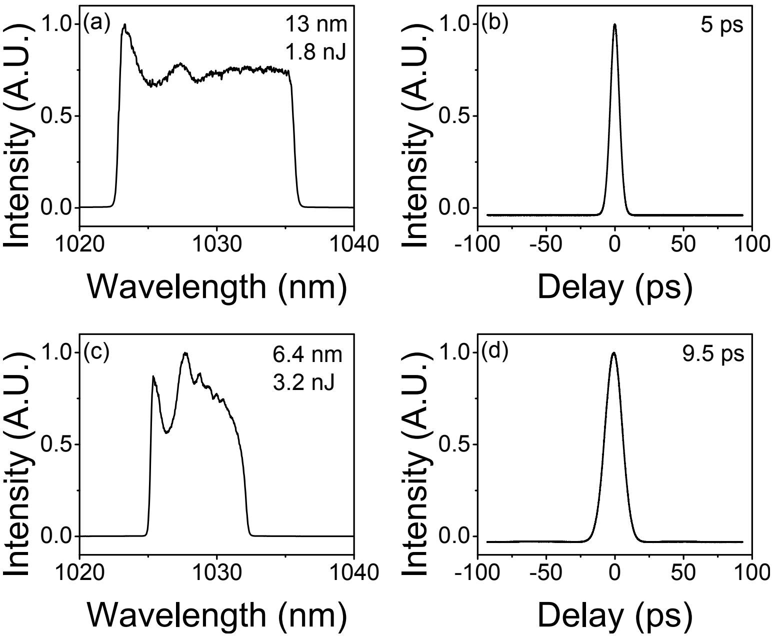

Figure 3.8: Experimental results of divided pulse dispersion managed soliton laser: (a) spectrum and (b) autocorrelation with no pulse division; and (c) spectrum and (d) autocorrelation with 1 dividing crystal.

As an initial test, a divided-pulse dispersion managed soliton laser is constructed. The cavity design is the same as in Fig. 3.2, with the grating separation reduced to give a net dispersion of around 26,000 fs^2. As shown in Fig. 3.8, the laser yields a 1.8 nJ pulse with a 13 nm spectral bandwidth with no dividing crystals in the cavity. When the 57.6 mm crystal is added, the pulse energy increases to 3.2 nJ, but the spectral bandwidth decreases to 6.4 nm. This can be understood by noting that the dispersion of this crystal is approximately 12,000 fs^2, single pass, so its inclusion nearly doubles the cavity's net dispersion. Thus, the grating pair should be adjusted to maintain the same net dispersion as crystals are added, but the pulse evolution may still be influenced by the resulting change to the dispersion map. This issue could also be avoided by using beam splitters for the pulse division and recombination to avoid changing the dispersion map.

These initial results show that the laser mode-locks with pulse division in a mapped cavity with spectral breathing, which is important for the extension of DPLs to the other pulse evolutions. However, the bandwidths of the generated spectra are narrower than expected for a dispersion managed soliton laser [14]. Further study of this laser is needed to determine which aspect of the cavity design is limiting the performance.

3.4 Divided-pulse dissipative soliton laser

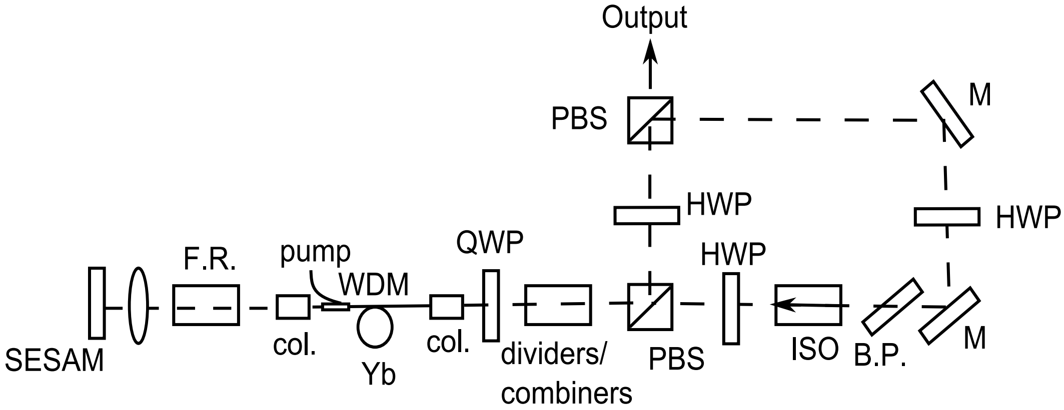

Figure 3.9: Divided-pulse dissipative soliton fiber laser. M: mirror; F.R.: Faraday rotator; col.: collimator; WDM: wavelength division multiplexer; QWP: quarter-wave plate; HWP: half-wave plate; PBS: polarizing beam splitter; ISO: isolator; SESAM: semiconductor saturable absorber mirror; B.P.: birefringent plate.

Initial experiments are also performed with a divided-pulse dissipative soliton laser. Without the need to provide anomalous dispersion, the cavity is reduced to a sigma-cavity with the same SESAM serving as the retro-reflector in the linear arm, as shown in Fig. 3.9. Mode-locked spectra for this cavity with 0 and 1 dividing crystals in the cavity are shown in Fig. 3.10. The performance of this cavity is fairly limited, although that is partly due to the SESAM, which tends to limit the pulse duration and energy compared to dissipative solitons mode-locked with nonlinear polarization evolution (NPE) [15]. Also, the greater variability in mode-locked states of the dissipative soliton laser makes it less straightforward to extract the effects of pulse division on the laser performance. Still, the output pulse energy does increase with the addition of the dividing crystal to the cavity, with the 5.1 nJ pulse energy being limited by the available pump power.

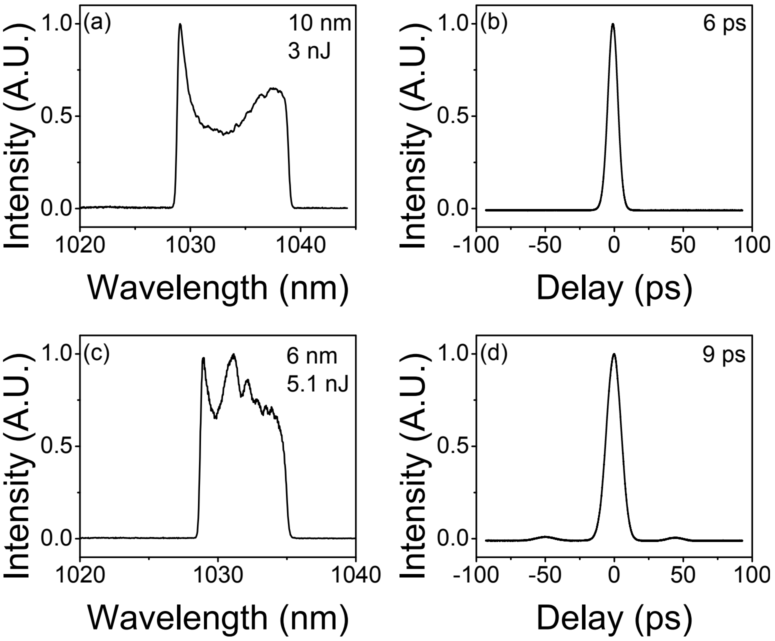

Figure 3.10: Experimental results of divided pulse dissipative soliton laser: (a) spectrum and (b) autocorrelation with no pulse division; and (c) spectrum and (d) autocorrelation with 1 dividing crystal.

3.5 Conclusion

DPLs have been demonstrated for a soliton laser, and preliminary results for divided-pulse dispersion managed solitons and dissipative solitons are also presented. Although these latter two lasers are far from optimized, they do indicate that pulse division is compatible with these pulse evolutions. Likely, superior performance can be achieved from these cavities by replacing the SESAM with a saturable absorber with greater energy handling capabilities and with a larger modulation depth. This could be possible by using NPE in a restricted section of the cavity, or by implementing a nonlinear optical loop mirror.

The DPL technique is also compatible with other energy-scaling techniques such as the use of large-core fiber. The technique should also be applicable to other gain media. Control of the pulse evolution is generally limited in solid-state systems, so divided-pulse lasers may be particularly interesting, although polarization sensitivity of the gain media will have to be addressed.

In conclusion, we have proposed and demonstrated the use of coherent pulse division and recombination within a laser cavity. The DPL concept has enabled 16 times scaling of the pulse energy from a fiber soliton laser. This technique should be applicable to other laser systems and may enable record-breaking oscillator performance.

BIBLIOGRAPHY

[1] E. S. Lamb, L. G. Wright, and F. W. Wise, Opt. Lett. **39**, 2775 (2014).

[2] K. Tamura, E. P. Ippen, H. A. Haus, and L. E. Nelson, Opt. Lett. **18**, 1080 (1993).

[3] F. O. Ilday, J. R. Buckley, W. G. Clark, and F. W. Wise, Phys. Rev. Lett. **92**, 213902 (2004).

[4] B. Oktem, C. Ulgudur, and F. O. Ilday, Nat Photon **4**, 307 (2010).

[5] W. H. Renninger, A. Chong, and F. W. Wise, Phys. Rev. A **82**, 021805 (2010).

[6] A. Chong, J. Buckley, W. Renninger, and F. Wise, Opt. Express **14**, 10095 (2006).

[7] A. Galvanauskas, Selected Topics in Quantum Electronics, IEEE Journal of **7**, 504 (2001).

[8] S. Zhou, F. W. Wise, and D. G. Ouzounov, Opt. Lett. **32**, 871 (2007).

[9] L. J. Kong, L. M. Zhao, S. Lefrancois, D. G. Ouzounov, C. X. Yang, and F. W. Wise, Opt. Lett. **37**, 253 (2012).

[10] Y. Zaouter, F. Guichard, L. Daniault, M. Hanna, F. Morin, C. Hönninger, E. Mottay, F. Druon, and P. Georges, Opt. Lett. **38**, 106 (2013).

[11] A. Klenke, M. Kienel, T. Eidam, S. Hädrich, J. Limpert, and A. Tünnermann, Opt. Lett. **38**, 4593 (2013).

[12] M. Kienel, A. Klenke, T. Eidam, M. Baumgartl, C. Jauregui, J. Limpert, and A. Tünnermann, Opt. Express **21**, 29031 (2013).

[13] D. N. Schimpf, T. Eidam, E. Seise, S. Hädrich, J. Limpert, and A. Tünnermann, Opt. Express **17**, 18774 (2009).

[14] H. Lim, F. O. Ilday, and F. W. Wise, Opt. Lett. **28**, 660 (2003).

[15] A. Chong, W. H. Renninger, and F. W. Wise, Opt. Lett. **33**, 1071 (2008).

CHAPTER 4

RELATIVE INTENSITY NOISE OF FIBER LASERS

4.1 Introduction

Little systematic study has been done to assess the relative intensity noise (RIN) performance of fiber lasers. An interesting outstanding question is whether the pulse evolution in the laser cavity influences the noise properties of the output. Li and coworkers demonstrate that the presence of a narrowband spectral filter in the amplifier similariton lasers results in dispersion-independent frequency noise [1], which is in contrast to prior work on dispersion managed soliton lasers [2]. Qin et al. also report that the presence of a narrow bandwidth spectral filter results in intensity noise reduction over the frequency range 100 kHz to 5 MHz [3], indicating that pulse evolutions that rely on narrow bandwidth filters may offer superior noise performance overall. Budunoglu and coworkers present a comparison of RIN for soliton, stretched-pulse, passive similariton, and dissipative soliton lasers in the frequency range covering 2.9 Hz to 200 kHz and conclude the cavity losses dominate the RIN, not differences in the pulse evolution [4]. However, effects such as environmental noise, relaxation oscillations, and pump to signal noise transfer are known to have a grater effect on the laser noise at lower frequencies [5, 6, 7]. Therefore, studying laser RIN in higher frequency ranges may prove better for determining the influence of the mode-locking regime on the laser's noise properties.

Applications such as stimulated Raman scattering (SRS) microscopy require sources of pulses with near shot-noise limited intensity noise and a few nanojoules of pulse energy [8]. Despite the advantages of fiber lasers in terms of cost, complexity, and reduced alignment sensitivity, solid state systems continue to dominate the field, which is in part due to their superior RIN. To date, no fiber source has achieved the low-noise operation needed to perform SRS microscopy without additional noise cancellation [9], which raises questions about the ultimately achievable noise performance from fiber lasers. Specifically, most SRS imaging experiments are performed using lock-in detection with a modulation frequency around 10-20 MHz [8], providing motivation to understand laser RIN in this frequency range.

In this chapter, we study relative intensity noise of dissipative soliton [10] and amplifier similariton [11] fiber lasers numerically and experimentally. These lasers are of interest to applications as they are capable of producing the highest energy and shortest pulses from fiber lasers. They also exhibit fundamentally different pulse evolutions. The pulse in a dissipative soliton laser (also known as the all-normal dispersion, or ANDi, laser) is an average cavity solution stabilized by the filtering of a chirped pulse. In contrast, the pulses in an amplifier similariton cavity are stabilized by self-similar attraction to parabolic pulses in the gain segment and thus are determined by a local attractor [12]. Numerically, we present strong evidence that the RIN in the 10-20 MHz range is fixed by the local attractor in the amplifier similariton lasers, whereas the RIN exhibits more variation in the case of the average cavity dissipative soliton lasers. We show the corresponding experimental data, which is currently inconclusive.

4.2 Modeling

The dissipative soliton and amplifier similariton laser cavities are simulated using a split-step method [13]. The standard cavity consists of 3 m of passive single mode fiber preceding the gain fiber, 70 cm of Yb-doped gain fiber, and 1 m of passive fiber following the gain fiber. An ideal saturable absorber curve is assumed. For the dissipative soliton cavity, both 70% and 100% modulation depth absorbers are modeled; a 100% modulation depth is used for the amplifier similariton cavity. Gaussian spectral filters are applied in both cavities, with bandwidths ranging from 8-20 nm for the dissipative soliton and 2 or 4 nm for the amplifier similariton. The saturation energy of the gain fiber is varied from 0.3 nJ to 1.7 nJ to yield different converged pulse energies. The output coupling is 70% for both lasers, with an additional 30% loss also assumed to account for other experimental losses. Experimentally, the amplifier similariton lasers will have a larger loss due to the difference in filter implementation, but in simulation the losses are kept the same to better isolate the influence of the pulse evolution.

Quantum noise terms arising from gain and loss are introduced into the simulation as described by Paschotta [14, 15], with some approximations in place. The pump dynamics in the gain fiber are not considered. Instead, the fiber is modeled with a fixed 30 dB gain and the saturation energies given above. These approximations will limit the accuracy of the simulation at lower frequencies [15] but are not expected to have a large influence in the tens of megahertz frequency range of interest in this study. The noise from the gain is added as a lump sum at the end of the gain segment. Noise terms are also added for all of the cavity losses, including output coupling, the linear loss term, saturable absorption, and spectral filtering. The nonlinear losses are treated as linear losses with the same average value, and are assumed to apply evenly over all frequencies since including the frequency dependence of the spectral filtering was found to have little effect on the simulated noise curves.

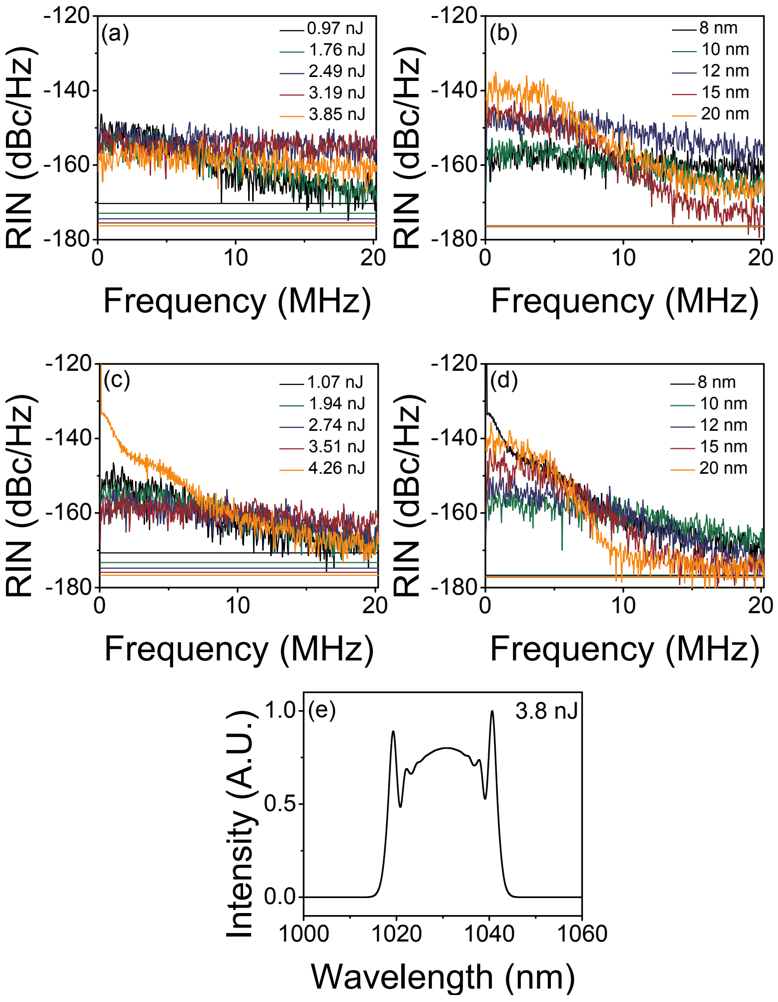

Figure 4.1: Simulated relative intensity noise (RIN) traces for dissipative soliton lasers for: (a) a fixed 8 nm filter bandwidth and varying converged pulse energy and (b) a fixed 4 nJ pulse energy and varying intracavity filter bandwidth with a 100% modulation depth saturable absorber. Simulated RIN traces for dissipative soliton lasers for: (c) a fixed 8 nm filter bandwidth and varying converged pulse energy and (d) a fixed 4.5 nJ pulse energy and varying intracavity filter bandwidth with a 70% modulation depth saturable absorber. The horizontal lines represent the shot noise level for the RIN trace of the same color. (e) Characteristic simulated spectrum.

The noise simulations are run for 1224 round trips and the output pulse energy is recorded for each round trip. The first 200 round trips are discarded to limit the following analysis to the steady-state behavior of the laser. The RIN traces are calculated as described in references [14, 15]. In summary, the power fluctuations are tabulated, a Hanning window function is applied to the data, and the resulting data are used to calculate the power spectral density and the RIN trace. For each simulated cavity, the noise simulation is completed 7 times, and the 7 traces are averaged.

Energy (nJ)	RMS RIN (x10^{-5})	Spectral BW/Filter BW
0.97	2.7	1.2
1.76	3.4	1.8
2.49	8.4	2.3
3.19	8.5	2.6
3.84	4.8	3.0

Table 4.1: RMS RIN for the 10-20 MHz frequency range for the simulations in Fig. 4.1(a) for the dissipative soliton laser with an 8 nm intra-cavity filter and the 100% modulation depth saturable absorber.

Filter BW (nm)	RMS RIN (x10^{-5})	Spectral BW/Filter BW
8	4.8	3.0
10	2.7	2.0
12	3.6	1.6
15	10.1	1.0
20	3.8	0.7

Table 4.2: RMS RIN for the 10-20 MHz frequency range for the simulations in Fig. 4.1(b) for the dissipative soliton laser with varying intra-cavity filter bandwidth and the 100% modulation depth saturable absorber.

The results for the dissipative soliton cavity are summarized in Figure 4.1 and in Tables 4.1 and 4.2. In Fig. 4.1, we note that the RIN traces vary with pulse energy, filter bandwidth, and saturable absorber modulation depth. It should also be noted that the spectral bandwidth of the output increases with pulse energy, so the filtering loss also increases, as quantified by showing the ratio of output spectral bandwidth to filter bandwidth in Table 4.1. The filtering loss decreases with increasing filter bandwidth as described in Table 4.2. Increasing RIN is somewhat correlated with increased filtering loss, indicating that the difference in cavity losses is one factor in the variation of the RIN, but not the only factor.

In general, the variation between high frequency RIN is greater with the 100% modulation depth absorber than for the 70% modulation depth absorber, which shows that the saturable absorber function may also be an important factor.

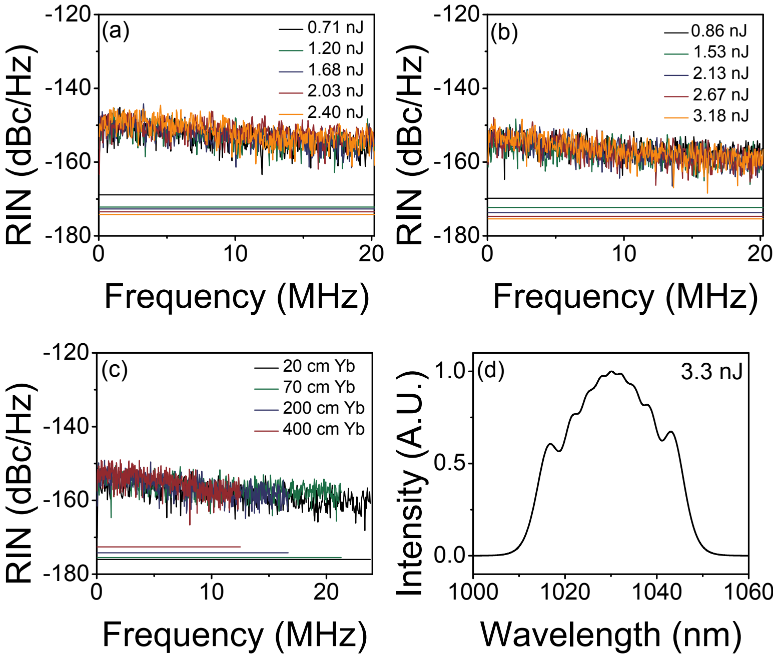

Figure 4.2: Simulated relative intensity noise (RIN) traces for amplifier similariton lasers for: (a) cavity with a 2 nm filter bandwidth and 70 cm of Yb gain; (b) cavity with a 4 nm filter bandwidth and 70 cm of Yb gain; and (c) cavity with a 4 nm filter bandwidth and varying lengths of Yb gain. The horizontal lines represent the shot noise level for the RIN trace of the same color. (d) Characteristic simulated spectrum.

Energy (nJ)	RMS RIN (x10^{-5})	Spectral BW/Filter BW
0.86	6.4	3.4
1.53	5.4	4.8
2.13	5.5	5.8
2.67	5.5	6.7
3.18	5.7	7.4

Table 4.3: RMS RIN for the 10-20 MHz frequency range for the simulations in Fig. 4.2(b) for the amplifier similariton laser with a 4 nm intra-cavity filter.

In contrast, the observed variation of RIN spectra with pulse energy is not replicated for the amplifier similariton simulations, shown in Fig. 4.2. The filtering losses again increase with increasing pulse energy, but the RIN remains constant.

The consistency of the RIN traces for a given filter bandwidth suggests that the local attraction to the parabolic pulse in the gain fiber is fixing the noise properties of the laser, making the RIN curves less sensitive to other cavity effects, such as loss. It is particularly interesting that the RIN of the amplifier similariton laser is higher than the best performance of the dissipative soliton laser, indicating that the presence of the local attractor makes the RIN more consistent but not necessarily quieter for a given cavity design. Table 4.3 shows the root-mean square (RMS) RIN for the cavity with the 4 nm filter (Fig. 4.2(b)), which confirms the much higher level of consistency versus converged pulse energy than is observed for the dissipative soliton laser. Fig. 4.2(c) shows the RIN traces for 4 different lengths of Yb gain fiber, since the gain per unit length is an important parameter in determining the asymptotic solution [16]. Little variation is observed, indicating the robustness of the attraction in this parameter range.

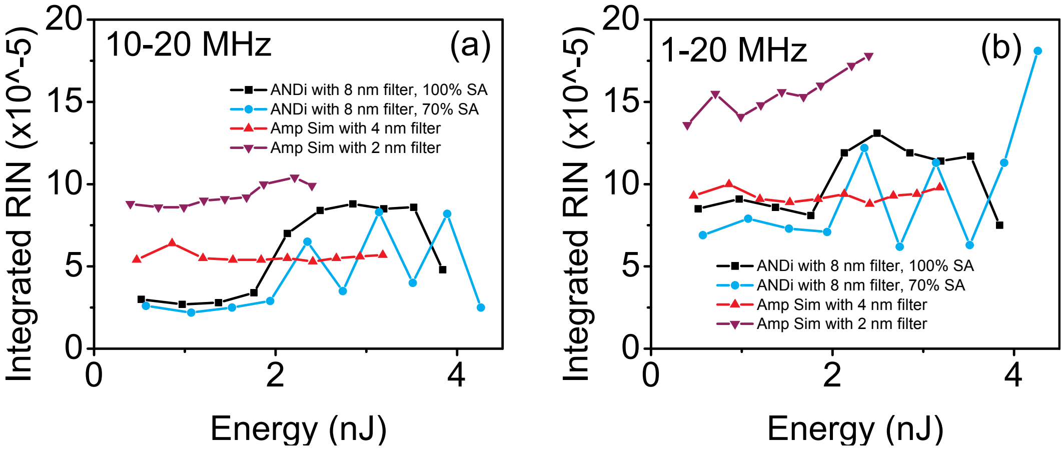

Figure 4.3: Integrated RIN for representative laser parameters over (a) 10-20 MHz and (b) 1-20 MHz.

Fig. 4.3 summarizes the integrated RIN for the various laser configurations under study over the 10-20 MHz and 1-20 MHz frequency ranges. It can be observed that the amplifier similariton is quieter with the 4 nm filter than with the 2 nm filter. This fits the hypothesis that the local attractor is strongly influencing the

RIN properties of the laser since the pulse evolution for the cavity with the 4 nm filter shows closer attraction to a parabola in the gain segment than in the cavity with the 2 nm filter. Fig. 4.3 also highlights the greater variability in RIN of the dissipative soliton lasers.

4.3 Experiments

The experimental cavity designs have been well documented in the literature [10, 17, 11]. In summary, both are constructed using 65 cm of core-pumped Yb-gain fiber (Yb-501, CorActive). The lasers are counter-pumped, with around 1.5 m of passive fiber before the gain and 2 m after the gain, yielding a repetition rate of 46 MHz. The only difference between the two cavities is the filter. The dissipative soliton laser uses a quartz plate to form filter bandwidths ranging from 8-20 nm, and the amplifier similariton uses a grating-based filter. In these experiments, a 300 lines/mm grating is used with a 45 degree angle of incidence placed 9 cm from an aspheric lens collimator with a 1 mm beam size to form an approximately 4 nm filter bandwidth.

RIN measurements are taken using an amplified silicon photodiode (Precision Applied Science PD1040 HRL-FC). The signal from the photodiode is low-pass filtered with a cut-off frequency of 22 MHz (Mini-Circuits BLP-21.4+) to eliminate the strong signal from the repetition rate of the laser. A bias-tee (Mini-Circuits ZFBT-4R2GW+) is used to separate the DC and AC signals; the DC signals are monitored on an oscilloscope and the AC signals are measured using a radio-frequency analyzer (Signal Hound-SA44B).

In the interest of reproducibility, data are recorded by mode-locking the laser at

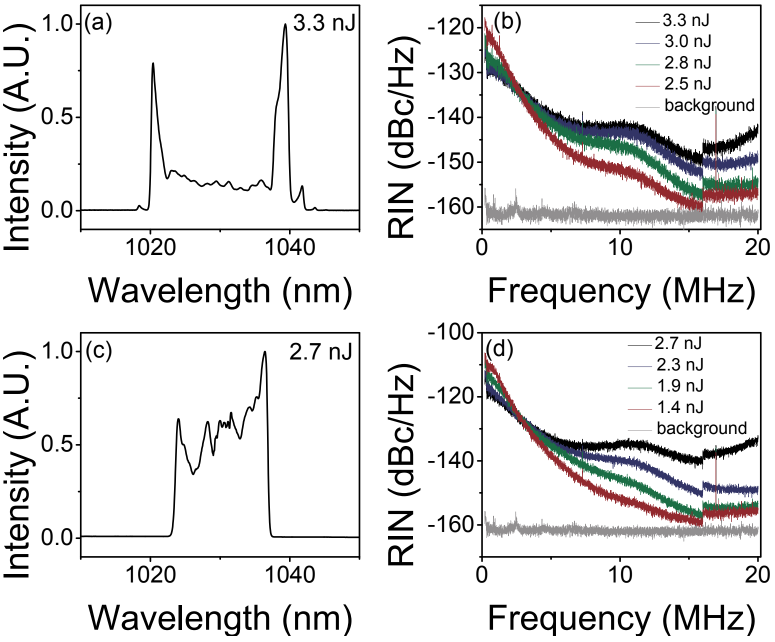

Figure 4.4: Relative intensity noise measurements for the dissipative soliton laser with the 8 nm filter. (a) Spectrum of high energy pulse and (b) RIN traces as the pump power is reduced. The output coupling is around 50%. (c) Spectrum of high energy pulse and (d) RIN traces as the pump power is reduced. The output coupling is around 70%. All RIN data are recorded at 150 mV with a 6.5 kHz resolution bandwidth.

Energy (nJ)	RMS RIN (x10^{-4})	Spectral BW/Filter BW
3.3	2.5	2.5
3.0	1.9	2.4
2.8	1.2	2.3
2.5	0.7	2.3

Table 4.4: RMS RIN for the 10-20 MHz frequency range for the experiments in Fig. 4.4(b) for the dissipative soliton laser with an 8 nm intra-cavity filter.

high pump power and then reducing the pump power. Two examples of a series of RIN spectra for the cavity with the 8 nm filter are shown in Fig. 4.4. The spectra corresponding to the highest pump power for each data set are shown in Figs. 4.4(a) and (c); the RIN decreases with pump power as seen in Figs. 4.4(b) and (d). The reduction in RIN at lower pulse energies is significantly more dramatic in experiment than in simulation (Fig. 4.1(a)) and the overall level of the RIN is worse, as quantified in Table 4.4. The trend of lower RIN with reduced output pulse energy (accomplished by lowering the pump power) is highly reproducible qualitatively. For the data shown in Fig. 4.4(b) and Table 4.4, the filtering loss is almost the same for all three traces. Since the RIN traces still show variation, this implies that other factors, such as the unknown experimental saturable absorber function, are important.

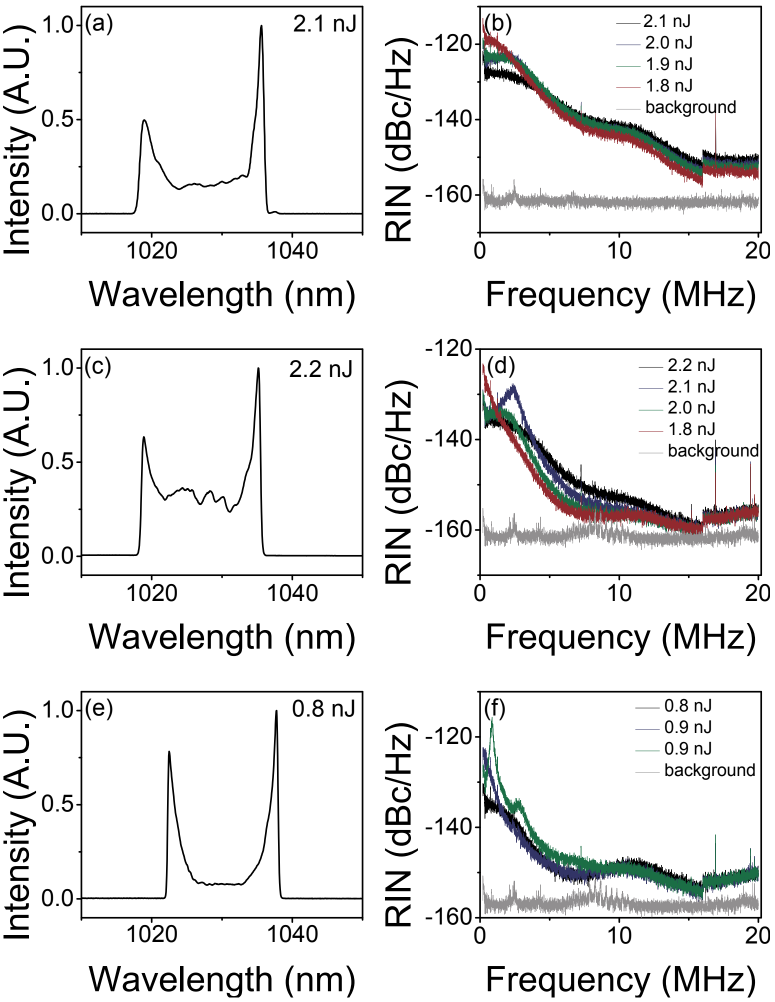

Figure 4.5: Relative intensity noise measurements for the dissipative soliton laser with varying filter bandwidth. (a) Spectrum of high energy pulse and (b) RIN traces as the pump power is reduced for the 10 nm filter with around 35% output coupling. (c) Spectrum of high energy pulse and (d) RIN traces as the pump power is reduced for the 12 nm filter with around 35% output coupling. (e) Spectrum of high energy pulse and (f) RIN traces as the pump power is reduced for the 15 nm filter with around 15% output coupling. All RIN data recorded at 150 mV with a 6.5 kHz resolution bandwidth.

Experimentally, the comparison of RIN is less straightforward as the filter bandwidth is changed since the cavity must be re-aligned and mode-locked for each filter. Since mode-locked states with similar pulse energy and output coupling are difficult to achieve for the different filters, rather than making a direct comparison of RIN versus filter bandwidth, Fig. 4.5 instead shows trends for three filter bandwidths as the pump power is decreased. Although not conclusive, these results indicate that quieter states may be more consistently achievable at broader filter bandwidths since many of the RIN traces are approaching the instrument-limited noise floor. Note that the proximity of the traces to the noise floor is likely masking differences in the RIN levels at the highest frequencies.

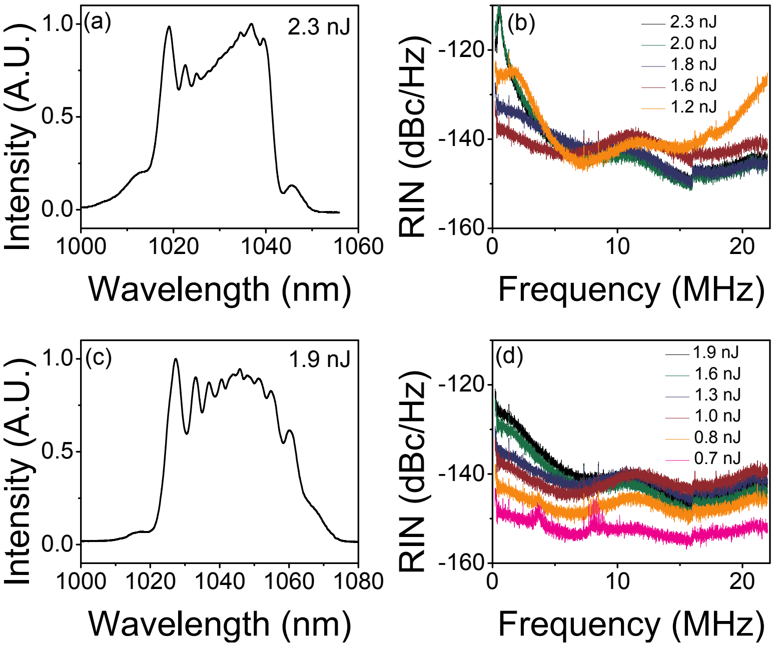

Figure 4.6: Relative intensity noise measurements for the amplifier similariton laser with a 4 nm filter. (a) Spectrum of high energy pulse and (b) RIN traces as the pump power is reduced. The estimated output coupling is around 40-55%. (c) Spectrum of high energy pulse and (d) RIN traces as the pump power is reduced. The estimated output coupling ranges from 45-80%. RIN data recorded at around 100 mV with a 6.5 kHz resolution bandwidth.

The RIN from an amplifier similariton laser is measured and shown in Fig. 4.6 using the same method as for the dissipative soliton. Although the RIN spectra

Energy (nJ)	RMS RIN (x10^{-4})	Spectral BW/Filter BW
2.3	2.3	6.2
2.0	2.1	5.6
1.8	2.4	5.0
1.6	3.8	4.6
1.2	4.8	4.9

Table 4.5: RMS RIN for the 10-20 MHz frequency range for the experiments in Fig. 4.6(b) for the amplifier similariton laser with a 4 nm intra-cavity filter.

do not overlay as exactly as the simulated spectra (Fig. 4.2), they do exhibit some of the same behavior. The first three entries in Table 4.5 show very little variation in the RMS RIN. The last two entries show a greater variation, but the estimated output coupling is between 45-47% for the first three and 54% and 40%, respectively, for the last two. This indicates that the laser is operating in different states for the last two recorded spectra, so an additional factor may explain the difference in RIN.

Some of the RIN spectra in Fig. 4.6 indicate that it is possible that the local attraction in the gain fiber is acting to constrain the RIN from the laser, but the influence of other experimental variables precludes a strong conclusion. The experimental RIN from the amplifier similariton does tend to be higher than for the dissipative soliton laser, which is also in agreement with simulation. This allows for the tentative conclusion that the RIN from the dissipative soliton laser exhibits more variability but may be the superior route to a quiet, high energy fiber laser.

As a counter-example, the amplifier similariton laser exhibits a different mode-locked state that does not match the trends seen in Fig. 4.6. For this state, the laser maintains the same converged pulse energy as the pump power is reduced and the amount of output coupling increases. This mode-locked state is reproducible. The RIN spectra for this laser state are presented in Fig. 4.7(b) and show that

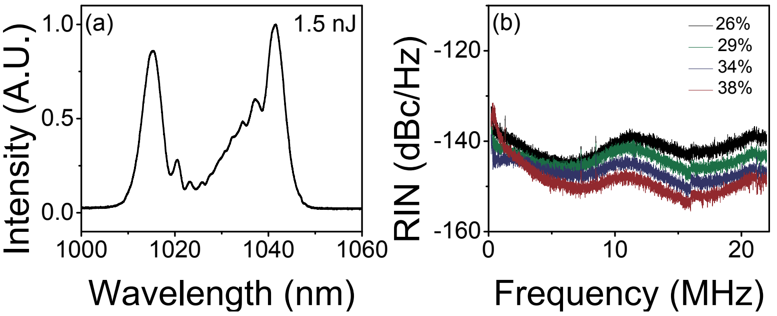

Figure 4.7: Relative intensity noise measurements for the amplifier similariton laser with a 4 nm filter and a 1.5 nJ pulse energy. (a) Spectrum of high energy pulse and (b) RIN traces as the pump power is reduced. The percentages in the legend are the estimated output couplings. RIN data recorded at around 100 mV with a 6.5 kHz resolution bandwidth.

in this case, the RIN systematically decreases for lower pulse energy and higher output coupling, which is not expected and indicates that even for the amplifier similariton, the RIN can depend on numerous experimental factors.

4.4 Conclusion

In conclusion, we numerically demonstrate characteristically different intensity noise behavior between the dissipative soliton and amplifier similariton lasers. The simulations show that the RIN from the amplifier similariton lasers tends to be more consistent but higher than the RIN for the dissipative soliton laser. Indications of these trends are observed experimentally, but not conclusively. If verifiable, these results have interesting implications for the role of nonlinear attractors in determining the noise of mode-locked lasers. Practically, we note that the high energy dissipative soliton lasers can also have low intensity noise, making them suitable candidates for applications such as stimulated Raman scattering microscopy that require near shot-noise limited performance at high frequencies.

BIBLIOGRAPHY

[1] P. Li, W. H. Renninger, Z. Zhao, Z. Zhang, and F. W. Wise, in *CLEO: 2013* (Optical Society of America, Washington, DC, 2013), p. CTu1I.6.

[2] L. Nugent-Glandorf, T. A. Johnson, Y. Kobayashi, and S. A. Diddams, Opt. Lett. **36**, 1578 (2011).

[3] P. Qin, Y. Song, H. Kim, J. Shin, D. Kwon, M. Hu, C. Wang, and J. Kim, Opt. Express **22**, 28276 (2014).

[4] I. L. Budunouglu, C. Ülgüdür, B. Oktem, and F. O. Ilday, Opt. Lett. **34**, 2516 (2009).

[5] R. P. Scott, T. D. Mulder, K. A. Baker, and B. H. Kolner, Opt. Express **15**, 9090 (2007).

[6] T. D. Mulder, R. P. Scott, and B. H. Kolner, Opt. Express **16**, 14186 (2008).

[7] R. P. Scott, C. Langrock, and B. Kolner, Selected Topics in Quantum Electronics, IEEE Journal of **7**, 641 (2001).

[8] C. W. Freudiger, W. Min, B. G. Saar, S. Lu, G. R. Holtom, C. He, J. C. Tsai, J. X. Kang, and X. S. Xie, Science **322**, 1857 (2008).

[9] C. W. Freudiger, W. Yang, G. R. Holtom, N. Peyghambarian, X. S. Xie, and K. Q. Kieu, Nat Photon **8**, 153 (2014).

[10] A. Chong, J. Buckley, W. Renninger, and F. Wise, Opt. Express **14**, 10095 (2006).

[11] W. H. Renninger, A. Chong, and F. W. Wise, Phys. Rev. A **82**, 021805 (2010).

[12] W. H. Renninger, A. Chong, and F. W. Wise, Selected Topics in Quantum Electronics, IEEE Journal of **18**, 389 (2012).

[13] G. P. Agrawal, *Nonlinear Fiber Optics* (Academic press, Burlington, MA, 2007).

[14] R. Paschotta, Applied Physics B **79**, 153 (2004).

[15] R. Paschotta, Applied Physics B **79**, 163 (2004).

[16] M. E. Fermann, V. I. Kruglov, B. C. Thomsen, J. M. Dudley, and J. D. Harvey, Phys. Rev. Lett. **84**, 6010 (2000).

[17] A. Chong, W. H. Renninger, and F. W. Wise, J. Opt. Soc. Am. B **25**, 140 (2008).

CHAPTER 5

OPTICAL PARAMETRIC OSCILLATOR FOR COHERENT RAMAN SCATTERING MICROSCOPY[1]

5.1 Introduction

Coherent anti-Stokes Raman scattering (CARS) microscopy offers label-free, three-dimensional optical sectioning of biological tissue by utilizing intrinsic molecular vibrations [3]. The source needed for this technique must supply two narrow-bandwidth, synchronized picosecond pulse trains with a frequency difference tunable to the relevant Raman shift. Transform limited, few-picosecond pulses are ideal for achieving the highest peak power while filling the Raman vibrational lineshape. The majority of CARS imaging experiments are conducted using a frequency doubled Nd-YVO_4 laser to synchronously pump a bulk optical parametric oscillator (OPO) [4]. The complexity and large footprint of such a source hinders the widespread use of CARS microscopy.

Sources that exploit the compact and alignment-free nature of fiber could make CARS more accessible. Fiber-based sources include a frequency doubled fiber laser used to pump a bulk OPO [5, 6] and a two-color source based on frequency-shifting a picosecond Er-doped fiber laser to perform second harmonic generation (SHG) [7]. Another uses the output from an Er-doped fiber laser to generate the two colors through SHG and filtering a supercontinuum generated from highly nonlinear fiber [8]. A similar scheme was adapted to be used with Tm-doped fiber amplifiers [9].

Other fiber-based sources use parametric generation. An optical parametric

---

[1] Much of the work presented in this chapter was published in Optics Letters [1] and the Proceedings of the SPIE [2].

amplifier (OPA) was used to provide femtosecond and picosecond pulses for coherent Raman microscopy [10], but its output is too low for video-rate imaging. Other OPAs use normal dispersion four-wave mixing (FWM) in photonic crystal fiber (PCF) to achieve large frequency shifts with narrowband pulses. An all-fiber OPA was used to perform CARS imaging, but the longer pulse durations yield much lower peak powers than are available from solid state sources [11]. Additionally, FWM tends to create noisy signal pulses [12]. This problem is alleviated in the fiber OPAs presented in [13, 14] through the use of continuous-wave (CW) seeding. The source demonstrated in [13] is the first fiber source to provide comparable pulse parameters and energies to the solid state source [4]. OPOs that accomplish frequency conversion through FWM in PCF have been studied as well and are summarized in [15]. One designed for multimodal CARS imaging uses a femtosecond seed laser [16], resulting in low pulse energy (0.1-0.5 nJ) and low spectral resolution and efficiency.

Here we present a synchronously-pumped fiber OPO based on the normal dispersion FWM process. The OPO achieves similar pulse parameters (2-4 ps duration and 3-4 nJ energy) to the OPA of Ref. [13], but with substantial performance and practical benefits over the OPA. For one, the self-consistent nature of the oscillator leads to significant reduction of the relative intensity noise (RIN) on the output pulse train. For another, the OPO reaches 13-20% conversion efficiency to the signal wavelength, as compared to only 10% in the OPA. As a practical advantage, the OPO eliminates the CW seed laser used in [13, 14]. The capabilities of this system are illustrated by its use in CARS imaging of mouse tissues. Additionally, work to create an all-fiber version of this OPO to fully take advantage of the alignment-free nature of fiber sources is presented.

5.2 Modeling

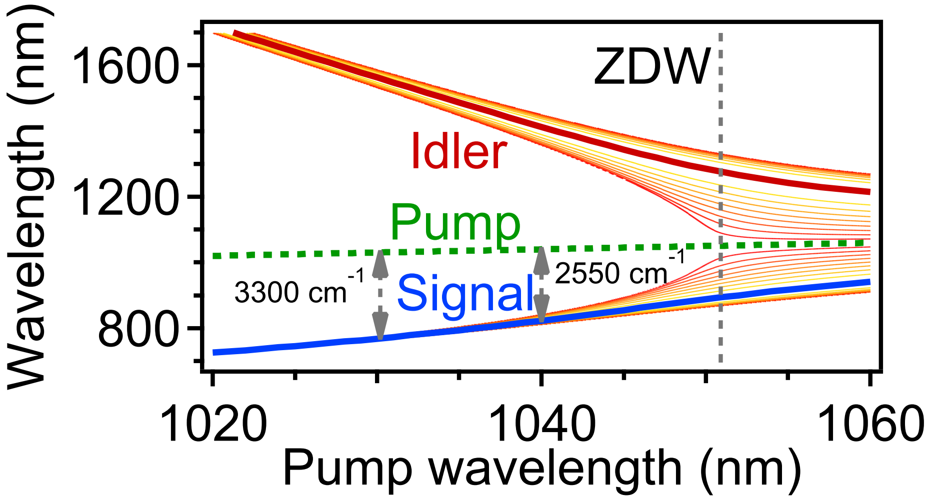

Figure 5.1: Phase matching diagram for photonic crystal fiber used in the experiments presented in this chapter. The fiber is provided by the University of Bath. ZDW: zero-dispersion wavelength. Figure is reprinted from [13], with permission.

Numerical simulations were used to guide the design of the OPO. The OPO is simulated with a generalized nonlinear Schrodinger equation that includes higher-order dispersion, spontaneous and stimulated Raman scattering, self-steepening, and input shot noise [17, 18]. Each round trip, shot noise and pump pulses at 1035 nm, with 7.5 ps duration and 1.95 kW peak power, are injected into 31 cm of endlessly single-mode PCF with a zero dispersion wavelength of 1051 nm. The dispersion coefficients at this pump wavelength are 1.59 fs^2/mm, 59.4 fs^3/mm, -69.3 fs^4/mm, 136 fs^5/mm, and -182 fs^6/mm, and the nonlinear parameter $\gamma =$ 9.6 (W·km)$^{-1}$. The phase-matching diagram for this fiber is shown in Fig. 5.1. We will refer to the short-wavelength photon as the signal and the long-wavelength photon as the idler. A 1300 nm long-pass filter is used to isolate the idler field to provide feedback for the cavity, with a 5% feedback ratio chosen to account for coupling and other losses. A delay is applied to the idler pulse to synchronize the idler and pump pulses. Under these conditions, the fluctuations on the signal and idler fields prohibit stable operation of the OPO (Figure 5.2(a)).

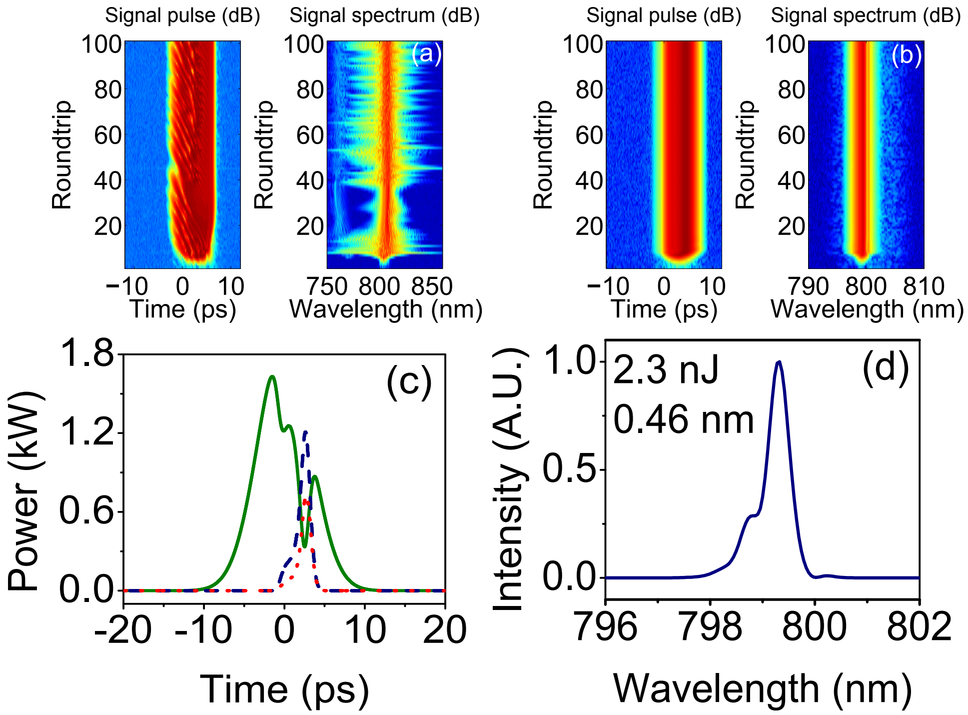

Figure 5.2: Results of simulations. (a) Signal pulse and spectrum without filter. (b) Signal pulse and spectrum with filter. (c) Filtered FWM: pump (solid curve), signal (dashed curve), and idler (dotted curve) pulses. (d) Signal spectrum. The input pulse is centered at 1035 nm with 7.5 ps duration and 1.95 kW peak power. Idler feedback is centered at 1468 nm with a 2 nm Gaussian filter.

We propose that filtering the field fed back into the PCF will result in stable, narrow-band operation. Simulations indicate that stable signal pulses are generated for filter bandwidths around 2-3 nm. Figure 5.2(b) shows the resulting signal with the use of a 2 nm Gaussian filter. The filter effectively stabilizes the field that is fed back, which in turn stabilizes the signal and idler in the oscillator. Nearly transform-limited 1.4 ps pulses with 2.3 nJ energy (Figures 5.2(c) and 5.2(d)) are generated at the signal frequency under these conditions. Thus, the narrow filter is a critical element of the design.

5.3 Optical parametric oscillator experiment

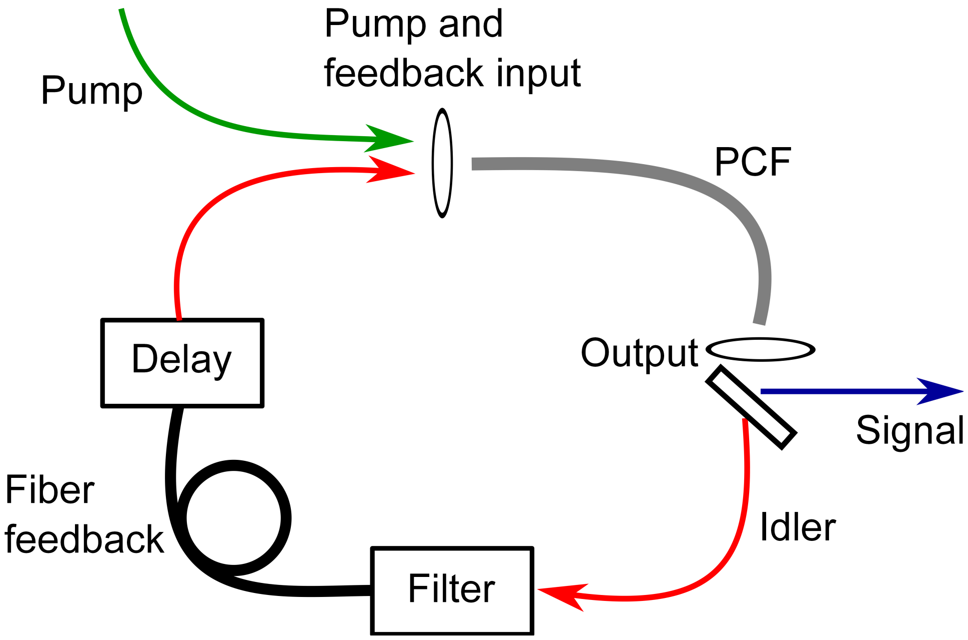

Figure 5.3: Schematic experimental set-up.

The experimental schematic is depicted in Fig. 5.3, and the literal experimental implementation is shown in Fig. 5.4. An Yb-doped fiber laser (a modified PicoFYb from Toptica Photonics), tunable from 1031 to 1038 nm, is used to seed a divided-pulse amplifier (DPA) constructed with 10 μm core fiber [19]. The output of the amplifier consists of 6.5-9 ps pulses with up to 2.5 W of average power at a repetition rate of 46 MHz. These pulses are coupled into a PCF with dispersion parameters matching those of the simulation and converted into signal and idler pulses. The signal light is coupled out of the OPO with a dichroic mirror, and a Gaussian filter with 2.7 nm bandwidth is created by a diffraction grating and fiber collimator, with the bandwidth chosen based on available gratings. Around 3.7 m of step-index fiber (Corning SMF28e+) forms the feedback loop, and a fiber coupled delay line with up to 80 ps of delay allows synchronization. The feedback ratio is estimated to be around 2%. An half-wave plate matches the

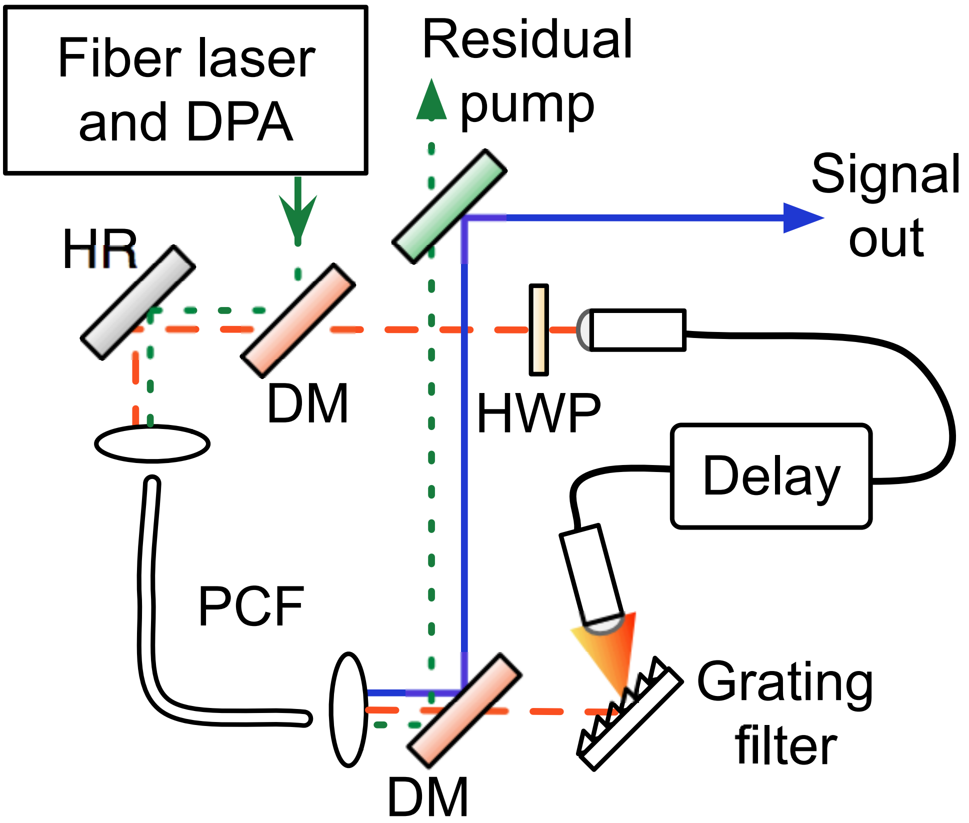

Figure 5.4: Experimental implementation of fiber optical parametric oscillator. The red lines representing the idler frequency and the fiber sections form the OPO cavity. DPA: divided-pulse amplifier; DM: dichroic mirror; HR: highly reflective mirror; PCF: photonic crystal fiber; HWP: half-wave plate.

polarization of the field that is fed back to that of the pump. Around 300 mW of the amplifier output is picked off before the OPO for combination with the signal at the microscope.

Experimental results obtained with 31 cm of PCF are shown in Figure 5.5. Pump pulses with 0.2 nm bandwidth and 8.7 ps duration are used (Figures 5.5(a) and 5.5(b)). With 850 mW (22 nJ) coupled into the PCF, 140 mW (3 nJ) is generated at the signal wavelength of 801 nm with a bandwidth of 0.5 nm and a duration of 2.1 ps, in good agreement with simulations. Higher pump powers yield signal powers up to around 200 mW (4.3 nJ), with slightly longer pulses,

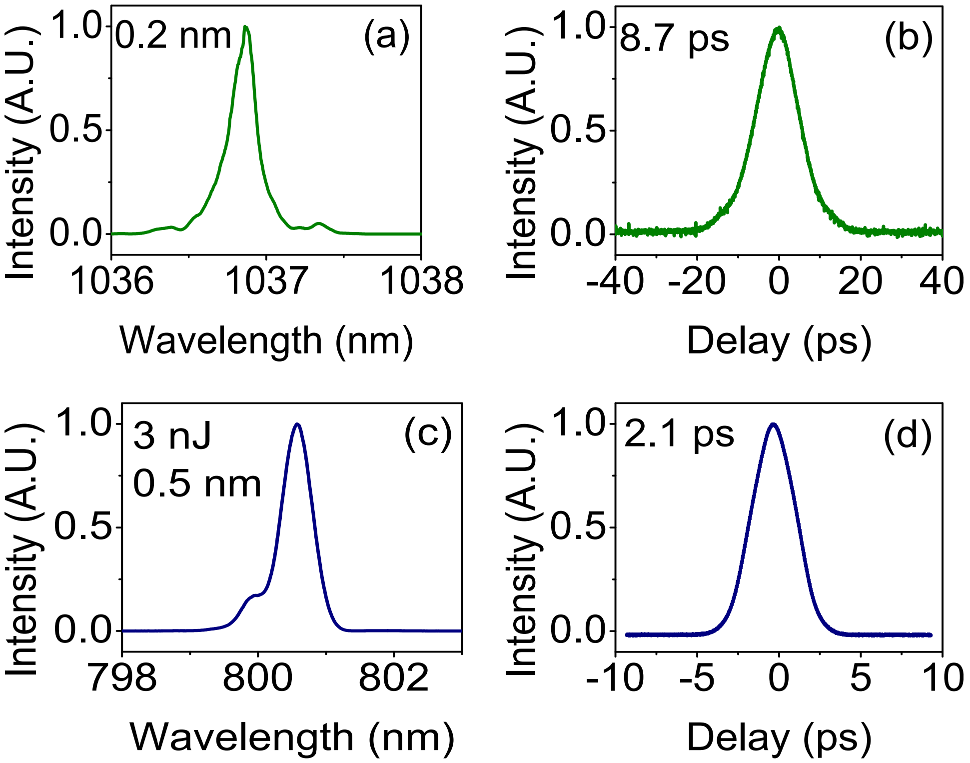

Figure 5.5: Experimental results: picked-off pump (a) spectrum and (b) autocorrelation. Signal (c) spectrum and (d) autocorrelation with a 2850 cm^{-1} frequency shift from the pump.

but the fluctuations increase; this will be discussed further below. Simulations indicate that longer PCFs generate higher pulse energies with more structured spectra due to coherent interactions between the pump and FWM fields as the process saturates. This is evidenced in the shoulder on the signal spectrum. The frequency difference between the pump and signal is 2850 cm^{-1}, which corresponds to the CH$_2$ stretching vibrational mode. The frequency shift can be tuned from 2740 to 3150 cm^{-1}, limited by the tuning range of the seed laser, with similar performance. The signal wavelength may be tuned over 2-3 nm by adjusting the center wavelength of the filter, and tuning over the broader range is accomplished by tuning the seed oscillator. Minimal realignment of the grating filter and delay line is required.

This OPO matches the pulse parameters of the solid-state device [4] and offers major performance advantages over other fiber-based sources. The peak signal power is twice that, and the average power three times that, of the fiber OPA reported in [14]. The peak power is 15 times that of the fiber source presented in [20], while the average power is 8 times higher.

After the imaging experiments described in the following section, an all-fiber version of this OPO is constructed and shown to have comparable performance. The bulk optics used to couple the light into and out of the PCF are replaced with 1040/1470 nm wavelength division multiplexers (Gooch and Housego). A reduced PCF length of around 20 cm is found to be optimal. The grating-based filter is replaced with a 2.4 nm fiber-coupled Fabry-Perot filter (OZ optics). This OPO cavity is alignment free after the pump light is coupled into the device and the pulse parameters are similar to those achieved with the bulk components.

5.4 Coherent anti-Stokes Raman scattering microscopy experiments

The signal pulses are combined with the picked-off pump pulses and directed to an Olympus FV300 microscope with an Olympus XL Plan N 25X water-immersion objective with an NA of 1.05. We use epi-detected CARS with an estimated 80 mW of light delivered to the sample. CARS images at the 2850 cm^{-1} vibrational shift are presented in Figure 5.6. Figs. 5.6(a) and (b) show white matter and the cortex in a mouse brain section, respectively. Fig. 5.6(c) shows the stratum corneum, and 5.6(d) shows a sebaceous gland around 36 μm deep in the mouse ear. The signal-to-noise ratio of the lipid droplets in the sebaceous gland images ranges

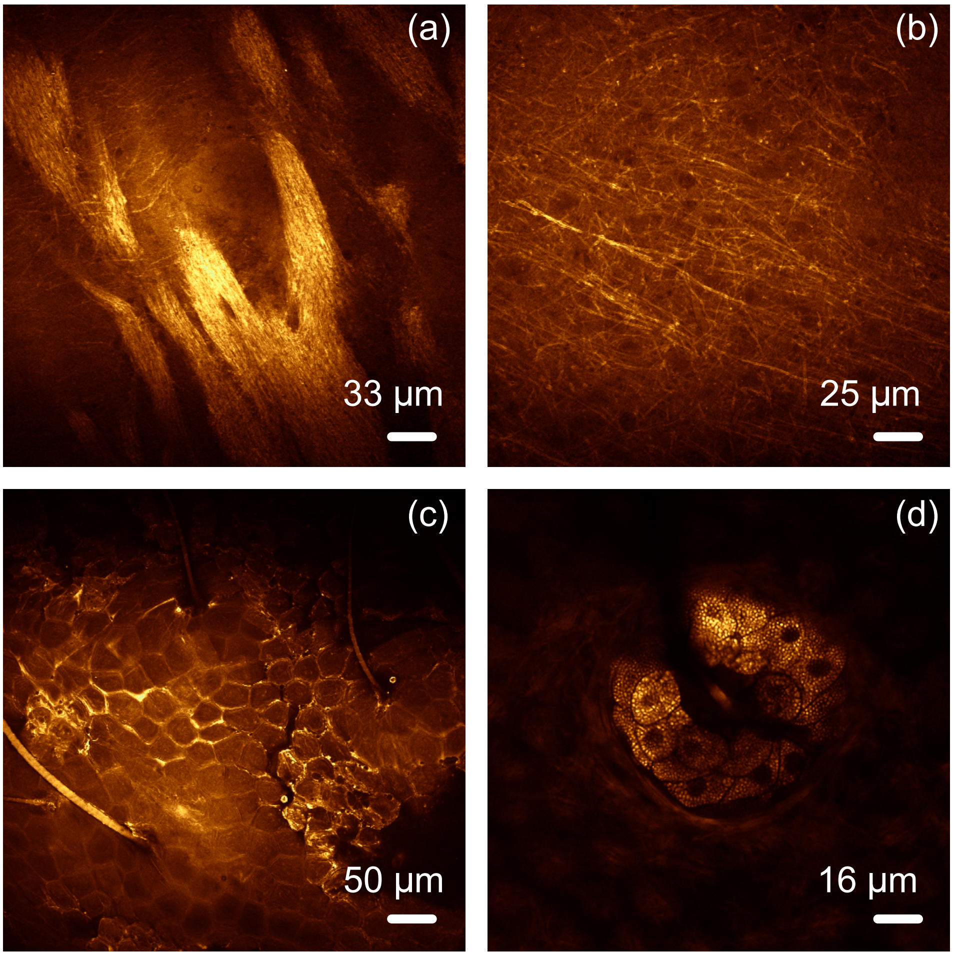

Figure 5.6: Epi-CARS images at 2850 cm^{-1}: (a) white matter in mouse brain section, (b) cortex in mouse brain section, (c) stratum corneum, and (d) sebaceous gland in mouse ear. 512 x 512 pixels at 2-4 μs per pixel, no averaging.

from 150 to 200, and the signal-to-noise ratio for the myelin sheathes is around 60. Images were taken at 2-4 μs per pixel without averaging. The OPO provides both improved image quality and imaging speed over the fiber source presented in [13]. Imaging was also performed at the 2930 cm^{-1} vibrational resonance (Fig. 5.7) as an initial demonstration of the tunability of the OPO.

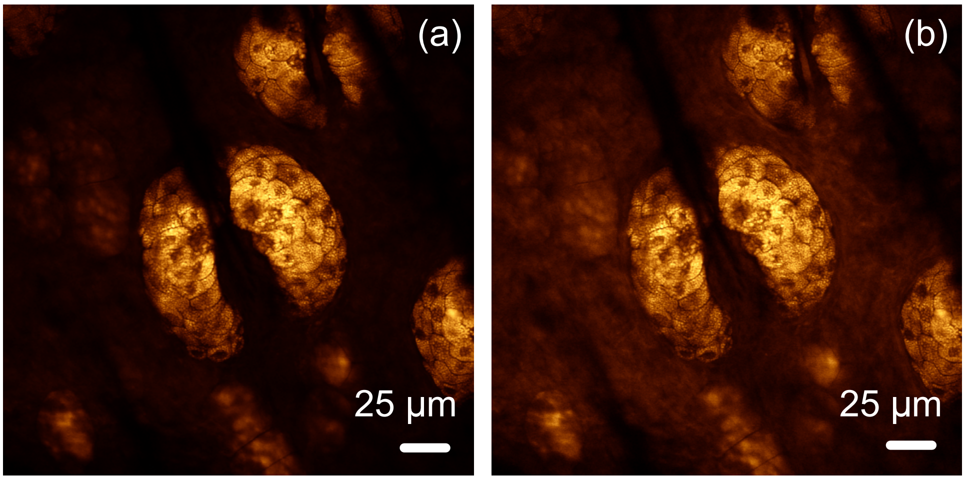

Figure 5.7: Epi-CARS images of sebaceous glands in mouse ear at the (a) 2850 cm^{-1} and (b) 2930 cm^{-1} frequency shifts, which show the increase in the protein signal at the 2930 cm^{-1} shift. 512 x 512 pixels at 2 μs per pixel, no averaging.

5.5 Intensity noise characterization of optical parametric oscillator

Compared to CARS, stimulated Raman scattering (SRS) microscopy has the advantages of being background-free and providing quantitative information on chemical concentration [21]. However, an extremely quiet source of pulses is required to detect SRS with an adequate signal-to-noise ratio for imaging. A fiber source that is quiet enough to perform SRS microscopy with direct detection has not been reported. Recent work has focused on alternate detection techniques that permit the use of fiber sources for SRS imaging, such as the collinear balanced detection described in [22, 8] and the demonstrated use of CW diode lasers with dual modulation in [23]. However, these techniques come at the cost of added electronic complexity, and, in the case of the CW source, significantly lower SRS signal and imaging speed than can be achieved with a pulsed source.

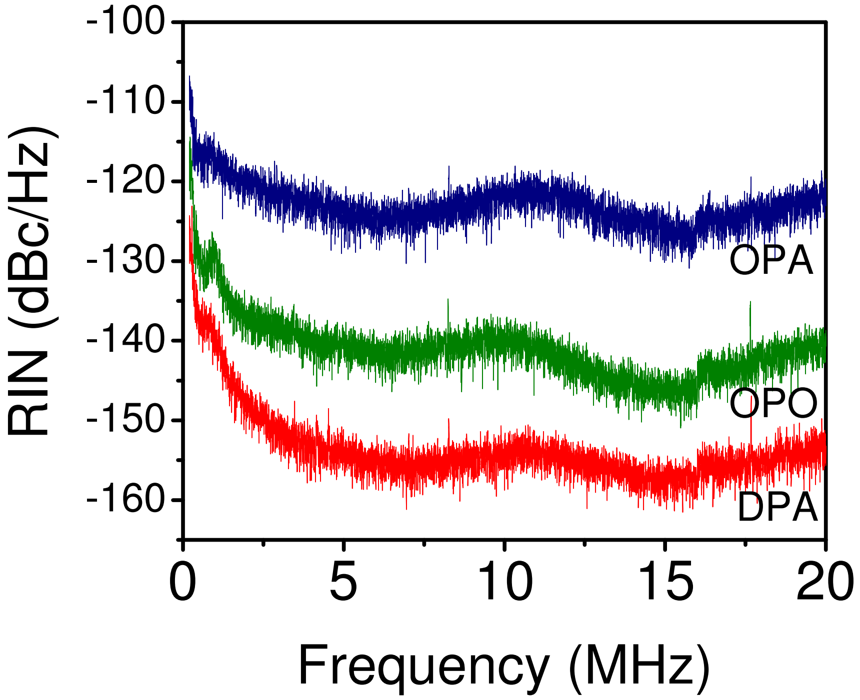

Figure 5.8: MHz RIN measurement on fiber sources for coherent Raman microscopy taken with a resolution bandwidth of 6.5 kHz. The OPA measurement references the work done in [13].

SRS imaging is typically performed by modulating one of the pulse trains at around 10 MHz and detecting the change in energy of the other pulse synchronously. RIN spectra for the source described here are shown in Fig. 5.8 along with that of the OPA based on the same FWM process [13]. The RIN of the seed laser is near the instrument floor of -165 dBc/Hz. After amplification, the RIN is around -155 dBc/Hz, and the OPO itself contributes 15 dBc/Hz across the spectrum in routine operation. The RIN of the fiber OPO is at least 20 dBc/Hz below that of the analogous OPA, which confirms the rationale for developing the OPO. However, the OPO is noisier than the target of better than -150 dBc/Hz for SRS imaging with direct detection.

5.6 Conclusion

In conclusion, we have demonstrated a picosecond fiber OPO based on FWM in PCF. The use of a narrow-band filter in the feedback loop is critical for stable operation of the OPO. The OPO matches the pulse parameters of solid-state sources and a fiber OPA, with intensity fluctuations much lower than the fiber OPA but greater than the solid-state OPO. Among fiber sources, the performance is the best reported to date, and yields CARS images with excellent signal-to-noise performance and fast imaging speeds.

BIBLIOGRAPHY

[1] E. S. Lamb, S. Lefrancois, M. Ji, W. J. Wadsworth, X. S. Xie, and F. W. Wise, Opt. Lett. **38**, 4154 (2013).

[2] E. S. Lamb, S. Lefrancois, M. Ji, W. J. Wadsworth, X. S. Xie, and F. W. Wise, Proc. SPIE 8948-15 (2014).

[3] C. L. Evans and X. S. Xie, Annual Review of Analytical Chemistry **1**, 883 (2008).

[4] F. Ganikhanov, S. Carrasco, X. S. Xie, M. Katz, W. Seitz, and D. Kopf, Opt. Lett. **31**, 1292 (2006).

[5] K. Kieu, B. G. Saar, G. R. Holtom, X. S. Xie, and F. W. Wise, Opt. Lett. **34**, 2051 (2009).

[6] I. Rimke, G. Hehl, M. Beutler, P. Volz, A. Volkmer, and E. Buttner, Proc. SPIE 8948-16 (2014).

[7] G. Krauss, T. Hanke, A. Sell, D. Träutlein, A. Leitenstorfer, R. Selm, M. Winterhalder, and A. Zumbusch, Opt. Lett. **34**, 2847 (2009).

[8] C. W. Freudiger, W. Yang, G. R. Holtom, N. Peyghambarian, X. S. Xie, and K. Q. Kieu, Nat Photon **8**, 153 (2014).

[9] N. Coluccelli, V. Kumar, M. Cassinerio, G. Galzerano, M. Marangoni, and G. Cerullo, Opt. Lett. **39**, 3090 (2014).

[10] E. R. Andresen, C. K. Nielsen, J. Thogersen, and S. R. Keiding, Opt. Express **15**, 4848 (2007).

[11] M. Baumgartl, T. Gottschall, J. Abreu-Afonso, A. Díez, T. Meyer, B. Dietzek, M. Rothhardt, J. Popp, J. Limpert, and A. Tünnermann, Opt. Express **20**, 21010 (2012).

[12] P. J. Mosley, S. A. Bateman, L. Lavoute, and W. J. Wadsworth, Opt. Express **19**, 25337 (2011).

[13] S. Lefrancois, D. Fu, G. R. Holtom, L. Kong, W. J. Wadsworth, P. Schneider, R. Herda, A. Zach, X. S. Xie, and F. W. Wise, Opt. Lett. **37**, 1652 (2012).

[14] M. Chemnitz, M. Baumgartl, T. Meyer, C. Jauregui, B. Dietzek, J. Popp, J. Limpert, and A. Tünnermann, Opt. Express **20**, 26583 (2012).

[15] J. E. Sharping, J. Lightwave Technol. **26**, 2184 (2008).

[16] Y.-H. Zhai, C. Goulart, J. E. Sharping, H. Wei, S. Chen, W. Tong, M. N. Slipchenko, D. Zhang, and J.-X. Cheng, Applied Physics Letters **98**, 191106 (2011).

[17] J. Hult, J. Lightwave Technol. **25**, 3770 (2007).

[18] R. Paschotta, Opt. Express **18**, 5041 (2010).

[19] S. Zhou, F. W. Wise, and D. G. Ouzounov, Opt. Lett. **32**, 871 (2007).

[20] K. Kieu and N. Peyghambarian, Proc. SPIE 7903-10 (2011).

[21] C. W. Freudiger, W. Min, B. G. Saar, S. Lu, G. R. Holtom, C. He, J. C. Tsai, J. X. Kang, and X. S. Xie, Science **322**, 1857 (2008).

[22] K. Nose, Y. Ozeki, T. Kishi, K. Sumimura, N. Nishizawa, K. Fukui, Y. Kanematsu, and K. Itoh, Opt. Express **20**, 13958 (2012).

[23] C.-R. Hu, M. N. Slipchenko, P. Wang, P. Wang, J. D. Lin, G. Simpson, B. Hu, and J.-X. Cheng, Opt. Lett. **38**, 1479 (2013).

CHAPTER 6

NORMAL DISPERSION FIBER LASERS FOR COHERENT RAMAN SCATTERING MICROSCOPY

6.1 Introduction

The previous chapter motivates the need for an ultra-quiet source of picosecond pulses to reduce the intensity noise in the fiber-based sources for coherent Raman scattering (CRS) microscopy. Since the relative intensity noise (RIN) of the optical parametric oscillator (OPO) output is consistently at least 10 dB above the RIN of the pump laser, a quieter pump laser at 1037 nm is necessary to achieve sufficiently quiet pulses at the signal wavelength [1]. Since picosecond fiber soliton lasers are limited to average powers on the order of 10 mW, which corresponds to a shot noise limit of -164 dBc/Hz, it is unlikely that a source starting from this laser will achieve the desired RIN level of -160 dBc/Hz for the 800 nm beam.

To address this problem, a high energy picosecond laser needs to be developed to reduce the shot-noise limit of the starting point. The divided-pulse soliton laser discussed in Chapter 3 [2] is one potential option. This chapter will analyze various alternatives for achieving quiet picosecond pulses by utilizing the higher pulse energies achievable form fiber lasers operating in the normal dispersion regime.

6.2 Picosecond laser based on narrow bandwidth spectral filter

One route to achieving picosecond pulses from a normal dispersion laser is to use a narrow bandwidth spectral filter, ideally narrower than the 2-4 nm filters that tend to yield broad bandwidth amplifier similariton pulses. Picosecond pulse generation from a cavity with a narrow filter has been demonstrated in reference [3], although little explanation is given into the pulse evolution inside of the cavity. The cavity design under consideration here is shown in Fig. 6.1. A 1200 lines/mm diffraction grating and collimator can form filter bandwidths on the order of 1 nm.

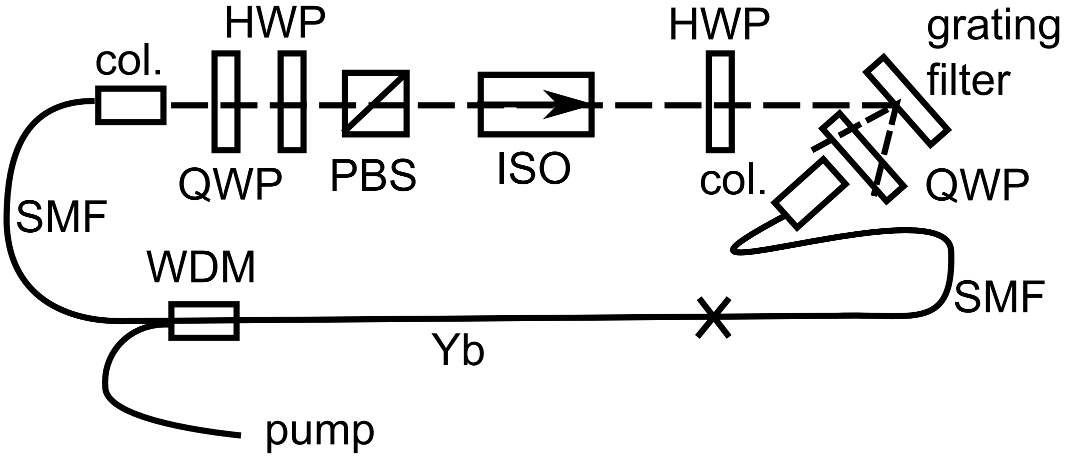

Figure 6.1: Schematic of picosecond laser cavity. HWP: half-wave plate; QWP: quarter-wave plate; PBS: polarizing beam splitter; ISO: isolator; col.: collimator; SMF: single mode fiber.

6.2.1 Modeling

Simulations for this cavity are run assuming a mode field area of 350 μm^2, which corresponds to the size of chirally-coupled core fiber or a large-core photonic crystal fiber. This is done to asses if this laser design can generate the 40-50 nJ needed to pump the fiber OPO without additional amplification. Also, it is advantageous to limit the amount of fiber in the cavity to reduce the amount of spectral broadening that will occur. Thus, the simulated cavity consists of 50 cm of passive fiber before the gain, a 50 cm length of gain fiber, and no passive fiber after the gain.

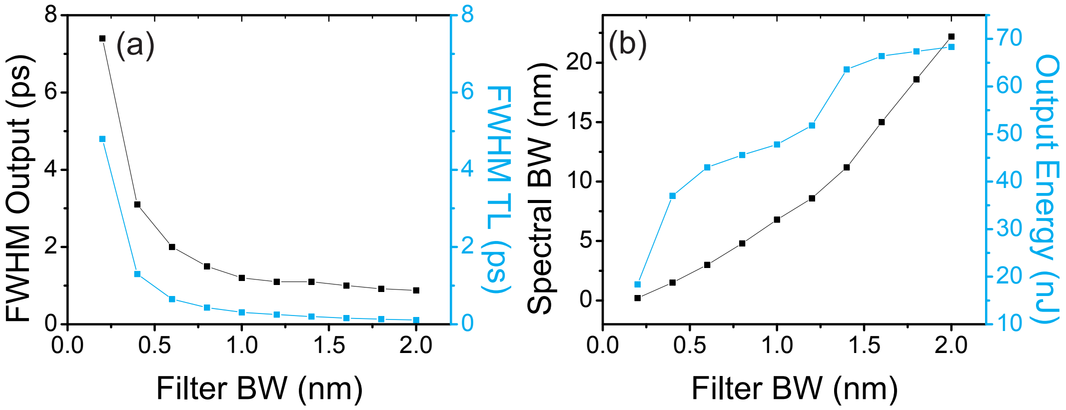

Figure 6.2: Trends for picosecond laser as a function of intra-cavity spectral filter bandwidth: (a) pulse duration; (b) spectral bandwidth and pulse energy. TL: transform limit.

The trends in pulse duration, spectral bandwidth, and pulse energy as the intra-cavity filter bandwidth is changed are shown in Fig. 6.2. Ideally, the pump pulse for the OPO should be longer than 3 ps in order for the OPO output pulse to be on the order of 1 ps. Fig. 6.2 indicates that spectral filters with bandwidths less than 0.5 nm will be needed to achieve these durations. With filters this narrow, it will be challenging to achieve 40-50 nJ directly from the oscillator, so modest amplification would be needed.

The pulse evolution inside the cavity for various filter bandwidths is shown in Fig. 6.3. Fig. 6.3(d) shows the expected evolution for an amplifier similariton laser [4], where the pulse duration is decreased by the action of the spectral filter, as expected for filtering of a chirped pulse. Fig. 6.3(a-c) demonstrates that narrower filters support the opposite behavior: the spectral filter acts to increase the pulse duration as is expected for a pulse closer to the transform limit. Finally,

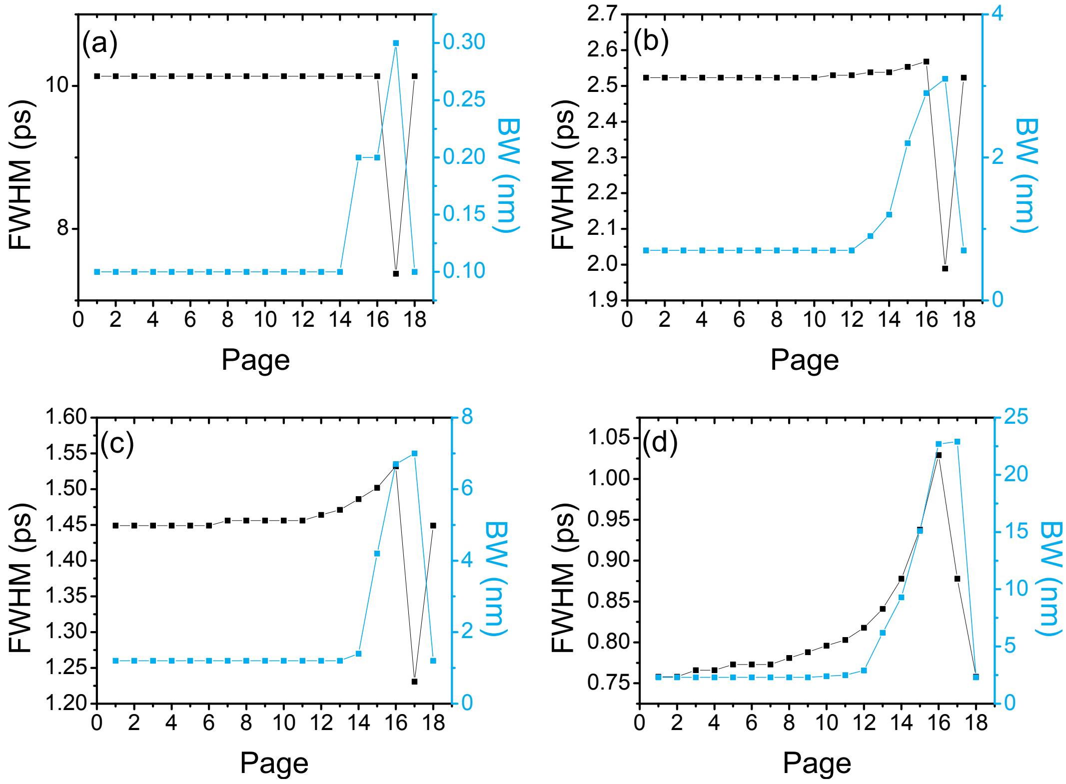

Figure 6.3: Pulse evolution for picosecond laser with spectral filter bandwidths of (a) 0.2 nm; (b) 0.6 nm; (c) 1.0 nm; and (d) 2.0 nm. Pages 1-8: passive fiber before gain; Pages 9-16: gain fiber: Page 17: saturable absorber; Page 18: spectral filter.

to assess how close the pulse gets to the parabolic asymptotic solution in the gain fiber, the M parameter is shown in Fig. 6.4. The M parameter is the difference integral between the pulse and a perfect parabola of the same peak power; thus, the pulse is a better approximation to a parabola as the M parameter tends towards zero. Fig. 6.4 shows that there is little attraction in the gain segment for narrower filters, and the pulse becomes more strongly attracted to a parabola as the filter bandwidth increases. With the 2.0 nm filter, the pulse is reaching the threshold to be considered a parabola, as expected. With the narrower filters that produce picosecond pulse durations, the saturable absorber appears to be the most important pulse shaping mechanism.

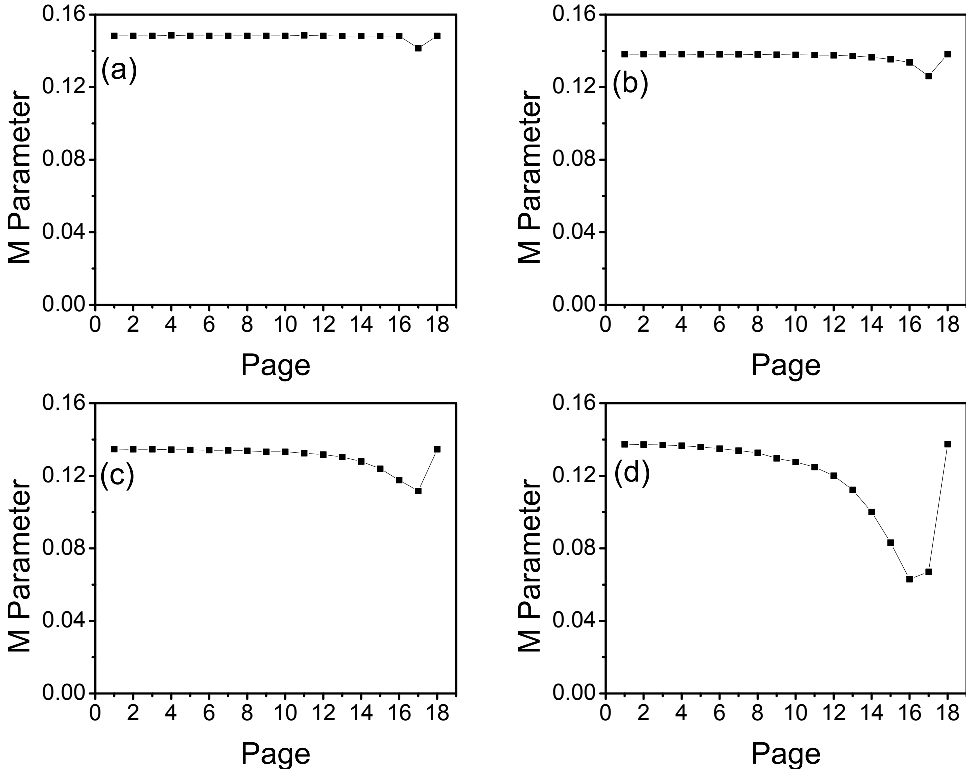

Figure 6.4: M parameter for picosecond laser with spectral filter bandwidths of (a) 0.2 nm; (b) 0.6 nm; (c) 1.0 nm; and (d) 2.0 nm.

6.2.2 Experiment

The laser shown in Fig. 6.1 is constructed in single mode fiber for preliminary experiments. Fig. 6.5 shows the mode-locked spectrum and RIN curve for this laser. The spectrum is around 1 nm wide. The filter is implemented using a 1200 lines/mm grating 3-4 cm away from the collimator to form a 1 nm bandwidth. With larger spacing between the grating and the collimator, the laser will tend to form soliton pulses due to the anomalous dispersion introduced by the grating. At wider filter bandwidths, the laser will produce amplifier similariton pulses, so there is a relatively narrow range of achievable filter bandwidths that produce the narrow-band outputs.

At the 57 MHz repetition rate, the 1.5 nJ pulse energy corresponds to an

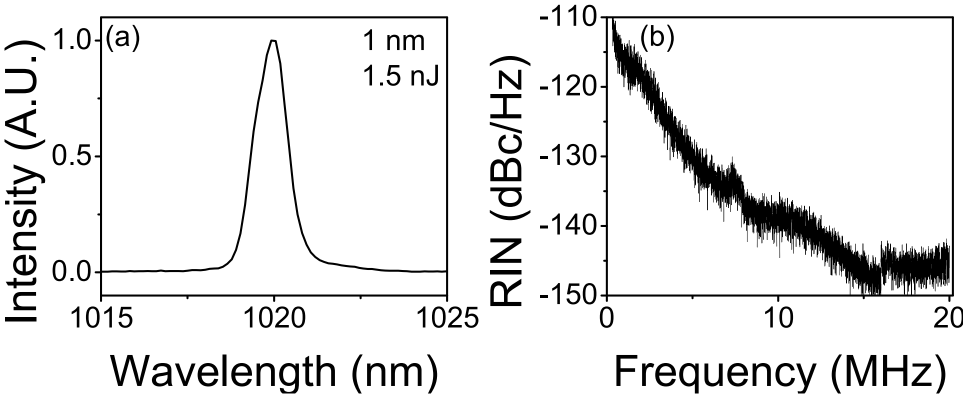

Figure 6.5: (a) Spectrum and (b) RIN curve for picosecond laser with narrow bandwidth filter.

average power of 87 mW, which has a shot noise limit of -176.5 dBc/Hz. Fig. 6.5 shows that the RIN of this laser is over 20 dB above shot noise, so this laser would require signification noise optimization to be a suitable candidate for stimulated Raman scattering (SRS) microscopy. Using a different narrow-band filter that would de-couple the filter bandwidth from the amount of anomalous dispersion may make it easier to achieve even narrower bandwidth spectra, but it is unclear if this would have a beneficial effect on the RIN levels.

6.3 Spectral compression of dissipative soliton lasers[1]

Multiphoton fluorescence microscopy continues to find new and exciting applications. Second- and third-harmonic generation imaging share some benefits with multiphoton imaging, while offering complementary capabilities. Femtosecond light pulses are generally used for multiphoton and harmonic-generation microscopies. Imaging techniques based on Raman processes, including coherent anti-Stokes Raman scattering (CARS) and stimulated Raman scattering (SRS) mi-

---

[1] Much of the work presented in this section was published in the Proceedings of the SPIE [5] and is under review for Biomedical Optics Express.

croscopy, also continue to proliferate [6]. Raman microscopies typically require two synchronized picosecond pulse trains, with the frequency difference between the two colors tunable to match the vibrational resonances of interest. Despite the technical success of the solid state laser and optical parametric oscillator (OPO) commonly used for CARS and SRS microscopy [7], its cost, size, complexity, and sensitive alignment will limit its use outside of specialized laboratories. This has motivated the development of fiber-based sources of picosecond pulses for Raman imaging. Some studies employ multiple nonlinear-imaging modalities, which generally require that both femtosecond and picosecond lasers be available. A robust source capable of providing both types of pulses would greatly facilitate such work.

Numerous fiber-based systems have been developed for Raman imaging. In a hybrid approach, fiber lasers are used to pump solid-state OPOs [8, 9]. Fiber lasers can also be used with various nonlinear processes in fiber to generate the second color [10, 11, 12]. Finally, four-wave mixing (FWM) in the normal dispersion region of photonic crystal fiber (PCF) is employed to frequency-convert picosecond pulses from ytterbium-doped fiber lasers [13, 1, 14, 15]. In addition to matching the pulse parameters needed for CARS, sources for SRS microscopy need to have ultra-low intensity noise. To date, no all-fiber source has achieved low enough intensity noise to be suitable for SRS microscopy with direct detection. Instead, Freudiger and coworkers demonstrated that electronic balanced detection may be used for cancellation of the noise on fiber sources [11], and Rimke *et al.* showed that a solid-state OPO pumped by an amplified fiber laser can achieve low enough noise on the frequency-shifted pulse train [16].

In addition to sources designed to meet the pulse parameters necessary for Raman microscopies, there is interest in developing sources that are suitable for multiple imaging modalities. Huff and coworkers constructed a multimodal source based on two synchronized picosecond titanium sapphire lasers to provide the desired pulse parameters for CARS [17]. Their system also uses the picosecond pulses to achieve two-photon excitation florescence (TPEF) and sum-frequency generation (SFG) images, which sacrifices performance compared to the use of femtosecond pulses in these imaging techniques. Kumar *et al.* perform single pulse CARS microscopy in conjunction with multiphoton imaging using a titanium sapphire laser and notch filters scanned by a galvanometer [18]. Fiber-based systems are attractive for these applications since they can reduce alignment sensitivity and cost. Xie *et al.* demonstrated a partially fiber source based on a femtosecond titanium sapphire laser used to perform CARS, SRS, and photothermal imaging [19]. The second color required for Raman imaging was generated through the soliton self-frequency shift in PCF. Again, this source is limited to very low powers (less than 10 mW) at 75 MHz and does not have the optimal picosecond durations for the Raman techniques. Two other sources demonstrate further fiber integration. One uses FWM of femtosecond pulses in PCF to yield a source capable of performing CARS microscopy and TPEF imaging [20]. However, the femtosecond pulses limit spectral resolution in CARS imaging, and the system is limited to 0.5 nJ at the signal wavelength. Finally, Meyer and coworkers demonstrate an all-fiber source for CARS, TPEF, and SHG microscopy that operates with pulses durations of tens of picoseconds [21]. In summary, to the best of our knowledge, no multimodal source has been demonstrated that is capable of providing both the optimal synchronized picosecond pulses for the Raman microscopies and the high energy femtosecond pulses for multiphoton techniques.

Here we demonstrate the use of spectrally-compressed femtosecond pulses from a dissipative-soliton laser to pump a fiber OPO [1]. The OPO generates the second pulse train necessary for CARS and SRS microscopies. By utilizing a high-power femtosecond fiber laser [22, 23] for the pump pulse, the same robust platform is capable of producing picosecond and femtosecond pulses near 1040 nm. The high energy femtosecond pulses from this laser have been used for TPEF and second harmonic generation (SHG) microscopy [24, 25, 26], so the source presented here provides suitable pulses for multiphoton and harmonic-generation imaging with a single excitation wavelength, as well as CARS microscopy. As an additional motivation, SRS microscopy stands to benefit from an ultra-low noise fiber source. Since femtosecond lasers tend have much higher powers than picosecond lasers, replacement of the low-power picosecond soliton lasers typically used as the seed laser with a higher power laser reduces the shot-noise limit of the intensity noise in the source. Thus, the development of high-power femtosecond lasers as a source of quiet picosecond pulses may offer a route to quieter fiber sources. Extensions of the source to provide tunable femtosecond pulses will also be discussed.

6.3.1 Simulation of spectral compression

Dissipative-soliton lasers, which are based on all-normal-dispersion designs, tend to provide the highest-energy pulses for given core size. The performance of these lasers has been well documented [27]. They generate chirped femtosecond pulses; we assess spectral compression of the output pulses to create transform-limited picosecond pulses. Spectral compression occurs when a down-chirped pulse is launched into a nonlinear material [28, 29]. Figure 6.6(a) shows the calculated spectral compression ratio versus impressed anomalous dispersion for 4 nJ transform limited Gaussian pulses with the indicated initial durations. The spectral compression is performed in passive fiber with a 10 μm core diameter up to 100 m

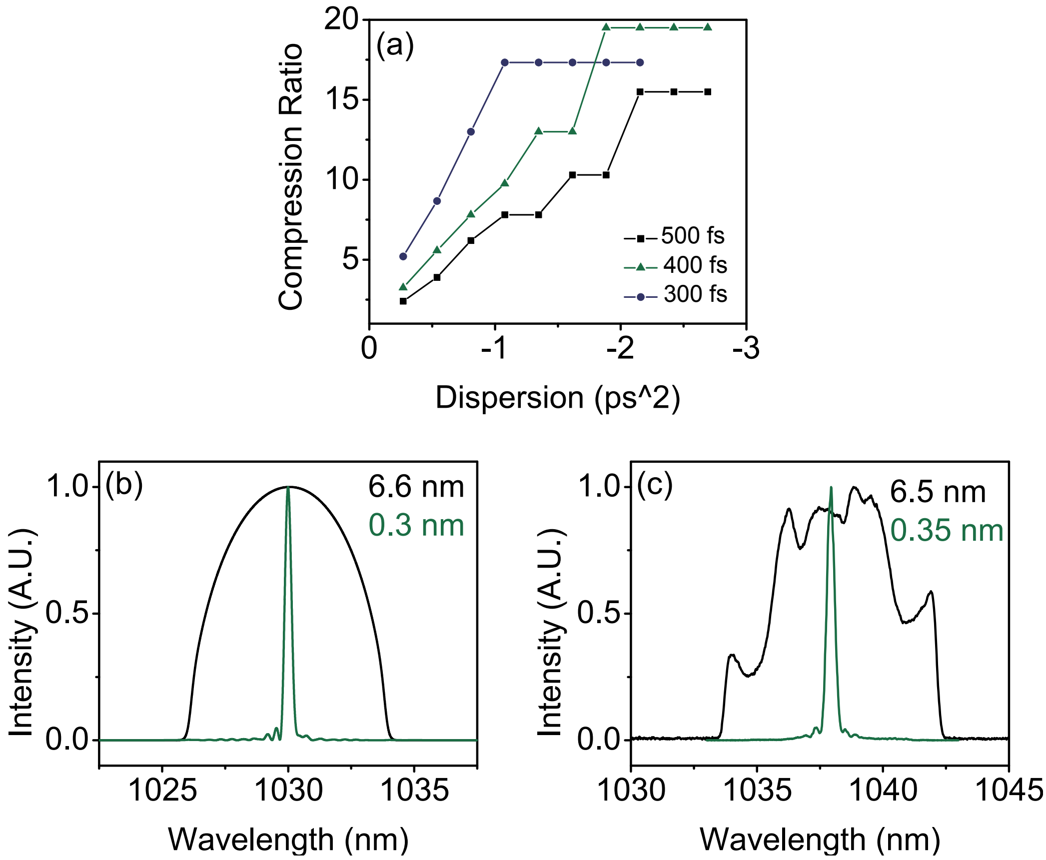

Figure 6.6: Spectral compression. (a) Simulation trends for 4 nJ transform limited Gaussian pulses with the initial pulse duration given in the legend. Compression is performed in fiber lengths of 50-100 m with the length selected to give the minimum spectral bandwidth. (b) Simulated spectral compression of a 4 nJ dissipative soliton. (c) Experimental spectral compression of a 1 nJ dissipative soliton.

long; the length is chosen to minimize the compressed bandwidth. These trends indicate that larger compression ratios can be achieved by impressing larger amounts of negative chirp on the pulse and then compressing the spectrum in correspondingly longer lengths of fiber. Fig. 6.6(b) shows compression of a simulation of a dissipative soliton.

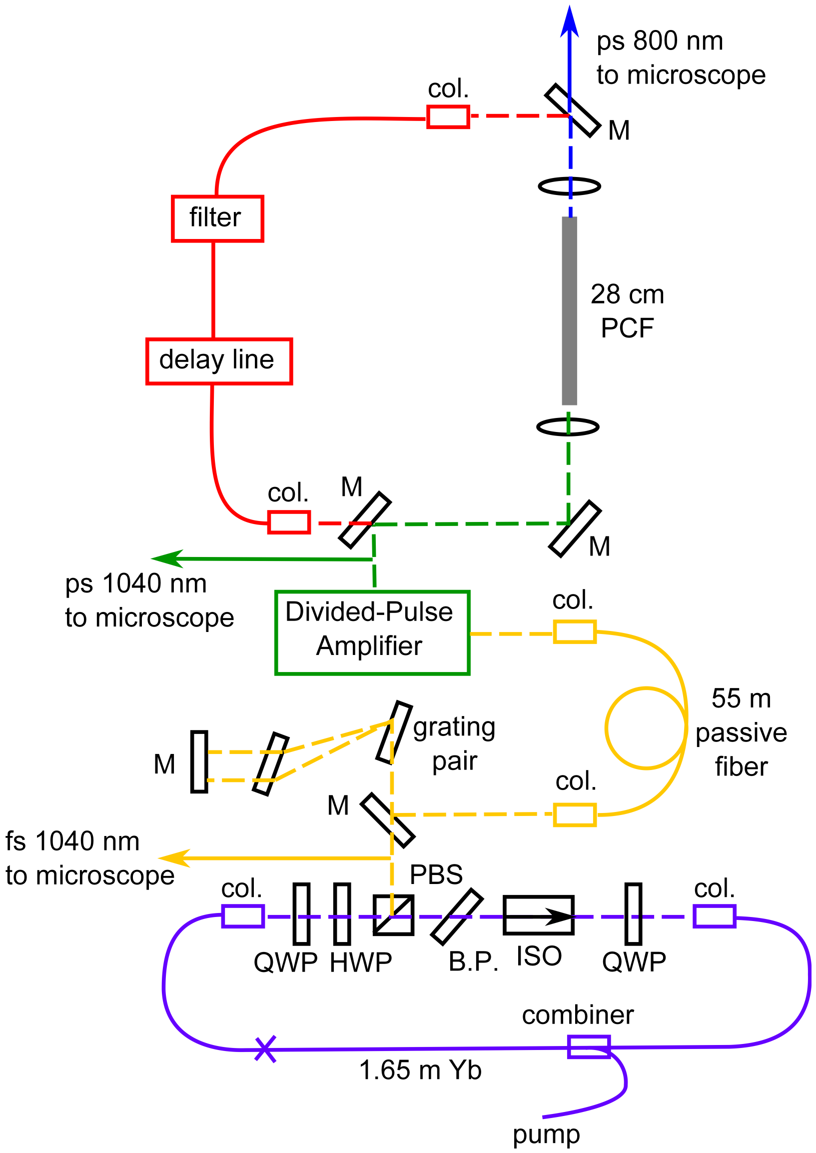

Figure 6.7: Schematic of multimodal microscopy source showing the dissipative soliton laser (purple), spectral compression stage (yellow), divided-pulse amplifier (green), and optical parametric oscillator (red). col.: collimator; QWP: quarter-wave plate; HWP: half-wave plate; PBS: polarizing beam splitter; B.P. birefringent plate; ISO: isolator; M: mirror; PCF: photonic crystal fiber.

6.3.2 Experimental Results

The experimental set-up is shown in Fig. 6.7. The dissipative soliton laser is based on double-clad Yb-doped fiber with a 10 μm core diameter (Liekki), similar to the cavity presented by Kieu *et al.* [23]. The repetition rate of the cavity is 21.4 MHz, which is selected for ease of producing spectral bandwidths near 10 nm. These spectra are ideal for spectral compression to picosecond pulse durations. The fiber leads on the collimators and combiner are passive fiber with 10 μm core size. Around 5.5 m of HI1060 (Corning) fiber is added before the gain to bring the repetition rate to 21.4 MHz; the smaller-core fiber is used to reduce multimode content in the laser. The HI1060 fiber is spliced on both ends to SMF28e+ (Corning), which is then spliced to the 10 μm fiber to reduce splicing loss. A quartz plate is used for the birefringent filter, which provides a bandwidth around 8 nm.

In standard operation [23], the laser generates pulses with over 20 nm bandwidth and over 10 nJ pulse energy, providing a source of femtosecond pulses after standard dechirping with a grating pair. To achieve the near-transform limited picosecond durations, better results are obtained if the laser is mode-locked with a spectral bandwidth below 10 nm. These spectra are easily obtained with minor adjustment of the waveplates and no other change to the cavity. The chirp on the output pulse is reversed with a grating pair (LightSmyth Technologies, 1600 lines/mm) that provides -3.3 ps^2 of anomalous dispersion, and then spectral compression is performed in around 55 m of passive fiber with 10 μm core diameter. A typical result is shown in Fig. 6.6(c) to show the excellent agreement with simulation. A second compressed spectrum and the corresponding autocorrelation are shown in Figs. 6.8(a) and (b) to highlight the fact that spectra with different shapes, but similar bandwidths near the base of the spectrum, yield similar results. Although the initial pulse energies are over 10 nJ, only 1-1.5 nJ remains after compression. Most of the loss occurs in coupling the beam back into fiber for the compression, due to the spatial chirp induced by the high density grating pair; this could be optimized in the future if needed.

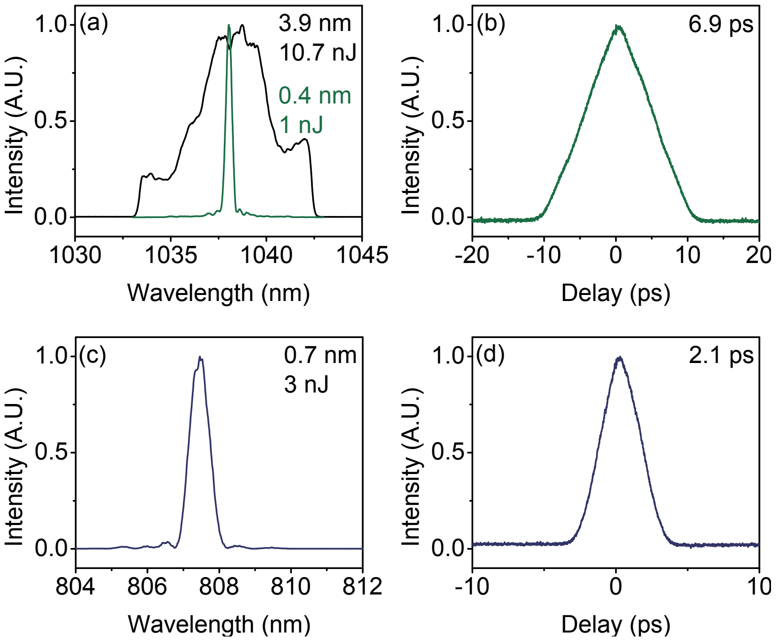

Figure 6.8: Spectrally compressed dissipative soliton laser: (a) spectrum and (b) autocorrelation. Signal pulses from optical parametric oscillator: (c) spectrum and (d) autocorrelation.

The 7 ps pulses are amplified to 40 nJ in a divided-pulse amplifier [30]. These pulses are used to pump the OPO described previously [1] and shown in Fig. 6.7. A Fabry-Perot filter (OZ optics) replaces a grating-based filter [1] in the feedback loop; this serves to decouple the OPO path length from the resonant wavelength. The long-wavelength FWM product is resonated in the cavity. With 15-20 nJ coupled into 28 cm of PCF (5 μm core, zero dispersion wavelength near 1051 nm), 3 nJ of signal pulses can be generated around 800 nm. This corresponds to conversion efficiencies of 15-20%. Over 10 nJ of the 1040 nm pulses can be picked-off before the OPO to serve as the Stokes light for CARS or SRS microscopy while maintaining similar performance from the OPO. Signal pulse energies up to 4-5 nJ can be generated from the OPO at higher pump powers, but the spectra become more structured and the intensity fluctuations increase. The pulse parameters for both beams are similar to the previously-reported performance [1], so this source is well suited for CARS microscopy in the popular C-H stretch region of the spectrum. The tuning range of the OPO signal wavelength is around 790-820 nm, and is currently limited by the 1450-1500 nm tuning range of the Fabry-Perot filter in the feedback loop. In this experiment, free-space coupling of light into and out of the PCF was used for ease of optimization; an all-fiber version of this OPO was recently demonstrated and it exhibits similar performance [5].

Greater wavelength tunability will increase the usefulness of this source. Currently, the femtosecond pulses are tunable over the bandwidth of the ytterbium gain medium. Fiber OPOs have been designed to achieve tunable femtosecond pulses with up to 2 nJ of pulse energy, as demonstrated in references [31, 32]. Recent results from Kieu and coworkers show that high energy femtosecond pulses can be created from a picosecond-pumped fiber OPO by exploiting dissipative-soliton formation in the OPO cavity [33]. Since the pulse duration from the spectrally compressed dissipative-soliton laser presented here is tunable over a wide range through mode-locking and compressing different spectra, it is capable of providing pump pulses for various fiber OPOs optimized for femtosecond pulse generation. Thus, the addition of a femtosecond fiber OPO to the set-up demonstrated here would provide a natural route for extending the wavelength tunability of the femtosecond pulses.

One motivation for replacing the low-power soliton laser typically used to generate the seed pulses in fiber-based systems for Raman imaging is the potential to start with a higher energy pulse, which has a lower shot noise limit. This is particularly important for SRS microscopy, which requires a nearly shot-noise limited source in the 10-20 MHz frequency range used for lock-in detection. In the source

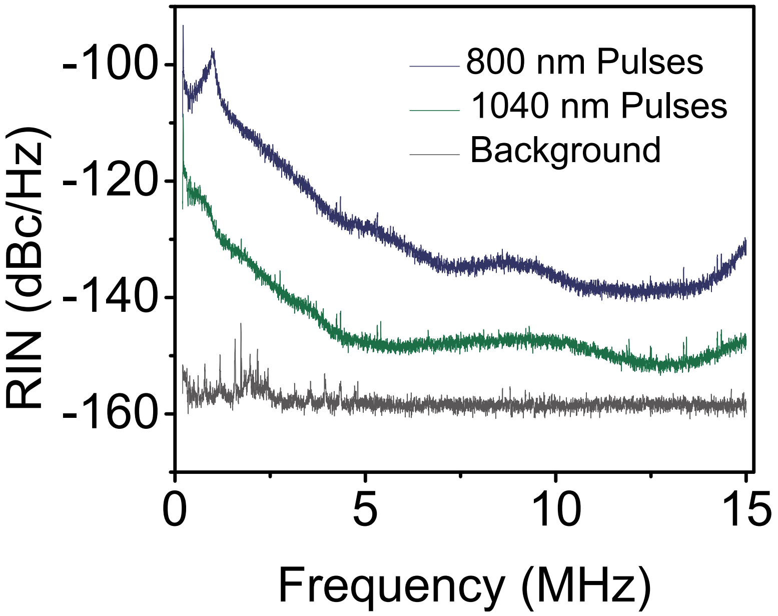

Figure 6.9: Intensity noise spectra for the 1040 nm and 800 nm pulse trains. Data taken with a Signal Hound SA44B analyzer with a resolution bandwidth of 6.5 kHz.

presented here, the spectrally compressed pulses have 20-30 mW of average power. After amplification, the 1040 nm pulses have relative intensity noise (RIN) around −150 dBc/Hz (Fig. 6.9). The OPO itself adds around 10 dB of noise, yielding a RIN around −140 dBc/Hz at 800 nm. This is comparable to the RIN achieved using the soliton seed pulse [1], and would be suitable for SRS microscopy with balanced detection [11]. However, the higher starting average power in this system makes it possible to improve the noise performance of this source by optimization of the laser. Eventually, it may be advantageous to construct a dissipative-soliton laser with large-core fiber, which can directly produce 40 nJ pulses for pumping the OPO without amplification [34, 35]. This would reduce the shot noise limit of the pump pulses even further, and eliminate the RIN added during amplification. As a practical benefit, elimination of the amplifier would also reduce the number of parts and complexity of the set-up.

6.3.3 Conclusion

In conclusion, we have demonstrated a fiber source based on a spectrally-compressed dissipative-soliton laser and a fiber OPO capable of producing the two picosecond pulse trains ideal for CARS and SRS microscopy. This is the first demonstration that dissipative soliton lasers can provide a route to a Raman scattering microscopy source. In addition, the dissipative soliton laser can produce high energy femtosecond pulses at 1040 nm that are suitable for other imaging modalities, such as TPEF and SHG microscopy [24, 25, 26], and the wavelength tunability could be extended by using the pulses to pump a fiber OPO optimized for femtosecond pulse generation. Although the source is not yet quiet enough for SRS microscopy with direct detection, this device provides RIN levels comparable to the best achieved by fiber sources to date and could be further optimized for low-noise operation through the design of the laser and through energy scaling with large core fibers. A fiber source able to provide the correct pulse parameters for Raman and multiphoton microscopies could provide a tremendous cost advantage and extend the application of these techniques.

BIBLIOGRAPHY

[1] E. S. Lamb, S. Lefrancois, M. Ji, W. J. Wadsworth, X. S. Xie, and F. W. Wise, Opt. Lett. **38**, 4154 (2013).

[2] E. S. Lamb, L. G. Wright, and F. W. Wise, Opt. Lett. **39**, 2775 (2014).

[3] P. Deslandes, M. Perrin, J. Saby, D. Sangla, F. Salin, and E. Freysz, Opt. Express **21**, 10731 (2013).

[4] W. H. Renninger, A. Chong, and F. W. Wise, Phys. Rev. A **82**, 021805 (2010).

[5] E. S. Lamb, H. Pei, and F. W. Wise, Proc. SPIE 9329-70 (2015).

[6] A. Alfonso-García, R. Mittal, E. S. Lee, and E. O. Potma, Journal of biomedical optics **19**, 71407 (2014).

[7] F. Ganikhanov, S. Carrasco, X. S. Xie, M. Katz, W. Seitz, and D. Kopf, Opt. Lett. **31**, 1292 (2006).

[8] K. Kieu, B. G. Saar, G. R. Holtom, X. S. Xie, and F. W. Wise, Opt. Lett. **34**, 2051 (2009).

[9] I. Rimke, G. Hehl, M. Beutler, P. Volz, A. Volkmer, and E. Buttner, Proc. SPIE 8948-16 (2014).

[10] G. Krauss, T. Hanke, A. Sell, D. Träutlein, A. Leitenstorfer, R. Selm, M. Winterhalder, and A. Zumbusch, Opt. Lett. **34**, 2847 (2009).

[11] C. W. Freudiger, W. Yang, G. R. Holtom, N. Peyghambarian, X. S. Xie, and K. Q. Kieu, Nat Photon **8**, 153 (2014).

[12] N. Coluccelli, V. Kumar, M. Cassinerio, G. Galzerano, M. Marangoni, and G. Cerullo, Opt. Lett. **39**, 3090 (2014).

[13] S. Lefrancois, D. Fu, G. R. Holtom, L. Kong, W. J. Wadsworth, P. Schneider, R. Herda, A. Zach, X. S. Xie, and F. W. Wise, Opt. Lett. **37**, 1652 (2012).

[14] M. Baumgartl, T. Gottschall, J. Abreu-Afonso, A. Díez, T. Meyer, B. Dietzek, M. Rothhardt, J. Popp, J. Limpert, and A. Tünnermann, Opt. Express **20**, 21010 (2012).

[15] T. Gottschall, T. Meyer, M. Baumgartl, B. Dietzek, J. Popp, J. Limpert, and A. Tünnermann, Opt. Express **22**, 21921 (2014).

[16] I. Rimke, G. Hehl, M. Beutler, P. Volz, E. Büttner, and A. Volkmer, Proc. SPIE 9329-69 (2015).

[17] T. B. Huff, Y. Shi, Y. Fu, H. Wang, and J.-X. Cheng, Selected Topics in Quantum Electronics, IEEE Journal of **14**, 4 (2008).

[18] S. Kumar, T. Kamali, J. M. Levitte, O. Katz, B. Hermann, R. Werkmeister, B. Považay, W. Drexler, A. Unterhuber, and Y. Silberberg, Opt. Express **23**, 13082 (2015).

[19] R. Xie, J. Su, E. C. Rentchler, Z. Zhang, C. K. Johnson, H. Shi, and R. Hui, Biomed. Opt. Express **5**, 2390 (2014).

[20] Y.-H. Zhai, C. Goulart, J. E. Sharping, H. Wei, S. Chen, W. Tong, M. N. Slipchenko, D. Zhang, and J.-X. Cheng, Applied Physics Letters **98**, 191106 (2011).

[21] T. Meyer, M. Baumgartl, T. Gottschall, T. Pascher, A. Wuttig, C. Matthäus, B. F. M. Romeike, B. R. Brehm, J. Limpert, and A. Tünnermann, Analyst **138**, 4048 (2013).

[22] A. Chong, J. Buckley, W. Renninger, and F. Wise, Opt. Express **14**, 10095 (2006).

[23] K. Kieu, W. H. Renninger, A. Chong, and F. W. Wise, Opt. Lett. **34**, 593 (2009).

[24] C. Xu and F. W. Wise, Nat Photon **7**, 875 (2013).

[25] F. W. Wise, Selected Topics in Quantum Electronics, IEEE Journal of **18**, 1412 (2012).

[26] G. Liu, K. Kieu, F. W. Wise, and Z. Chen, Journal of Biophotonics **4**, 34 (2011).

[27] A. Chong, W. H. Renninger, and F. W. Wise, J. Opt. Soc. Am. B **25**, 140 (2008).

[28] S. A. Planas, N. L. P. Mansur, C. H. B. Cruz, and H. L. Fragnito, Opt. Lett. **18**, 699 (1993).

[29] M. Oberthaler and R. A. Höpfel, Applied Physics Letters **63**, (1993).

[30] S. Zhou, F. W. Wise, and D. G. Ouzounov, Opt. Lett. **32**, 871 (2007).

[31] C. Gu, H. Wei, S. Chen, W. Tong, and J. E. Sharping, Opt. Lett. **35**, 3516 (2010).

[32] J. E. Sharping, C. Pailo, C. Gu, L. Kiani, and J. R. Sanborn, Opt. Express **18**, 3911 (2010).

[33] K. Q. Kieu, D. E. Churin, R. Gowda, T. Ota, Y. Inoue, S. Uno, and N. Peyghambarian, Proc. SPIE 9344-97 (2015).

[34] S. Lefrançois, K. Kieu, Y. Deng, J. D. Kafka, and F. W. Wise, Opt. Lett. **35**, 1569 (2010).

[35] M. Baumgartl, F. Jansen, F. Stutzki, C. Jauregui, B. Ortaç, J. Limpert, and A. Tünnermann, Opt. Lett. **36**, 244 (2011).

CHAPTER 7

FUTURE DIRECTIONS

This chapter assesses future research areas relating to the work presented in the rest of this thesis, with a particular emphasis on the divided-pulse lasers and fiber sources for coherent Raman scattering microscopy. Simulations of four-wave mixing within laser cavities are also presented.

7.1 Divided-pulse lasers

Intra-cavity coherent pulse division and recombination has been introduced as an energy scaling mechanism for mode-locked lasers. The divided-pulse laser (DPL) technique is shown to provide 16x scaling of the pulse energy from a picosecond soliton laser, and very preliminary experiments show that the technique is compatible with dispersion-managed soliton lasers and dissipative soliton lasers, although further optimization is needed to show good performance from these cavities.

Considering that the DPL technique is arguably more complex than using a low-power oscillator and amplifier, and currently requires free-space components for the implementation of the pulse division and recombination, its advantage lies in applications where it can achieve a performance level that an amplifier cannot. One example of this would be in applications where shot-noise limited intensity noise is required; the output from a laser can be shot-noise limited, and amplifiers generally add at least 3 dB worth of excess noise.

DPLs may be advantageous in applications where modest amplification of pulses is needed. The DPL technique allows the pulse energy to be scaled by the number of divided pulses, ideally while maintaining identical pulse parameters. This could allow for energy scaling without gain narrowing or loss of pulse contrast from amplified spontaneous emission.

One limitation of the DPL implementation shown in Chapter 3 is that the semiconductor saturable absorber mirror (SESAM) has a tendency to damage at high pulse energies. Thus, to extend DPLs to pulse evolutions that support higher energy pulses, or to higher division ratios, it will be important to use a different saturable absorber. To take full advantage of the otherwise environmentally stable design, a nonlinear optical loop mirror or nonlinear amplifying loop mirror (NOLM/NALM) implemented in polarization-maintaining fiber would be a good option. For more flexibility, nonlinear polarization evolution (NPE) restricted to a portion of the cavity could be used. Ideally, this would be implemented in a portion of the cavity that sees the combined pulse so as to maintain strict control over the pulse polarization between division and recombination.

7.1.1 Divided-pulse amplifier similariton lasers

Of the known pulse evolutions in fiber lasers, the amplifier similariton may be the most difficult to implement using a DPL technique due to the need for a narrowband spectral filter before the gain, the large spectral breathing that occurs within the cavity, and the need for a high modulation depth saturable absorber [1]. This makes it an interesting case to consider to assess limitations and challenges of DPLs.

A proposed ring-cavity implementation of the divided-pulse amplifier similariton laser is shown in Fig. 7.1. Since SESAMs do not exhibit the high modulation depth needed to support amplifier similariton pulses, this cavity uses NPE

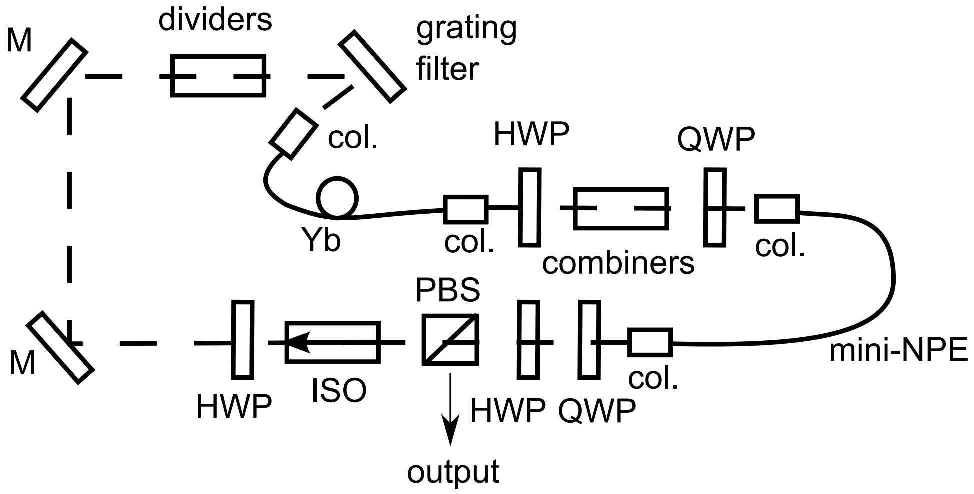

Figure 7.1: Schematic of proposed divided-pulse amplifier similariton laser. HWP: half-wave plate; QWP: quarter-wave plate; ISO: isolator; col.: collimator; M: mirror.

restricted to a segment of the cavity (mini-NPE), with the NPE rejection port serving as the output coupler. Also, since the narrow-band filter before the gain segment is a critical element of the laser cavity, it may be advantageous to use separate division and recombination stages to avoid the double-pass through the filter. It also may be necessary to implement the division and recombination using beam splitters to avoid complications from the large spectral breathing in the presence of the wavelength dependent index of refraction of birefringent crystals. Experiments using divided-pulse nonlinear compression indicate that the use of crystals for division and recombination can cause fringes on the recombined spectrum [2]. Although this effect is non detrimental in the pulse compression example (the fringes appear around 10 dB below the peak), it is reasonable to expect imperfections in the recombination process to pose greater challenges inside of a laser cavity.

7.2 Fiber sources for coherent Raman scattering microscopy

The previous chapters document work on creating fiber-based sources for coherent Raman scattering (CRS) microscopy. Since the fiber optical parametric oscillator (OPO) described in Chapter 5 can be used to achieve high quality images using coherent anti-Stokes Raman scattering (CARS) microscopy [3], the remaining challenge for fiber-based sources is achieving the ultra low-noise performance needed for stimulated Raman scattering (SRS) microscopy.

7.2.1 Development of quiet picosecond lasers

Given the current design of the OPO, which consistently produces signal pulses with relative intensity noise (RIN) levels at least 10 dB higher than the pump laser, it will be necessary to design a nearly shot-noise limited pump laser at 1037 nm with average powers ideally above 150 mW. This power level corresponds to shot noise levels below -175 dBc/Hz, so the RIN of the signal pulses should then be below -160 dBc/Hz, allowing for SRS imaging with direct detection and high signal to noise ratios.

Currently, the most promising routes to high power picosecond pulses without the need for amplification are the soliton DPL (Chapter 3) [4], the picosecond pulses generated via a narrow-band intra-cavity filter (Chapter 6), and spectral compression of high power femtosecond lasers (Chapter 6). All three of these options require challenging optimization of the laser performance to achieve the proper pulse parameters simultaneously with low-noise operation. Ideally, one of these systems would be implemented in a large-core fiber to achieve enough pulse energy to pump the OPO without additional amplification (40-50 nJ). This would save the additional noise added in the amplifier, as well as simplify the final source by eliminating the amplification stage.

Continuation of the simulations and preliminary experiments on the RIN of fiber lasers shown in Chapter 4 may provide insight into the best approach for developing low-noise fiber lasers. The results shown in this thesis indicate that dissipative soliton lasers are capable of high energy, low noise operation, making them well-suited for Raman imaging applications. It will be important to study optimization of this laser to simultaneously achieve the best noise performance and the ideal parameters for spectral compression when picosecond pulses are needed.

7.2.2 Using residual pump light

Using the shortest pulses that fill the Raman linewidth gives the maximal CARS or SRS signal for a given average power. Given that that the signal pulses from the OPO tends to be a factor of 3-4 shorter than the pump pulses, de-chirping the residual pump light may be a way to increase the Raman signal level, which could be especially beneficial for SRS microscopy where the higher signal can alleviate the noise constraints to a small extent.

Fig. 7.2(a) shows a signal spectrum generated from the OPO, and Figs. 7.2(b) and (c) show the residual pump spectrum and de-chirped pulse, respectively. The pulse compresses to within a factor of two of the transform limit, and is around a factor of 5 shorter than the pump pulses before the OPO. Using this pulse duration should increase the CARS or SRS signal by the same factor of 5. As

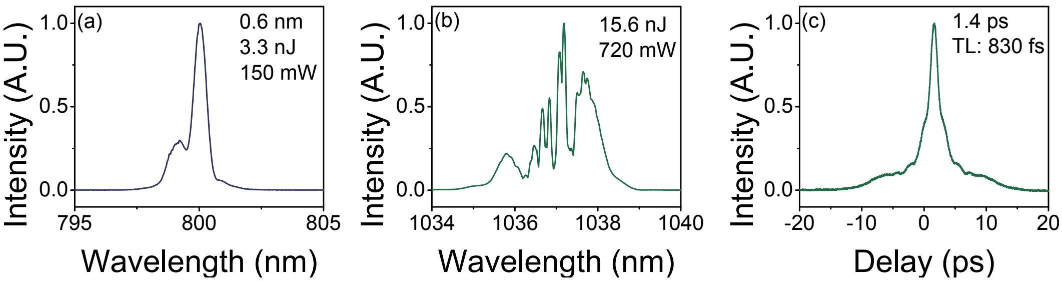

Figure 7.2: Compressed residual pump light from fiber OPO: (a) signal spectrum; (b) residual pump spectrum; (c) compressed residual pump pulses.

an additional advantage, more energy can be achieved in the 1037 nm pulse with less amplification by using the residual pump light from the OPO, so the CARS or SRS signal could be increased further through the use of more energy at this wavelength.

One potential drawback to using the residual pump light is the fact that the spectrum and pulse are not smooth due to the energy transfer to the signal and idler beams. Using this pulse in an imaging experiment will be needed to assess the impact of this effect on the image quality. Also, the pump light after the OPO will have higher RIN than the picked-off pump light before the OPO due to the intensity fluctuations in the four-wave mixing (FWM) process. As long as the 800 nm is detected, this should have a minimal impact on image quality.

7.2.3 Amplifier similariton lasers for multiplex stimulated Raman scattering microscopy

In multiplex CRS microscopy, the sample is probed with a picosecond pulse and a femtosecond pulse. The additional bandwidth coverage of the femtosecond pulse allows multiple Raman resonances to be excited simultaneously, allowing for multiple molecules to be studied. This technique provides exciting diagnostic possibilities [5, 6], and the chance of clinical deployment would be greatly enhanced by a robust and inexpensive fiber source.

In recent work, the Insight DeepSee from Newport's Spectra-Physics was used for multiplex SRS microscopy [5]. This source provides a tunable beam from 680-800 nm with 120 fs pulse durations, and a fixed beam at 1040 nm with 200 fs pulse durations, which are converted to 2.3 ps durations through a pulse shaper. The femtosecond pulse at the shorter wavelength is detected [7, 5]. As with any SRS technique, having a near shot-noise limited pulse train is still critically important.

One route to achieving the necessary pulse parameters from a fiber source is to utilize the amplifier similariton laser [1]. The quietest pulses from fiber sources come directly from the oscillator. Since the amplifier similariton lasers generate the necessary bandwidth for the femtosecond pulse directly, they stand the best chance of achieving the necessary RIN. In 10 μm fiber, the laser can generate 20 nJ of pulse energy [8], so a portion of the output can be used for the femtosecond pulse, and the other portion can be filtered and spectrally compressed to pump the OPO, similar to the technique described for dissipative solitons in Chapter 6. Preliminary experiments show that this is a viable approach with optimization of the laser.

7.2.4 Single-pulse fiber sources for coherent Raman scattering microscopy

The two-color sources for CRS microscopy remain more complex than the single-pulse sources needed for florescence imaging and multiphoton microscopy. One route to simplifying the CRS sources would be to use a single broad-band pulse that covers both wavelengths in the same spectrum, as recently shown using a titanium sapphire laser [9]. This method could be particularly advantageous for imaging in the fingerprint region where the desired frequency shifts are 500-2000 cm^{-1}. To achieve the smaller frequency differences using fiber FWM, the photonic crystal fiber would need to be pumped quite close to the zero-dispersion wavelength. In this region, the parametric gain bandwidth is larger (see Fig. 5.1), and it is more difficult to achieve narrow-band picosecond pulses. These frequency shifts can be covered by spectra with bandwidths from 80 to 200 nm, which can be achieved directly from an Yb-doped fiber laser [10], or with modest spectral broadening after the output. Ideally, a high energy fiber laser would be used directly, eliminating added noise from amplification and/or frequency conversion.

7.2.5 Achieving noise reduction in optical parametric oscillators

Recent reports indicate that the signal from a $\chi^{(2)}$ OPO based on a solid-state crystal can have lower RIN than its pump laser [11]. This enables a noisier amplified fiber laser to be used to pump a solid-state OPO and still achieve a source that is suitable for SRS imaging with direct detection. In fact, in an 80 MHz system, the RIN level at 20 MHz on the OPO output is the same whether it is pumped by a fiber laser or a quieter solid-state laser. This effect can be caused by using low output coupling so the pulse resonates many times in the cavity before exiting or by saturation effects reducing pump fluctuations [11].

It is currently unclear whether the noise reduction seen in the $\chi^{(2)}$ OPO can be replicated in the $\chi^{(3)}$ OPO. There is reason to suspect it will be harder to achieve in the fiber OPO due to additional terms, such as stimulated Raman scattering, that may act to increase fluctuations. Also, the achievable pulse energies in the picosecond fiber OPO are limited to a few nanojoules before the output spectrum becomes too broad, which may limit the output energy from the device if the signal light is also resonate in the cavity. However, the noise reduction is interesting enough in its own right to merit future investigation.

7.3 Four-wave mixing inside the laser cavity

Fiber four wave-mixing is the critical process used to create the two-color fiber sources for Raman microscopy discussed in this thesis. In prior work, FWM was used to construct an optical parametric amplifier (OPA) [12], and in Chapter 5 (reference [3]), this work was extended to demonstrate a source based on an OPO. We now consider performing fiber FWM inside of a laser cavity, which would enable a two-color source from the same device, albeit with potentially different pulse parameter than those presented in prior work [12, 3]. Preliminary simulations indicate that moderate-energy pulses with few-hundred femtosecond durations may be expected.

7.3.1 Single-pass simulations

In order to assess the concept of intra-laser cavity FWM, we first perform single-pass simulations of FWM in photonic crystal fiber (PCF) pumped with the pulses we expect to exist inside of the laser cavity. Namely, we consider Gaussian pulses with 20 nm bandwidths chirped to a duration of 1 ps. These are launched into

5 cm of PCF with the same parameters as the fiber used in Chapter 5 [3], which is similar to the commercially available LMA-5 fiber (NKT Photonics). Similar to the OPA presented by Lefrancois and coworkers [12], the PCF is seeded with 5 mW of continuous-wave (CW) radiation at the idler wavelength. The energy in the pulses generated through FWM is maximized with pump pulse energies around 38 nJ; with longer PCF lengths or higher pump pulse energies, the output from the PCF tends towards supercontinuum. These results are presented in Fig. 7.3 and show that clean pulses near 800 nm can be generated under these conditions.

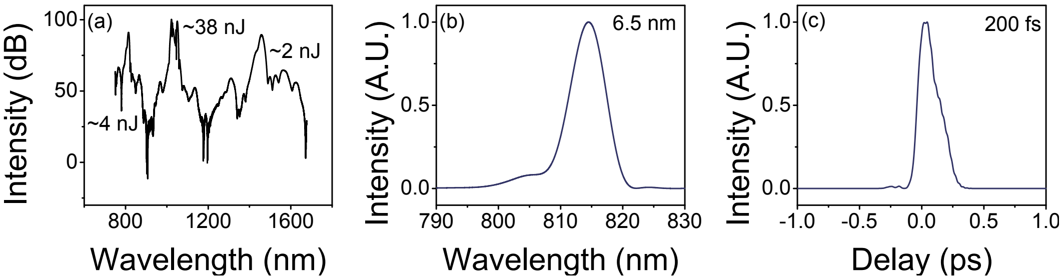

Figure 7.3: Four-wave mixing in 5 cm of photonic crystal fiber with the pump pulse described in the text: (a) full spectrum; (b) signal spectrum; (c) signal pulse.

7.3.2 Four-wave mixing in an amplifier similariton laser

The results shown in in the previous section indicate pump pulses near 40 nJ are desired for the FWM in this parameter regime. This suggests that a double-clad laser based on 10 μm core fiber is the best candidate to realize these results inside the laser cavity. Since output pulse energies of 20 nJ from an amplifier similariton laser [8] and 30 nJ from a dissipative soliton laser [13] are achievable with this fiber, the intracavitary pulse energy should be able to reach the necessary level. We expect amplifier similariton lasers to be more tolerant of perturbations in the cavity due to the presence of the local attractor, so we begin by simulating FWM in this laser. The schematic is shown in Fig. 7.4.

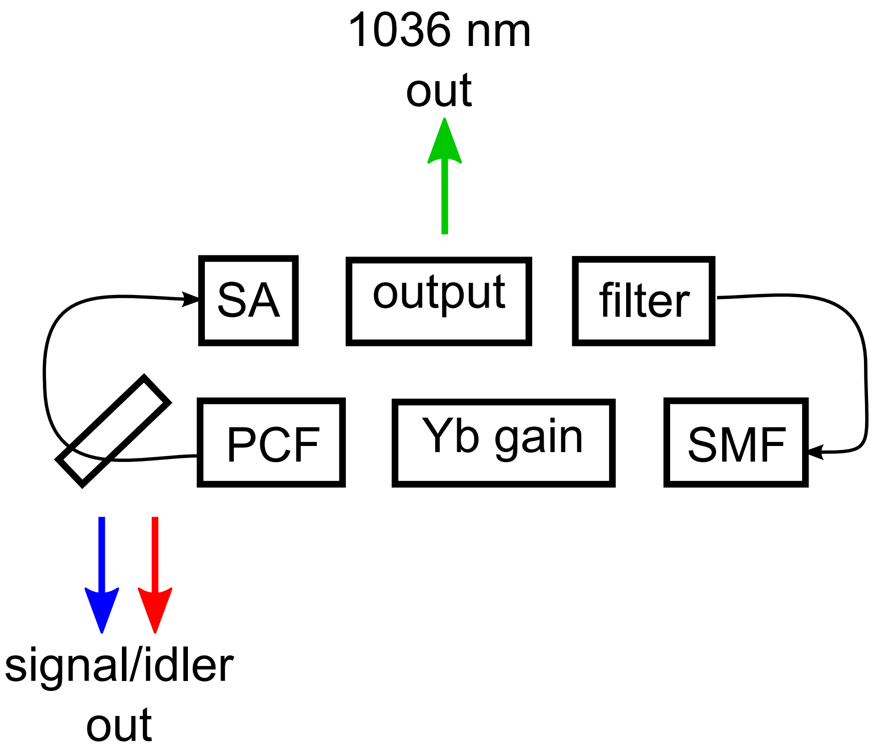

Figure 7.4: Schematic of laser used to simulate intra-cavity four-wave mixing. SA: saturable absorber; SMF: single-mode fiber; PCF: photonic crystal fiber.

The laser cavity consists of 2 m of passive fiber followed by 2 m of Yb-doped gain fiber, both with the 10 μm core diameter. The gain fiber is modeled with a fixed 30 dB gain, and optimal FWM results are found with a saturation energy of 16.8 nJ. The PCF after the gain is 6 cm, and 5 mW of CW seed light at the idler wavelength is added at the beginning of the PCF. The generated signal and idler pules are taken out of the cavity at the output of the PCF. The saturable absorber is modeled as an ideal curve with a 100% modulation depth. The output coupling is assumed to be 70%, and 30% additional loss is added to account for other experimental losses. A 2 nm spectral filter is used before the gain segment.

The simulation results are shown in Fig. 7.5. Simulations indicate that around 0.9 nJ of pulse energy can be generated at the new colors with pulse durations around 240 fs, as shown in Fig. 7.5(b-e) In this simulation, pulses with around

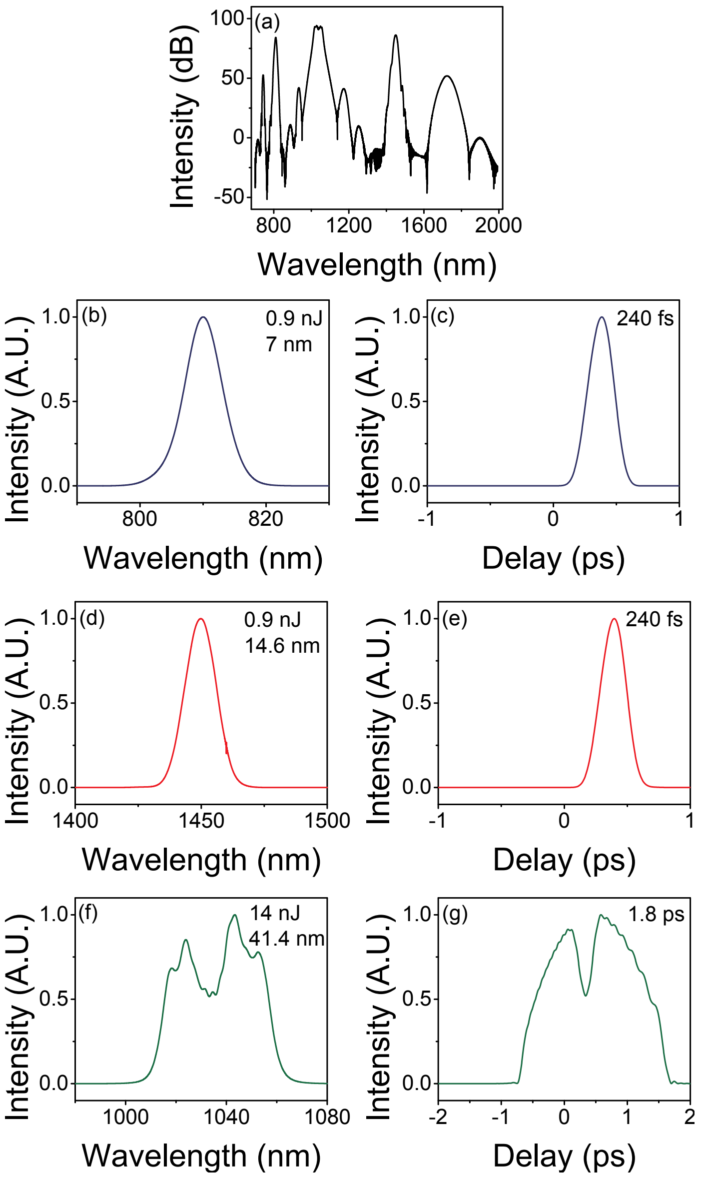

Figure 7.5: Simulated results of four-wave mixing inside of a double-clad amplifier similariton laser: (a) spectrum at the end of the photonic crystal fiber (PCF); (b) signal spectrum and (c) signal pulse at the end of the PCF; (d) idler spectrum and (e) idler pulse at the end of the PCF; (f) output spectrum from laser; (g) output pulse from laser.

27 nJ of energy at 1036 nm enter the PCF. At higher pulse energies, the simulation fails to converge. Further work is needed to assess whether this limitation is real or an artifact of the simulated spectral window. Fig. 7.5(f-g) shows the output from the laser at 1036 nm. Both the spectrum and the pulse show a dip in the

middle, which is the direct result of the FWM process. De-chirping this pulse should be similar to de-chirping the residual pump pulse from the OPO cavity, as shown experimentally in Fig. 7.2.

7.3.3 Four-wave mixing in a dissipative soliton laser

As indicated above, we may expect the amplifier similariton laser to be better-suited to intra-cavity FWM applications due to its larger tolerance for perturbations within the cavity. To test this hypothesis, the bandwidth of the intracavitary spectral filter is increased to 15 nm, which is in the range that generally supports dissipative solitons. Dissipative solitons can also tolerate a lower modulation depth saturable absorber, so this parameter is reduced to 80%. With lower modulation depths, the simulation fails to converge. All other simulation parameters are left the same.

The results for this simulation are shown in Fig. 7.6 and indicate that intracavity FWM inside of a dissipative soliton laser may allow for better performance than in the amplifier similariton laser. With a 61 nJ pump pulse entering the PCF, the pulse energy generated at the new wavelengths has doubled to 1.8 nJ. The pulses are longer, which is likely indicative of the larger chirp on the dissipative soliton pulses that are pumping the FWM process.

7.3.4 Conclusion

The initial simulations indicate that intra-cavity FWM may be viable route to creating a laser capable of having useful two- or three- wavelength output. At

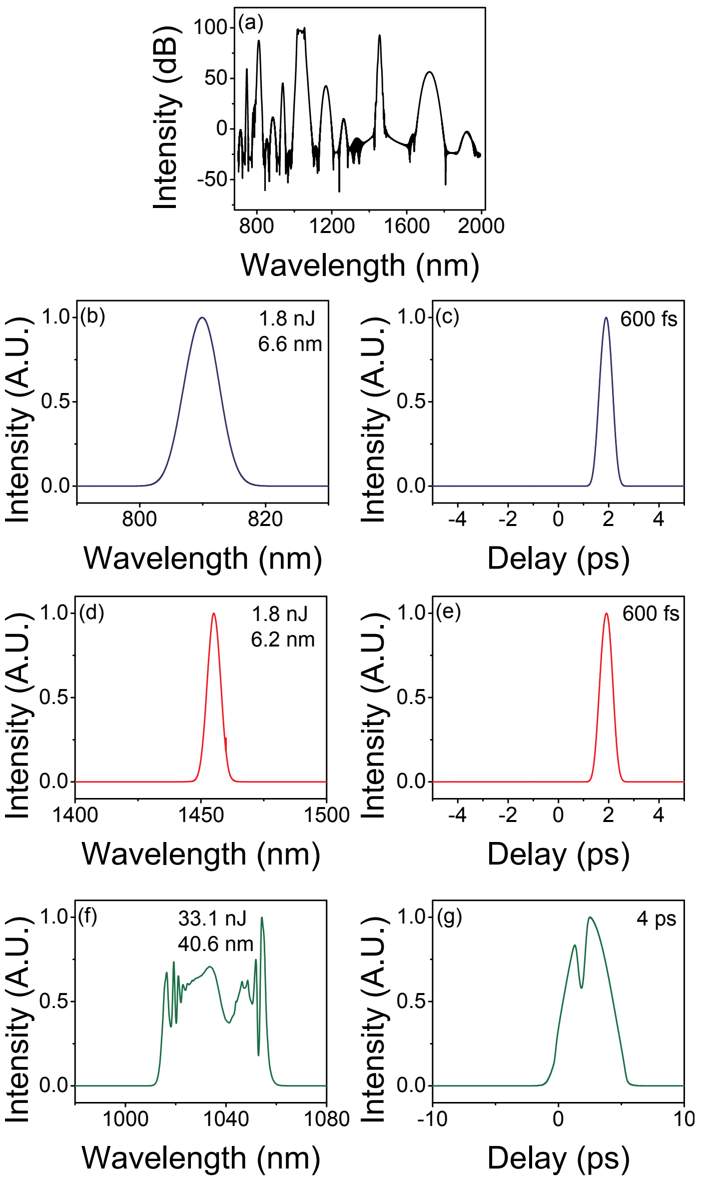

Figure 7.6: Simulated results of four-wave mixing inside of a double-clad dissipative soliton laser: (a) spectrum at the end of the photonic crystal fiber (PCF); (b) signal spectrum and (c) signal pulse at the end of the PCF; (d) idler spectrum and (e) idler pulse at the end of the PCF; (f) output spectrum from laser; (g) output pulse from laser.

least in simulation, the dissipative soliton laser supports higher pulse energy than the amplifier similariton laser.

It does appear that the pulse energies achievable at the new colors may be more limited than when a separate OPA or OPO stage is used. However, this approach to FWM may offer unique advantages in terms of the noise. The FWM is pumped by the intra-cavity pulse rather than the output. The intracavity pulse may have lower noise than the laser output, and allows for a higher energy pump pulse without the use of an amplifier. However, it will likely be difficult to achieve transform limited picosecond pulses using this approach, limiting its usefulness to picosecond SRS microscopy. Instead, a device based on this design may be useful for multiplex SRS microscopy using femtosecond pulses [14].

These preliminary simulations use a CW seed for the FWM process. In future work, it would be interesting to create a feed-back loop for one of the FWM products and use that to synchronously seed the FWM process. This would be similar to creating an OPO within a portion of the laser cavity. This may provide the route to the lowest-noise source.

BIBLIOGRAPHY

[1] W. H. Renninger, A. Chong, and F. W. Wise, Phys. Rev. A **82**, 021805 (2010).

[2] A. Klenke, M. Kienel, T. Eidam, S. Hädrich, J. Limpert, and A. Tünnermann, Opt. Lett. **38**, 4593 (2013).

[3] E. S. Lamb, S. Lefrancois, M. Ji, W. J. Wadsworth, X. S. Xie, and F. W. Wise, Opt. Lett. **38**, 4154 (2013).

[4] E. S. Lamb, L. G. Wright, and F. W. Wise, Opt. Lett. **39**, 2775 (2014).

[5] C.-S. Liao, M. N. Slipchenko, P. Wang, J. Li, S.-Y. Lee, R. A. Oglesbee, and J.-X. Cheng, Light Sci Appl **4**, e265 (2015).

[6] D. Fu, Y. Yu, A. Folick, E. Currie, R. V. Farese, T.-H. Tsai, X. S. Xie, and M. C. Wang, Journal of the American Chemical Society **136**, 8820 (2014).

[7] M. N. Slipchenko, R. A. Oglesbee, D. Zhang, W. Wu, and J.-X. Cheng, Journal of biophotonics **5**, 801 (2012).

[8] B. Nie, D. Pestov, F. W. Wise, and M. Dantus, Opt. Express **19**, 12074 (2011).

[9] S. Kumar, T. Kamali, J. M. Levitte, O. Katz, B. Hermann, R. Werkmeister, B. Považay, W. Drexler, A. Unterhuber, and Y. Silberberg, Opt. Express **23**, 13082 (2015).

[10] A. Chong, H. Liu, B. Nie, B. G. Bale, S. Wabnitz, W. H. Renninger, M. Dantus, and F. W. Wise, Opt. Express **20**, 14213 (2012).

[11] I. Rimke, G. Hehl, M. Beutler, P. Volz, E. Büttner, and A. Volkmer, Proc. SPIE 9329-69 (2015).

[12] S. Lefrancois, D. Fu, G. R. Holtom, L. Kong, W. J. Wadsworth, P. Schneider, R. Herda, A. Zach, X. S. Xie, and F. W. Wise, Opt. Lett. **37**, 1652 (2012).

[13] K. Kieu, W. H. Renninger, A. Chong, and F. W. Wise, Opt. Lett. **34**, 593 (2009).

[14] D. Fu, G. Holtom, C. Freudiger, X. Zhang, and X. S. Xie, The Journal of Physical Chemistry B **117**, 4634 (2013).

APPENDIX A

APPENDIX A: BUILDING FIBER LASERS

A.1 Introduction

During the experiments performed for this thesis, it became apparent that the performance of the fiber lasers can have a strong dependence on the components used to build them, even when specifications are nominally the same. In particular, achieving optimal performance of core-pumped amplifier similariton lasers and double-clad dissipative soliton lasers has been challenging. This appendix gives some general guidelines for selecting components and summarizes the cavity construction used to build very-well functioning lasers of both of these types.

A.2 General specifications

In addition to the specific advice offered below, a few general specifications should be kept in mind.

First, all components used in the laser should have low return loss. Ideally, nothing with a return loss worse than -65 dB should be used. In practice, components with a return loss of -60 dB are usually acceptable, and components with return loss of -55 dB are distinctly more challenging to work with. Lasers made with them may be harder to mode-lock, and self-lasing will also become problematic.

Second, care must be taken when splicing the fibers in the cavity. Especially for double-clad fibers, the Fujikura splicers tend to yield better results than the

Erikson splicers. A bad splice can result in difficultly in mode-locking or self-lasing. When using double-clad fiber, a bad splice can also increase multi-mode content, which will be seen in fringes on the spectrum. For specialty fibers, the splicers do not accurately estimate loss, so it becomes important to monitor splice loss independently to optimize the splice parameters.

Third, the wavelength-division multiplexer (WDM) has been found to be the culprit in numerous laser cavities with poor performance. The WDM appearing bright on an infra-red viewer can be a sign that the WDM has been damaged. Or, the WDM should also be suspected if the amplified spontaneous emission (ASE) spectrum shows unusual structure.

Fourth, for low repetition rate oscillators, it is extremely important to not leave the long lengths of fiber on the factory spool. The ease of mode-locking and stability of these cavities is greatly enhanced by removing the fiber from the spool and loosely coiling it on the table.

A.3 Amplifier similariton lasers

This laser is constructed using single-clad, core-pumped fiber. It mode-locks easily in minutes using the maximum output from a 600 mW pump laser. Pulse energies can be over 3 nJ, and spectral bandwidths are 30-40 nm at full-width, half-maximum. Importantly, it is easy to find single-pulsing, self-starting modes that avoid the continuous-wave breakthrough that is often observed in sub-optimal amplifier similariton lasers.

The example amplifier similariton cavity operated at a repetition rate of

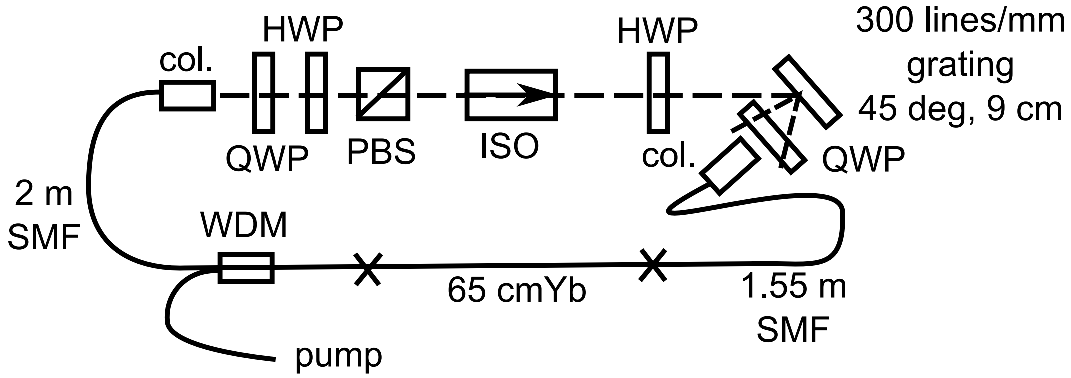

Figure A.1: Schematic of amplifier similariton laser cavity. HWP: half-wave plate; QWP: quarter-wave plate; PBS: polarizing beam splitter; ISO: isolator; col.: collimator; SMF: single mode fiber.

46.6 MHz and is shown in Fig. A.1. The laser is counter-pumped using a WDM from Lightel. There is 1.55 m of fiber before the gain, and the gain fiber is around 65 cm in length. The gain fiber is likely YB-501 from CorActive; all other fibers in the cavity are HI1060 (1060XP from ThorLabs). The free space section of the cavity is around 40 cm in length, so the remaining cavity length is passive fiber after the gain fiber. The filter is formed with a 300 lines/mm grating used at a 45° angle of incidence. The collimator is placed between 8.5 and 9 cm away from the grating. The collimators are out-of-production 1 mm aspheric lens collimators from OFR with a return loss of -65 dB; the closest replacement are the same from OZ Optics. The intracavity isolator is a low-power 1030 nm isolator from ThorLabs. The waveplates and polarizing beam splitter (PBS) are of unknown origin.

Example mode-locked spectra from this laser are shown in Fig. A.2. Many other core-pumped amplifier similariton lasers were constructed with similar designs during the work presented in this thesis with significantly worse performance in terms of pulse energy, spectral bandwidth, ease of mode-locking, and single-pulsing, self-starting operation. Based on the success of this cavity, it seems that

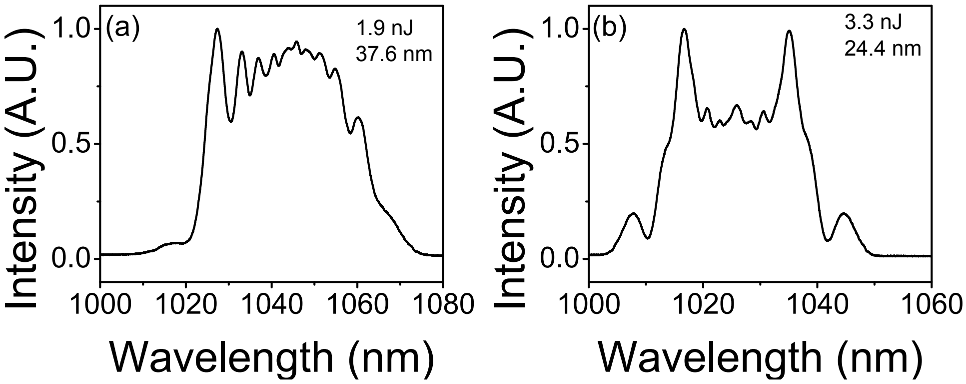

Figure A.2: Example spectra from Yb-doped fiber amplifier similariton laser.

slight differences in components may result in any of the above problems. In addition to finding proper components, the alignment of the grating filter is the other design parameter of which to be critical. When calculating the expected filter bandwidth, there is a wide tolerance in the angle of incidence and the separation between the grating and the collimator, but in practice, the laser can behave differently with only minor changes to these two parameters.

A.4 Double-clad dissipative soliton lasers

Despite the overwhelming success of the dissipative soliton laser, replicating top performance out of a cavity constructed with 10 μm fiber requires some care, in part due to the fact that the fiber is borderline multi-mode. For these lasers, using a proper splicer, such as a Fujikura splicer, is particularly important. The laser shown in Fig. A.3 is readily mode-locked in minutes using birefringent plate filters in the range 6T-15T (bandwidth of approximately 25 nm to 8 nm). Pulse energies of 20 nJ are easily achieved; higher pulse energies can be found with more care.

This laser operates at a repetition rate of 49.2 MHz. It is pumped using a diode

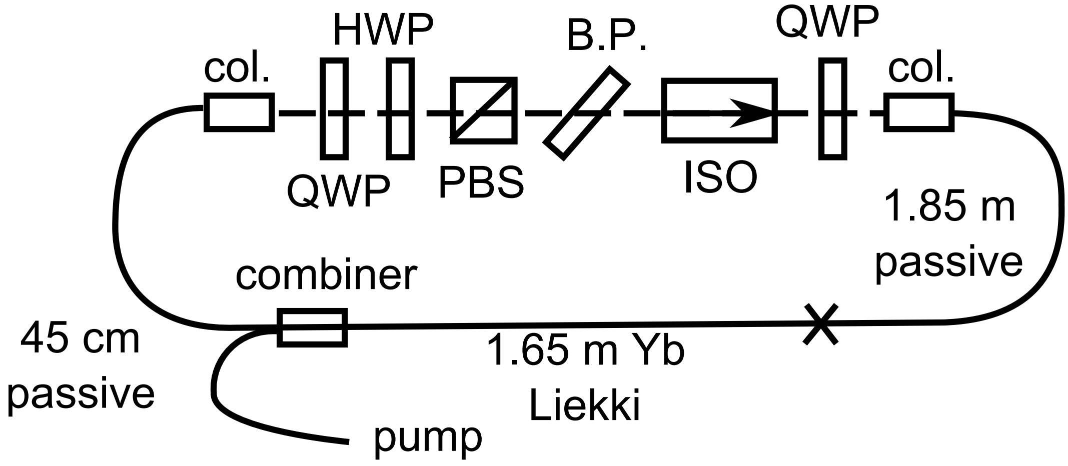

Figure A.3: Double-clad dissipative soliton cavity design. Yb: Ytterbium-doped fiber; col.: collimator, QWP: quarter-wave plate; HWP: half-wave plate; PBS: polarizing beam splitter; ISO: isolator.

from BWT Beijing with an output fiber with a 105 μm core using a combiner from ITF Labs. The gain fiber is the 10 μm core, double-clad gain fiber from Liekki and is 1.65 m in length. The laser is co-pumped; there is a 45 cm piece of passive fiber after the gain, the free space section is around 40 cm, and the remaining cavity length is passive fiber preceding the gain fiber. All fiber within the cavity has the 10 μm core size. The filter is a quartz plate from either VLOC or nLIGHT Photonics. The 1.1 mm aspheric lens collimators are custom collimators from OZ optics specified for few-watt level applications. The intra-cavity isolator is a high-power isolator from ThorLabs. The waveplates and PBS are of unknown origin.

The repetition rate of this laser is reduced by adding HI1060 (Corning) before the gain fiber so as not to introduce multi-mode content by increasing the amount of 10 μm core fiber in the cavity. To reduce splice losses, the HI1060 is spliced to SMF28e+ (Corning) on both ends, and then the SMF28e+ is spliced to the 10 μm core fiber. This laser mode-locks quite easily with narrower filters down to around 20 MHz. Below 20 MHz, mode-locking becomes more difficult but is still achievable with care.

The laser cavity functions comparably to the initial demonstration by Kieu *et al.* [1] and better than other cavities attempted in the course of this thesis work. A few differences between this cavity and the others are worth noting. First, very minimal fringes are observed on the output spectra, indicating little to no multimode content in the laser output. This could be due in part to the amount of fiber in the cavity or to the specific fiber manufacturers. In particular, the Liekki fiber is found to work better in the laser than the comparable fiber from CorActive. However, this could depend on the specific batch of the fiber and may not always be true. Finally, if using a pump diode without wavelength stabilization (as is the case for the pump diode used here), temperature tuning the diode to maximize laser efficiency (within the temperature range of the diode) can noticeably improve performance.

BIBLIOGRAPHY

[1] K. Kieu, W. H. Renninger, A. Chong, and F. W. Wise, Opt. Lett. **34**, 593 (2009).